THESIS

V/W-BAND SATELLITE COMMUNICATION SYSTEMS

Submitted by

Zachary Mendez

Department of Electrical and Computer Engineering

In partial fulfillment of the requirements

For the Degree of Master of Science

Colorado State University

Fort Collins, Colorado

Summer 2021

Master's Committee:

Advisor: Venkatachalam Chandrasekar

Margaret Cheney
Thomas Siller

ABSTRACT

V/W-BAND SATELLITE COMMUNICATION SYSTEMS

The increasing demand for high-speed wireless communications are driving new innovations and developments in telecommunications engineering. Telecommunication systems are taking advantage of the developments in manufacturing and integrated circuit design to provide improved communication system performance. Contemporary satellite communication systems typically operate in the frequency regions between S-band and Ku-band. Improved manufacturing techniques are allowing for systems to be reliably constructed to operate in the millimeter wave frequency bands, which inherently increases data rates by increasing the available bandwidth, and improving wireless communication system efficiency. High throughput satellites are being developed to utilize these higher frequencies, and employ multiple access techniques to provide more capabilities for users. The future of satellite communications will utilize V/W-band communication systems to increase the available bandwidth and realize more effective communication and radar systems.

This thesis presents the system design and development of a V/W-band multiple-input multiple-output (MIMO) antenna system. The multibeam feed assembly development is presented from the initial stages of design and simulation, to the building and testing of waveguide prototypes, and through integration into a full-scale antenna system that is built and tested at a near-field antenna range for a system demonstration. The system demonstration includes frequency mixing modules to serve as the communication interface, the multibeam feed horn assembly, and an offset fed parabolic reflector. The system measurements are compared to simulated results obtained with CST Microwave Suite® for system validation.

ACKNOWLEDGEMENTS

I would like to thank my advisor, Dr. V. Chandrasekar, for his guidance and providing me with numerous opportunities to learn and gain practical experience in the field. The challenges I was able to face and overcome throughout the course of this program were invaluable, and I am very grateful the experience. Thank you Dr. Cheney and Dr. Siller for taking the time to read my thesis and for the opportunity to defend it.

I would like to thank Dr. Keith Kelly for sharing his expertise in RF design and his availability to provide support to overcome obstacles and challenges. Allowing me to carry out the development of this novel system was an incredible opportunity to exercise my skills and gain crucial experience in my career. Thank you to all of my colleagues at Agile RF Systems, each of which have been crucial to my learning and professional development as an engineer. Thank you to our partners for providing the expertise to fully realize and test this complex antenna system, the project could not have concluded without their inputs and support.

This work was supported by the Air Force Research Laboratory under contract FA8750-17-C-0237.

Finally, thank you to all of my friends and family for their unwavering support in my endeavors. Thank you to my parents for their love, and for constantly encouraging me to pursue my goals. Thank you to all of my friends who encourage me to challenge myself, and for their compassion.

TABLE OF CONTENTS

LIST OF TABLES

LIST OF FIGURES

Chapter 1

Introduction

1.1 Motivation

Millimeter wave systems are on the frontier of wireless communications. The demand for high data rates from an increasing number of wireless users continues to drive the development of new systems that offer larger bandwidth channels. Higher bandwidth systems can support more simultaneous users, and effectively increase communication speed. Next generation communication systems that use frequencies in the millimeter wave region (30-300 GHz) will greatly increase the available bandwidth per channel, compared to microwave communication links. Innovations in wireless system design and manufacturing make these systems more realistic to realize and employ. Designing these systems to support multiple-input multiple-output methods further increases the number of users that can be supported by a single system, making it more cost effective as a single unit.

The next generation communication systems are taking advantage of new manufacturing technologies to economically realize complex system components. Radio frequency (RF) hardware is constrained by the carrier frequencies utilized, more specifically, the inversely related wavelength of the operating frequency. As the frequencies increase, the physical dimensions of the RF communication subsystems must decrease. As components become smaller and smaller, they become more difficult and expensive to manufacture. One challenge of developing new millimeter wave systems is reliably, and economically, manufacturing the communication hardware. The benefits of increased communication capability justify the research and development effort expended towards millimeter wave telecommunication systems. V-band (50-75 GHz) and W-band (75-110 GHz) regions are being employed in a variety of wireless system applications. Automotive radars, terrestrial communication systems, satellite communication systems, and weather radars are all

utilizing state-of-the-art millimeter wave integrated circuits and wireless transmission systems to provide new and improved capabilities in their respective domains.

This thesis focuses on the development of an innovative satellite system to operate in V/W-band that utilizes an architecture to support MIMO and full duplex communication capabilities. MIMO is achieved with a multibeam feed assembly configured for an offset fed parabolic reflector, and is capable of dual-circular polarization for uplink and downlink. The system development iterates through simulations using CST Studio Suite® (CST MWS) to design a waveguide network from its building blocks to full system complexity. These steps are corroborated by the building and testing engineering coupons representing the features necessary to realize the network. Design and simulation was also carried out for the full antenna system, including the feed aperture and parabolic reflector. The system development concludes with a full-scale V/W-band prototype antenna system that was measured at a near field antenna range to compare measured performance to simulated performance.

1.2 Objective

The V/W-band telecommunication system is a full scale prototype satellite communication antenna. It operates at 71-76 GHz and 81-86 GHz for transmit and receive bands, respectively, to offer 5 GHz bandwidth for uplink and downlink. The objective of this thesis is to describe the design and development of a V/W-band multibeam feed array to be utilized for this communication system. The feed array is realized using a waveguide feed network consisting of 19 independent waveguide channels. The waveguide network is integrated with an offset fed parabolic reflector system to measure its effectiveness with the full RF transmission system. The antenna system provides 19 beams, each of which have a beamwidth of 0.3 degrees and are all packed into a 2-degree beam space.

Typical multibeam wireless communication feeds employ complicated beam forming networks to maximize the directivity of the antenna. In such a configuration, a cluster of feed horns can be combined through the network to form a single beam. The antenna system system utilizes

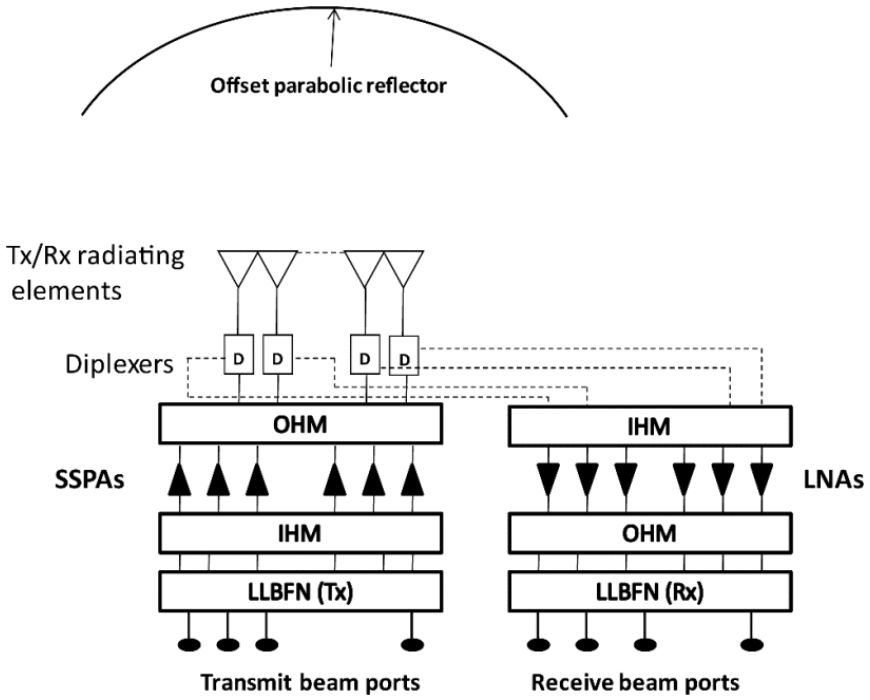

Figure 1.1: Architecture for beam combining network, typically utilized in multibeam wireless communication systems.

source: [1]

completely independent feed horns for each of its 19 beam in both communication bands. This development provides benefits including a very compact feed horn assembly that reduces blockage of the reflector.

The V/W Satcom system operates as a full-duplex system with 19 transmit and receive beams covering the same space simultaneously, and each beam has access to the full 5 GHz communication bandwidth range, greatly increasing its maximum throughput. Typical multibeam systems require bulky feed horns to realize all beams, but a major benefit for this system is that the multibeam feed horn is small due to the millimeter wave frequency band, and therefore is easily implemented in an offset fed reflector architecture. Additionally, the feed horn realizes all 19 beams independently, not requiring complicated networks, such as depicted in Figure 1.1, where multiple beam states are combined through a complicated network for each communication beam.

1.3 Thesis Organization

This thesis is organized to present the engineering development of a multibeam V/W-band RF system designed for a satellite based communication system, including the theoretical basis for design, computer-aided design and simulation, building and testing coupons, then building and testing a full scale system prototype. The thesis is organized as follows:

Chapter 2: An introduction to satellite communication systems.

Chapter 3: A literature review focused on development of RF systems through simulation, and prototype evaluation.

Chapter4: The design of the V/W-band wireless communication system components through the process of simulation and an iterative build and test process.

Chapter 5: Presents the measured results of the V/W-band waveguide feed assemblies as well as the integrated antenna systems.

Chapter 6: The conclusions gathered from the system development and evaluation, along with future work.

Chapter 2

Satellite Communication Systems

2.1 Introduction

Communication satellites serve as gateways to connect users across the globe. Shown as an example in Figure 2.1, users on the ground can relay signals by utilizing a satellite as a signal repeater towards a receiver. The primary attribute of any communication system is its capacity for information throughput, which can determine the amount of users that a system can support and the speed of information flow between users. This makes techniques and innovations to increase available bandwidth in wireless systems an important and active area of research and development Frequency reuse, implementing MIMO systems, and increasing carrier frequency and bandwidth are all active areas of research aimed at maximizing the service capabilities of individual telecommunication systems.

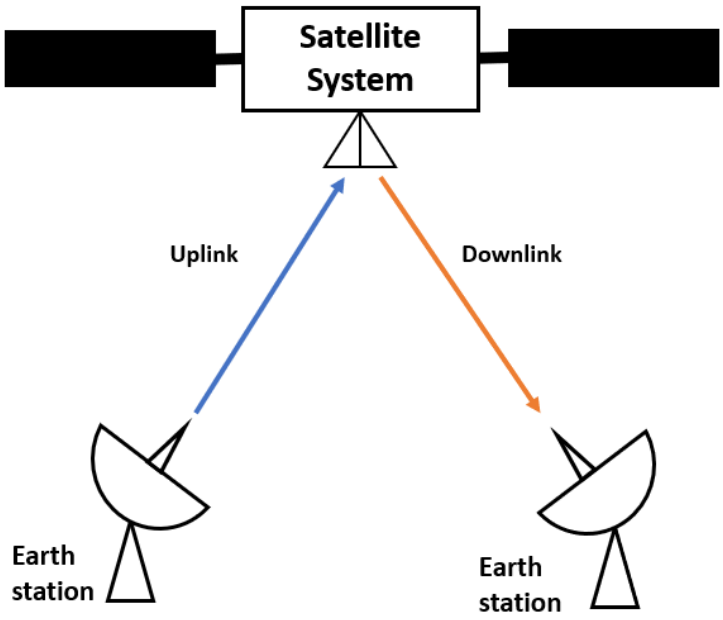

Figure 2.1: A communication satellite receives communication signals from an Earth station, then amplifies and converts the signal before repeating it back to another Earth station.

The high level system design decisions in a space-based system design are the power system, antenna size and architecture, maximum allowable mass [2]. Communication satellites are designed to balance these key parameters with their capacity to serve as a high capacity communication gateway or broadcast system.

2.1.1 Frequency Reuse

It is essential for satellite communication systems to reach as many users as possible while constraining hardware mass and size. There are several design aspects to consider when developing a novel telecommunication system so that it is maximally effective. Modern satellite links are able to dynamically deal with many users simultaneously, without interrupting service. Multiple-input multiple-output systems have become standard in many wireless communication applications due to the technology becoming more available. MIMO systems can use a single unit to provide service across a wide spatial region with multibeam antennas, such as shown in Figure 2.2.

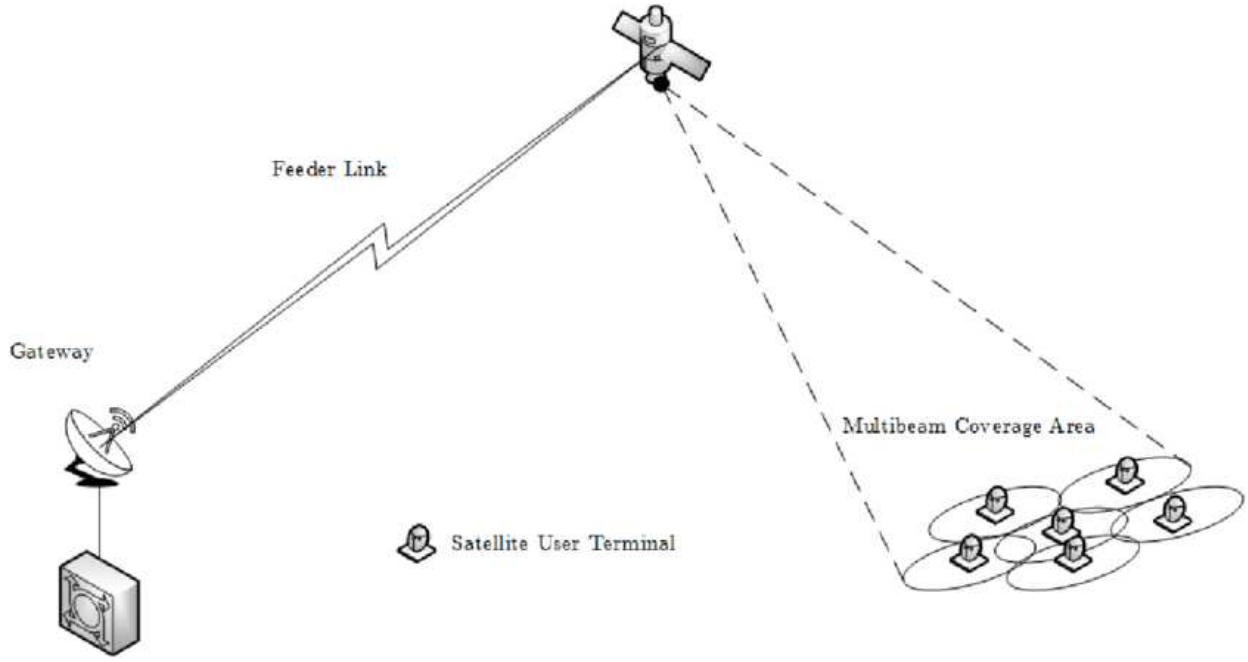

Figure 2.2: Multi-beam Wireless System Architecture [3].

Frequency reuse relies on the spacial separation of users to allow for a single system to serve many users with a high quality communication link. A communication system has the ability to serve several cells in a large area, with each cell being assigned a frequency band within the transmission systems capability, and adjacent cells operate in a frequency band with a sufficiently separated spectrum to not cause interference. Such a frequency reuse technique is depicted in Figure 2.3.

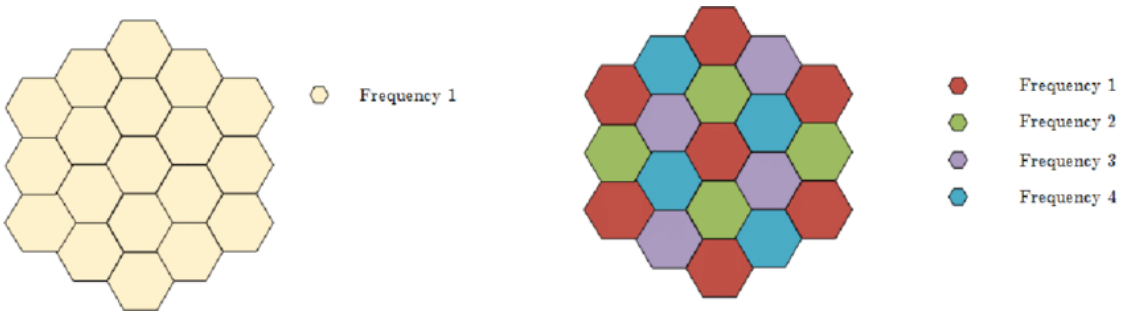

Figure 2.3: Single color (left) and multicolor (right) frequency reuse [3].

If a system has a sufficient amount of cells, the a frequency band can be reused a number of cells over, defined by equation 2.1 where r_u is the distance and C is the size of a cell cluster. The amount of cells required frequency reuse is also determined by the multiple access technique that is chosen from before.

$$r_u = \sqrt{3C} \tag{2.1}$$

The basis of a telecommunication system is to transmit and receive random signals to over large distances. A metric to characterize these systems is the quantity of information that can be relayed per unit time, which has been exponentially increasing since the beginnings of telecommunications. The current state of the art telecommunication systems can exceed 10^{10} bits per second over wired connections, and wireless systems are beginning to reach the stage of gigabit connectivity ($> 10^8$ bits per second). High throughput wireless communication systems are on the forefront of higher data transmission rates due to their inherently large bandwidth, achieved by utilizing higher and higher frequency bands. The amount of data that can be transmitted is directly related to the RF bandwidth of a communication channel, and is defined by the following two equations.

$$C = 2B \log_2(M) \tag{2.2}$$

$$C = B \log_2 \left(1 + \frac{S}{N}\right) \tag{2.3}$$

Where B is bandwidth, and $\frac{S}{N}$ is in linear scale, and the channel capacity, C, is measured in bits per second (bps). The difference in these two equations is that the Shannon equation (2.3) accounts for the signal to noise ratio to describe the possible communication symbols, where M denotes the quantity of symbols available, unlike the Nyquist equation (2.2). Maximizing the available bandwidth of a communication system maximizes its carrying capacity, making bandwidth a key area of interest in system design.

2.1.2 Atmospheric Absorption

Water in the atmosphere is the primary contributor to losses seen by electromagnetic waves propagating through the atmosphere. Cloud coverage can typically be ignored when communicating with systems operating at frequency bands below Ka-band (26.5-40 GHz), and at these higher bands cloud coverage can have a much larger impact and must be accounted for [4].

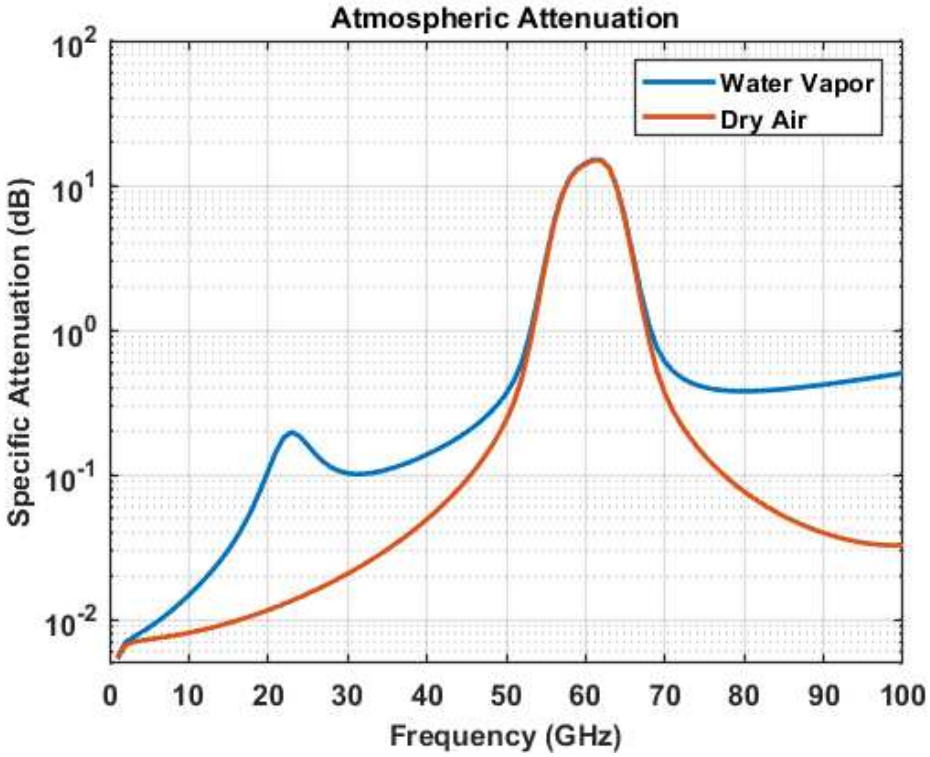

Figure 2.4: Attenuation from the atmosphere vs frequency [5]. The band of interest for this system is 71 - 86 GHz where attenuation begins to decline.

The attenuation from the water and oxygen content in the atmosphere at W-band is comparable to the attenuation at Ka-band, which is another major factor contributing to interest in advancing V/W-band satellite communication technology [6]. Still this is a large consideration to add to path loss while processing the link budget for a new communication system design.

2.2 Next Generation Satellite Systems

Millimeter wave bands are an active area of research with many areas of application, including uses in astronomy, millimeter-wave imaging including medical applications and remote sensing, providing gigabit capable communication links, and high sensitivity radar systems [7]. The nature of signals at these frequencies allow for very high resolution imaging, and large bandwidth communication signals for high data transfer rates which can outperform systems designed to operate in the lower end of the radio frequency spectrum.

There are a large variety of industries that are interested in taking advantage of the new capabilities provided by Q/V/W-band wireless systems. Satellite links at these frequencies can be utilized to host many more users simultaneously, while providing better performance than contemporary telecommunication systems.There are also applications for terrestrial use in cellular communications. 5G networks are currently in development across the world, with a promise of building the backbone of new infrastructure to support a new communication age. Implementing a 5G network that utilizes millimeter-wave frequencies allows for support for many more users in a single cell, potentially 1,000 more devices per square meter than 4G networks that are the current state-of-the-art [8]. The large-scale roll-out of these systems to users is still in the early stages, but the largest telecommunication companies are all racing to provide this infrastructure and lead the way in developing this new technology.

KA-SAT

The KA-SAT, launched in December 2010, is a next generation communication satellite that exemplifies a system that maximizes communication carrying capacity. KA-SAT employs travelling-wave tube amplifiers in the transponders to provide high capacity communication links at Ka-band,

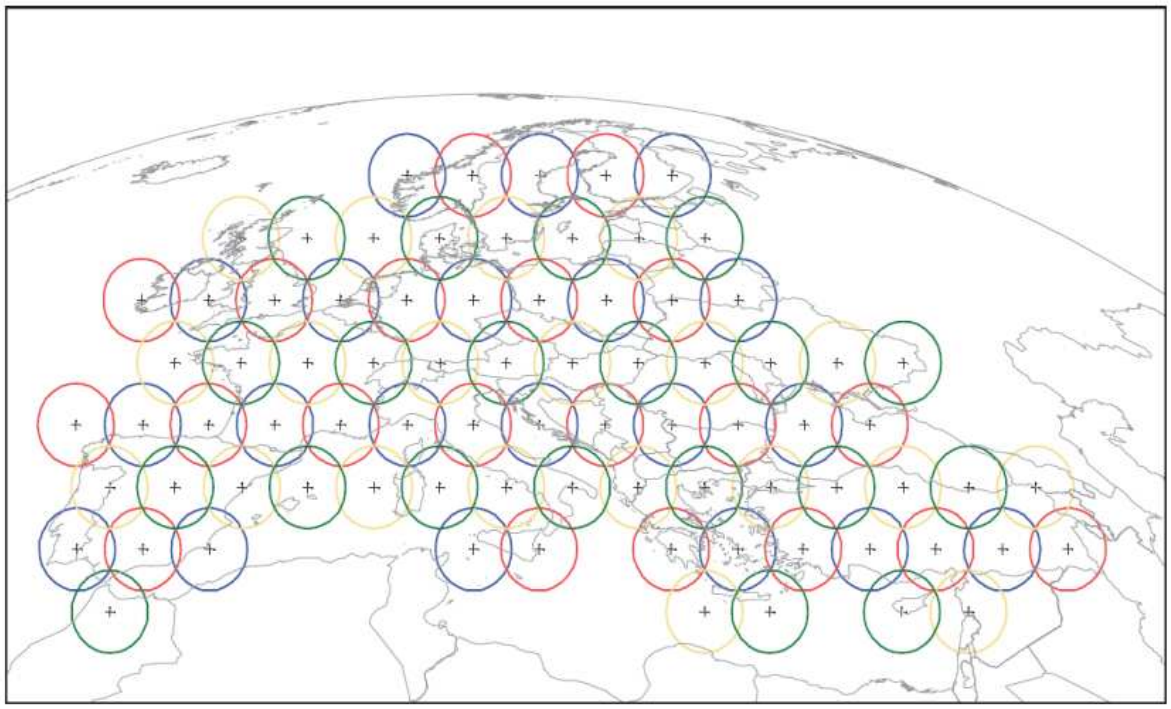

Figure 2.5: Example of a four-color frequency reuse scheme [9].

as well as Q/V-band for their Gateway links. The Ka-band transponders increase the data carrying capacity of the system by operating with a four-color reuse scheme over a large color area, seen illustrated in Figure 2.5.

KA-SAT offers 250 MHz of bandwidth for the uplink and downlink channels, and a 500 MHz spectrum for each polarization, right and left hand circularly polarized. Uplink it relegated to 27.5-30 GHz for Ka-band, and 47.2-50.2 GHz for the Q/V-band gateway, and the downlink operates at 17.3-20.2 GHz and 37.5-40.2 GHz for the respective links. Through these methods, the service capacity for this new generation is reported to be 90 Gbps, greatly outperforming the earlier generation of communication satellites [9].

WAVE Mission

The W-Band Analysis and VErification (WAVE) mission, being carried out by the University of Rome in conjunction with the Italian Space Agency, is continuing to explore the feasibility and

effectiveness of W-band satellite communication systems [10]. The goals of the mission are to gather experimental data on atmospheric effects of signal propagation at W-band, test data-relay capacity, and to validate W-band technologies and space-qualification. These are popular areas of research with millimeter wave electrical components becoming more feasible for production and economical for research groups. Industry is taking advantage of these capabilities as well, and exploring ways to implement this new technology for improved services.

There are technical challenges when operating at these very high frequencies, all of the electrical components are quite sensitive, and tolerances can have a larger negative impact on performance. There are great payoffs to succeeding with this communication technology, it is very efficient for overall satellites that are designed under strict size and mass requirements. Transmission is also more efficient due to larger bandwidths and less interference at this higher than standard frequency band. Data rates can exceed 100 Mbps, these new technologies that are being deployed to offer gigabit connectivity [11].

Chapter 3

Literature Review

3.1 Transmission Lines

3.1.1 RF Network Analysis

Waveguide is a common component in RF transmission systems due to their exceptionally low loss and high power handling capabilities [12]. Waveguide confines an electromagnetic wave in a region, and allows it to propagate with very low loss inside of the waveguide region. Waveguides are characterized with the same techniques as other high frequency transmission lines. High frequency, two-port (or multi-port), devices and networks are defined by their scattering matrix, or S-parameters, which are described the equivalent circuit parameters. The scattering matrix is derived from the transfer matrix (equation 3.1), and the impedance matrix (equation 3.2). High frequency networks are not easily described by familiar circuit parameters, voltage and current. It is more practical to describe them in terms of how travelling waves behave at device interfaces.

$$\begin{bmatrix} V_1 \\ I_1 \end{bmatrix} = \begin{bmatrix} A & B \\ C & D \end{bmatrix} \begin{bmatrix} V_2 \\ I_2 \end{bmatrix} \tag{3.1}$$

$$\begin{bmatrix} V_1 \\ V_2 \end{bmatrix} = \begin{bmatrix} Z_{11} & Z_{12} \\ Z_{21} & Z_{22} \end{bmatrix} \begin{bmatrix} I_1 \\ I_2 \end{bmatrix} \tag{3.2}$$

A common method to characterize a high freuqency device is to embed it into a network along with a vector network analyzer. A vector network analyzer describes the scattering matrix (3.3). The a and b matrices describe incoming and outgoing waves of a two-port devices, refer to Figure 3.1. The a and b matrix elements are related to the voltage, current, and impedance elements in the transfer and impedance matrices. Their relations are shown in (3.4a - 3.4d). When measuring a passive two-port waveguide, the primary characteristics are the S11 and S21 parameters, known

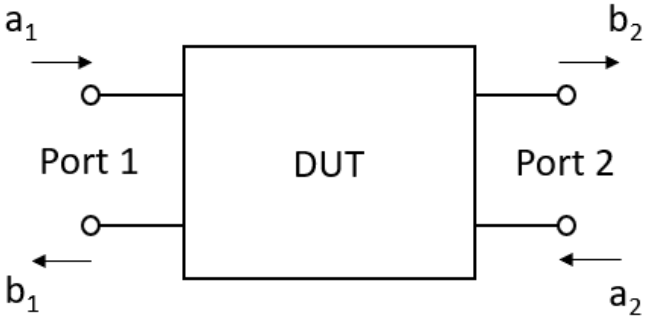

Figure 3.1: A two-port device-under-test (DUT) is shown here with the a and b parameters that represent incident waves and their reflection.

as the reflection and transmission coefficients [13]. An ideal waveguide transmission line has an S11 of 0, and an S21 of 1, indicating that all energy is transmitted through the guide, and none of it is lost to reflection. In a real waveguide system, there is some energy that is lost at the waveguide interface, known as reflection loss, and there are conductor losses in the walls of the waveguide, which can be referred to as insertion loss.

$$\begin{bmatrix} a_1 \\ a_2 \end{bmatrix} = \begin{bmatrix} S_{11} & S_{12} \\ S_{21} & S_{22} \end{bmatrix} \begin{bmatrix} b_1 \\ b_2 \end{bmatrix} \tag{3.3}$$

$$S_{11} = \frac{b_1}{a_1}\Big|_{a_2=0} \tag{3.4a}$$

$$S_{12} = \frac{b_1}{a_2}\Big|_{a_1=0} \tag{3.4b}$$

$$S_{21} = \frac{b_2}{a_1}\Big|_{a_2=0} \tag{3.4c}$$

$$S_{22} = \frac{b_2}{a_2}\Big|_{a_1=0} \tag{3.4d}$$

3.1.2 Waveguide Design

The operating frequency of a waveguide transmission line is determined by the physical dimensions of the waveguide channel. The dimensions required to propagate the dominant mode facilitated by the system requires the dimensions indicated by solving for the cutoff frequency using (3.5) generally, and (3.6) for the dominant mode in rectangular waveguide [12]. Rectangular waveguide is generally described by dimensions *a* and *b* as the side lengths, referring to Figure 3.2. The variables *m* and *n* are indices to relate the order of the TE or TM modes cutoff at a particular frequency, f_c. of If the dimensions are too large, an evanescent mode occurs in the indicated frequency range and quickly attenuates through the channel, effectively making waveguide a high-pass filter. A V/W-band RF system typically uses standard waveguide sizes including WR-10, WR-12, and WR-15. COTS waveguide components are still not widely available for these dimensions.

$$f_{c_{mn}} = \frac{k_c}{2\pi\sqrt{\mu\epsilon}} = \frac{1}{2\pi\sqrt{\mu\epsilon}}\sqrt{\left(\frac{m\pi}{a}\right)^2 + \left(\frac{n\pi}{b}\right)^2} \tag{3.5}$$

$$f_{c_{10}} = \frac{1}{2a\sqrt{\mu\epsilon}} \tag{3.6}$$

Cylindrical waveguide is applied through the same principles as rectangular waveguides, the primary difference being that they are more easily described using a cylindrical coordinate system. The parameters describing a cylindrical waveguide are shown in Figure 3.3, and the cutoff frequency equation (3.7). The cutoff wavenumber, k_c, is described by the extrema of the Bessel function of the same order as the desired transverse mode cutoff frequency. The radius, *a*, and waveguide material determine the cutoff frequency for each propagating mode. In this cylindrical case, the first waveguide mode not subject to cutoff is TE_{11}, making it the dominant mode.

$$f_{c_{nm}} = \frac{k_c}{2\pi\sqrt{\mu\epsilon}} = \frac{\rho'_{nm}}{2\pi a\sqrt{\mu\epsilon}} \tag{3.7}$$

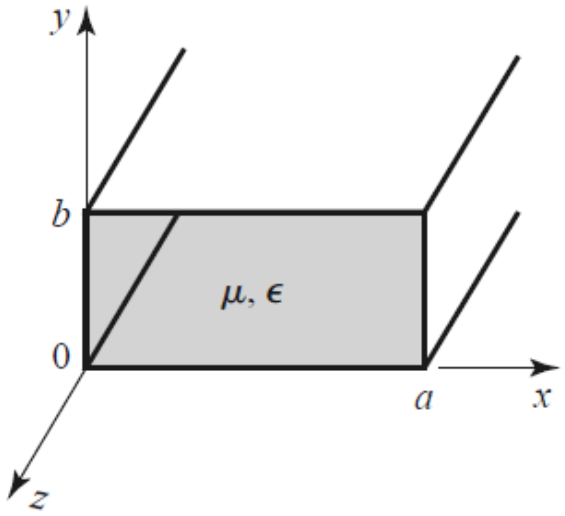

Figure 3.2: Geometry of a rectangular waveguide. Typical rectangular waveguide denotes the long dimension as a and the short dimension b, typically half of a. Transverse electric or magnetic waves propagate along the z-axis.

Source: [12]

.

The waveguide feed assembly requires several waveguide transitions, made up of different waveguide configurations. The theoretical basis for design of the square waveguide, and the rectangular waveguide that must be less than half of the square to be realizable, is based off of the rectangular waveguide equations. The cylindrical waveguide section is necessary to realize the circular polarization for the feed horns, and it is sized to ensure no higher order modes propagate and interfere with the signals.

The design basis for the V/W-band feed horn waveguide system begins by ensuring the cutoff frequency for each waveguide geometry used allows for full transmission of the communication band supported by the respective networks. Simulations were created to analyze the waveguides, and increase confidence in the design. CST MWS full-wave solvers simulate the S-parameters for the ideal waveguide sections, and it independently calculates and verifies the mode cutoff frequencies. Based on the results observed from simulation, waveguide coupons were built and tested to compare the experimental measurements to simulated results. Following through this design

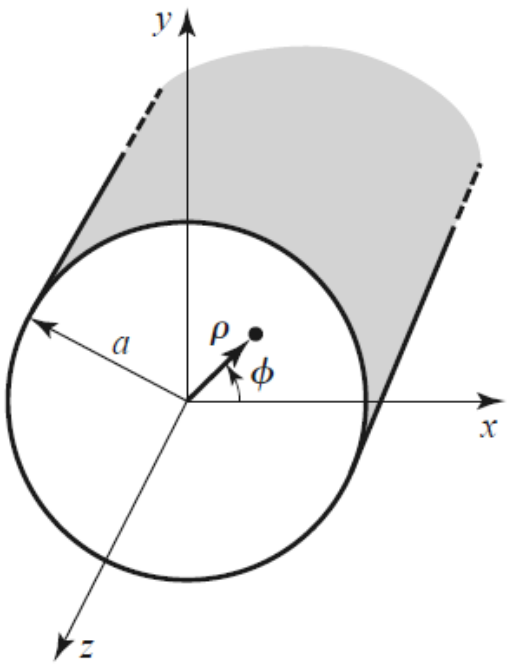

Figure 3.3: Geometry of a circular waveguide. The radius of the circular cross section is a, and the transverse electric or magnetic waves propagate along the z-axis just as in rectangular waveguide. The field equations are typically denoted in a cylindrical coordinate systems, being defined as functions of ρ, ϕ, and z.

Source: [12]

process, the risk in combining waveguide subcomponents into the waveguide feed assemblies is substantially reduced.

3.2 Full-wave Simulation

Subcomponents in RF systems can be modeled in full-wave simulation software to fully characterize subsystem features that have the potential to impact the transmission performance of the subsystem. In [14] CST MWS simulation software was used to design a section of square waveguide that included a mitered 90-degree bend. The methods implemented in this paper detail the process an RF engineer goes through to design waveguide features for their particular usage case. Utilizing full-wave solvers as the first step in the design process for custom waveguide features, such as mitered waveguide turns or other less common transitions, is very effective because there are many unknowns introduced by these transitions. Full-wave simulation gives insight into the phase impact and transition losses that these features introduce. These parameters are essential for system design, and can be explored quickly and inexpensively through simulation. The benefits of using a full-wave solver also include convenient visualization tools as well as a comprehensive documentation of all transmission parameters that impact the system performance. Tolerance analysis can also be simulated to predict the impact of machining tolerances, and then design more robust components that are less susceptible to performance degradation.

Square waveguide is useful in dual-polarized and circularly-polarized high power RF transmission applications, such as meteorological weather radar systems, millimeter wave systems, and wireless communication systems. The key feature is the ability to transmit both TE_{10} and TE_{01} modes effectively, shown at the waveguide port in Figure 3.4, providing an effective path to success for system applications that require dual-linear or circular polarization.

The phase impact of a mitered bend is best discovered and analyzed in a full-wave solver environment as seen in [14]. The primary merits of design are the complex S11 and S21 parameters, given that the bend they simulated is passive and reciprocal. The authors chose to compensate the phase impact in the bend with a ridge along the wall, which can be seen in the CAD model shown

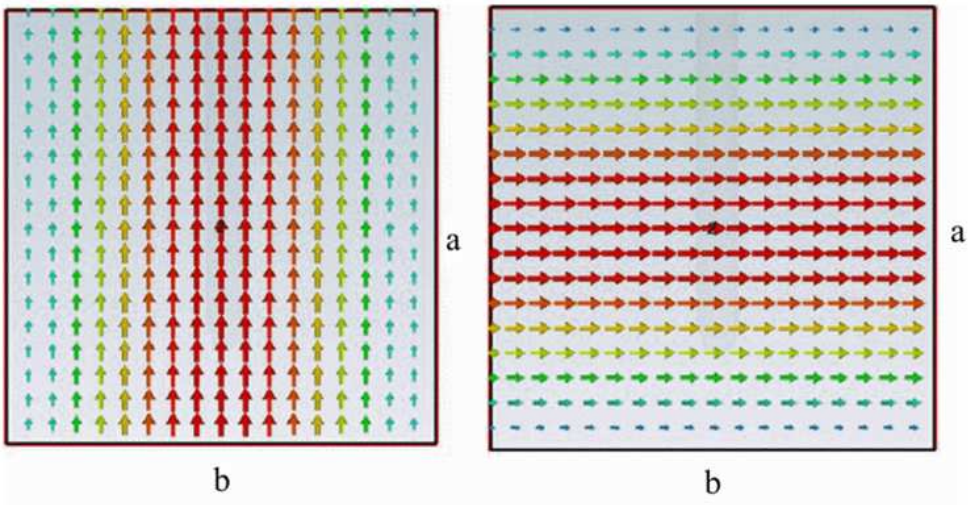

Figure 3.4: Simulated E-field at a square waveguide port in CST MWS for TE_{10} mode (left) and TE_{01} mode (right).

Source: [14]

in Figure 3.5. The authors conclude that additional waveguide transitions are necessary to maintain acceptable polarization discrepancy between modes. These features are more readily realizable at X-band, which this waveguide section was designed for.

It is essential to build prototypes to further evaluate simulations to gain confidence in a design before moving forward. Figure 3.6 shows the comparison between the simulated and measured experimental result of the square waveguide mitered bend with the ridge phase-matching feature. The simulation provided a close approximation of what was measured, but the measured data is invaluable for realizing an effective system.

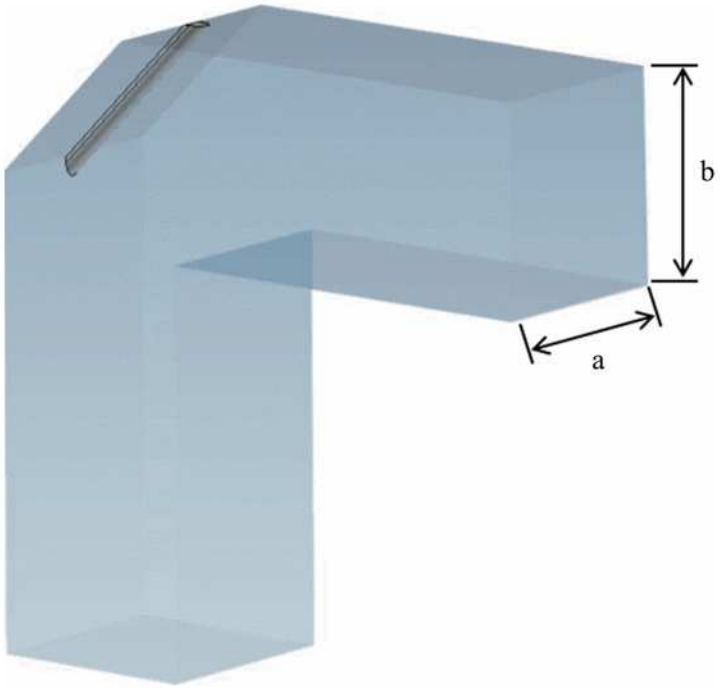

Figure 3.5: CAD model of square waveguide and mitered bend. The waveguide face is square, a is equal to b in this case, and it propagates orthogonal waveguide modes. The phase matching feature is seen along the length of the mitered bend.

Source: [14]

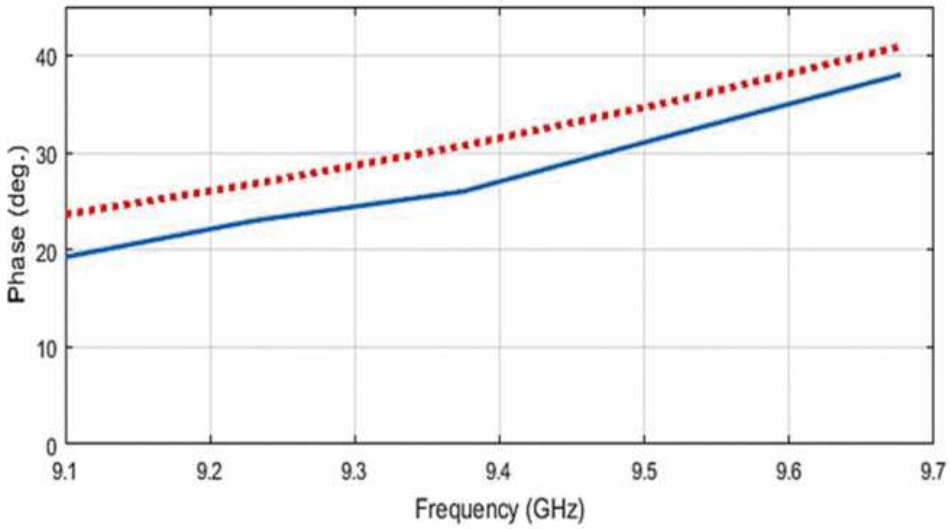

Figure 3.6: Simulated phase difference (solid-blue) and measured phase difference (dashed-red).

Source: [14]

3.3 Fabricating V/W-band waveguide

The RF subcomponents in the V/W-band antenna system are restricted to waveguide, especially since the losses in other transmission lines types are exceedingly high at these frequencies. Waveguide suitable for V/W-band frequencies are not yet widely available as commercial off the shelf components. It is difficult to realize waveguide with these dimensions, and especially when considering features such as couplers, splitters, and waveguide transitions. Selecting commercial off the shelf waveguide components to realize complex networks can still be prohibitively expensive. The waveguide network for the multibeam V/W-band communication system requires a custom block with a straight forward fabrication process.

3D printing, metal additive manufacturing, and selective laser melting are all manufacturing techniques that are being actively developed to realize waveguide suitable to operate in these frequency ranges. The dimensions required for V/W-band can be machined, although they are pushing the limits of such a process. Complex features, such as waveguide splitters, are not reliably manufacturable in most applications. Experiments have resulted in waveguides that lose an extra 1 dB due to machining tolerances, and there can also be impacts on the phase relation between some hybrid splitters. Even trivial waveguide transitions such as a 90-degree bend at these dimensions can prove to be difficult to manufacture. Bends are not easily machined at these dimensions, and new techniques are worth exploring to realize transitions.

The process of fabricating V/W-band waveguide features is illustrated in Verploegh [15]. In the paper they discuss the processes available to manufacture waveguide to be used for V-band and W-band applications, including analyzing the tolerances that are inevitable in a manufacturing processes and how they impact RF performance. Waveguide sections were manufactured and tested, as shown in Figure 3.7, using materials specific to the machining processes, which is an important consideration for these sensitive components.

Waveguide design through simulation allows for a design in an ideal setup, using thin PEC as walls without machining imperfections can be misleading. When choosing a manufacturing method, it is important to consider what machining features that it introduces to the waveguide,

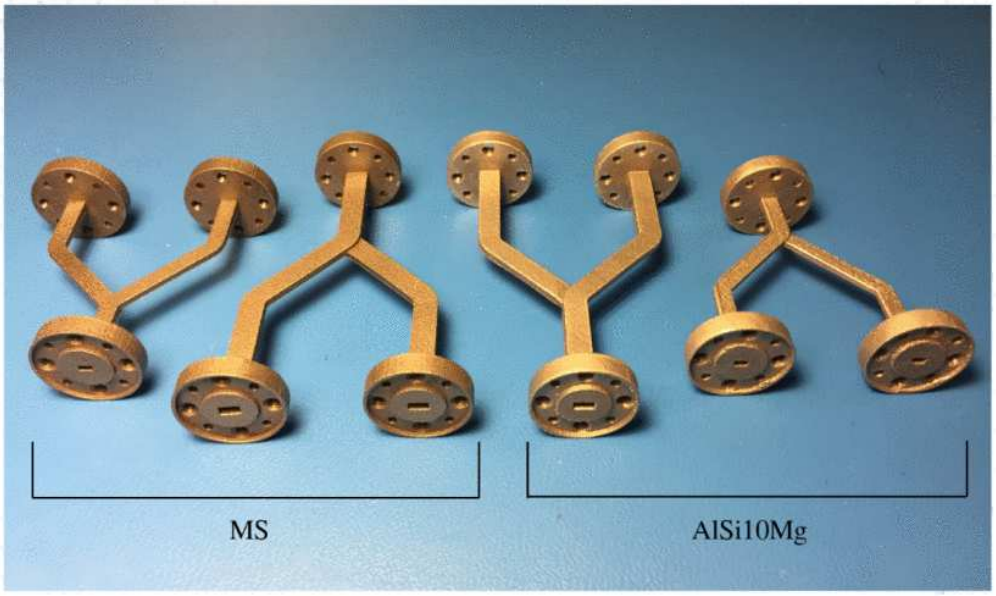

Figure 3.7: Waveguides fabricated utilizing new machining methods to realize small components.

Source: [15]

and how that may impact the RF performance. For instance, a mitered bend that is machined has discrete steps along the bend, rather than a perfectly smooth surface. Waveguide corners also cannot be machined perfectly square, there is a corner radius. The paper documents that the manufacturing methods employed degrade the performance by increasing the losses by a significant amount.

Another aspect of analysis was the septum wall used to divide two waveguide sections. Tolerance analysis was performed for a feature that is more vulnerable to machining imperfections, based on the offset in tilt angle of the wall, pictured in Figure 3.8. The authors observed from simulation that an offset of even 1 degree causes a noticeable amplitude imbalance, and up to a 3 degree slant has the potential to cause an amplitude imbalance of over 0.5 dB.

The impact of the tolerances resultant from selective laser melting and other manufacturing explicitly show the requirement of high precision methods for this category of devices. A conclusion can also be drawn that the mechanical designs must consider manufacturability as a top priority when considering RF performance, as a wall 50 microns thick is very susceptible to machining tolerances when stretched across the length of a waveguide section. Experimental analysis shows

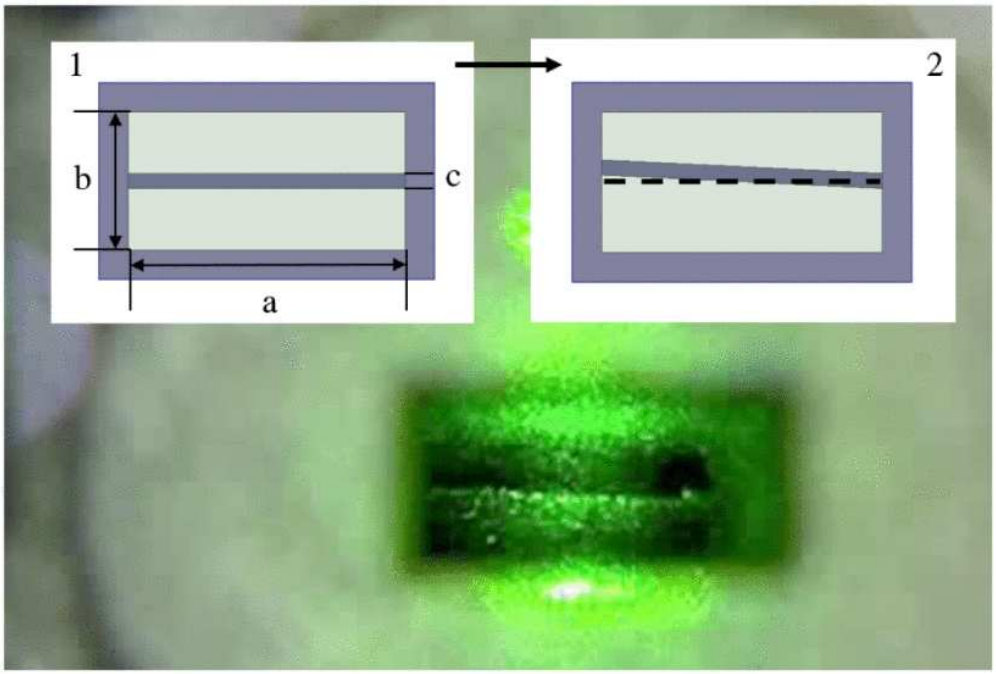

Figure 3.8: Tolerance analysis of a septum waveguide wall.

Source: [15]

the consequences of imperfections such as increased insertion loss, between 1 and 2 dB, which may be unacceptable for the waveguide transmission system which ideally has negligible insertion loss.

Chapter 4

V/W-band Telecommunication System Design

4.1 Introduction

The V/W-band telecommunication system is a space-based antenna system capable of dual-circularly polarized, dual-band, muiltibeam wireless communication system. This chapter focuses on the the design of the complete RF system, which was achieved through analysis, simulation, and prototype testing. Several RF subcomponents were be developed and integrated into the waveguide feed assembly to realize the antenna architecture, as, shown with the system block diagram in Figure 4.1. The frequency selective surface (FSS) provides the full-duplex communication capability with this system. The offset fed parabolic reflector is analyzed with the feed horn assembly to realize 19 spot beams within the beam space. The system architecture provides 19 independent transmit and receive beams, each beam having a 0.3-degree beamwidth, and spaced into a 2-degree beam space, to realize the MIMO functionality. The V and W, transmit and receive bands operate within 71-76 GHz and 81-86 GHz to provide a 5 GHz system bandwidth.

The challenges to realize this design include manufacturing waveguide channels with millimeter wave features that operate in V/W-band. All 19 independent waveguide channels must fit inside of the feed horn assembly, constrained by the size of the feed aperture. The waveguide transitions, stepped septum polarizers, and the 90-degree bend, all necessary to realize this system each require high precision machining and careful assembly. To reduce the risk in manufacturing, waveguide coupons are built to hone in the fabrication process throughout the development. Successfully fabricating waveguide coupons helps to ensure that each channel is realized in the feed horn prototype without critical issues. The waveguide transitions, including the 90-degree mitered bends, the septum polarizer, and the lofted waveguide section were built and tested as full-scale prototypes before the final prototype feed array unit is machined and assembled.

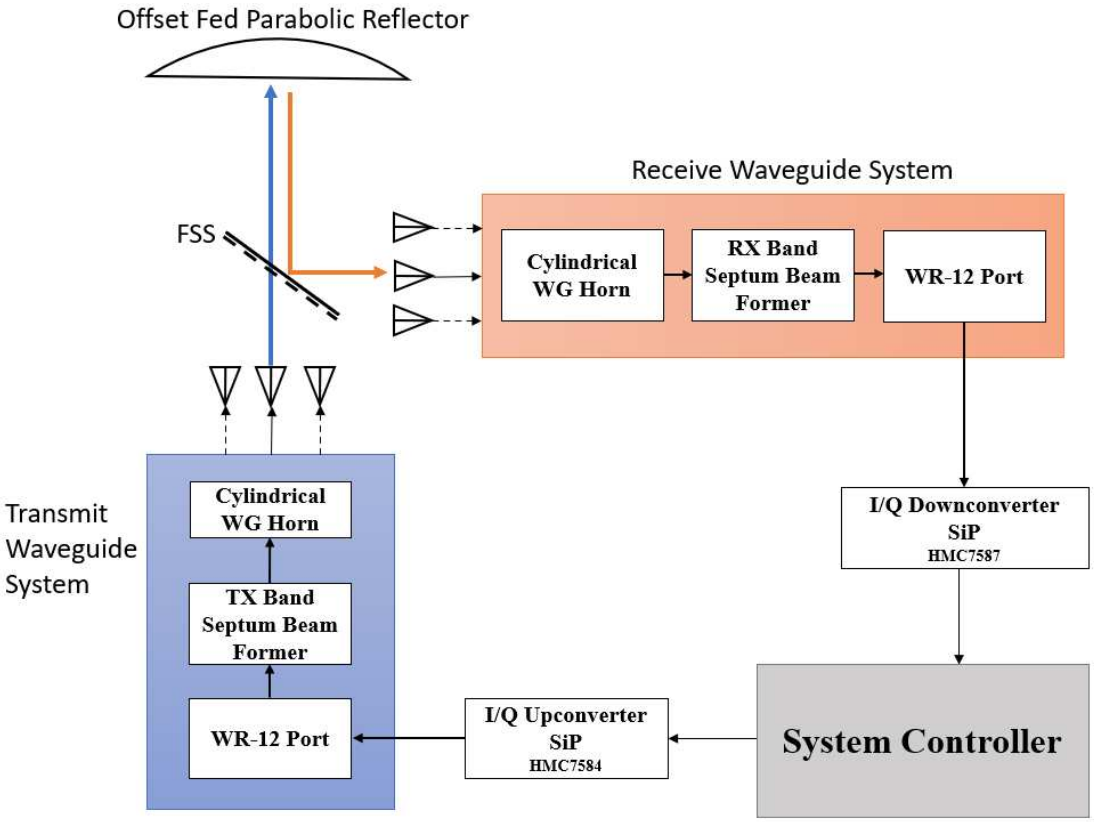

Figure 4.1: Block diagram of the V/W-band antenna and communication system that was developed. The primary development is in the waveguide systems, and the waveguide transitions are discussed in detail in this section. The offset fed parabolic reflector was designed and evaluated in conjunction with the feed array fed by the waveguide system. The Frequency Selective Surface allows for simultaneous transmit and receive operation, and allows for the use of a single primary reflector for both bands, reducing system complexity.

The offset fed parabolic reflector system has critical features in the spacing of the feed cluster and positioning of the feed horns. The system is simulated using an ideal feed aperture and reflector designed in CST MWS. Simulated far field beam patterns for the feed aperture and the reflector were analyzed to determine the aperture efficiency, which is related to the side lobe levels and edge taper for the antenna system. Analysis was also performed using simulations to ensure there is no blockage in the field of view for the reflector. Reflector analysis provides simulated beam pattern results that are essential to verifying the performance of the realized prototype system. Peak directivity, beam shape, and cross-pol isolation are all critical aspects of this design.

4.2 Millimeter Wave Component Design

4.2.1 Square Waveguide and Mitered Bend

The waveguide system interfaces with WR-12 waveguide ports on the frequency converter modules. The transmit modules mix LO and IF inputs to the link carrier frequency and amplify the signal. The receive modules undo these operations by amplifying the received signal once again, and then mixing down the received signal to the lower IF band. The CAD models for these modules are shown in Figure 4.2, showing the module LO and IF input, power and control, and waveguide ports. The flange for this waveguide port is non-standard due to the size constraints, so the beginning of the waveguide feed horn block has a non-standard WR-12 flange interface.

The upcoming transitions determine the waveguide geometries to follow the module input. The input port transitions to the septum polarizer, placed inside a square waveguide section, with rectangular waveguide. The square waveguide section includes a 90-degree mitered bend to align the feed horns within the cluster, and after the bend the square waveguide transitions to cylindrical waveguide. The square waveguide and mitered bend model is seen in Figure 4.3. The square waveguide dimensions for transmit and receive bands required a side length of 2.54 mm and 2.29 mm, respectively. With these parameters, the model was simulated to obtain magnitude and phase transmission results, which are shown in Figure 4.4 and Figure 4.5. The simulation utilized the F-solver and ideal waveguide ports exciting the two orthogonal modes that propagate in the square

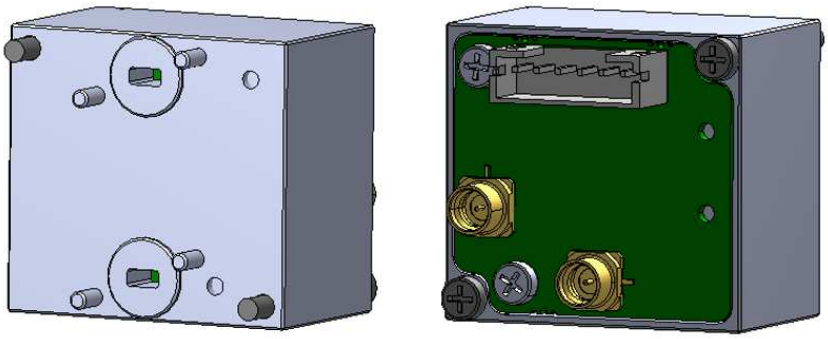

Figure 4.2: CAD Model of frequency mixer modules. The image on the left shows the WR-12 waveguide outputs from the SiP, on the right is the LO and IF inputs to the module as well as the 6-pin power and control connector.

waveguide section. The simulated results denote these orthogonal modes as the E-plane and H-plane results.

WR-10 provides a match for the square waveguide section in the transmit band, and is the closest option for the receive band to best integrate with the square waveguide section. The septum polarizer contained in the square waveguide has a non-zero thickness, and this must be accounted for while designing the transition from rectangular to square waveguide. A practical machining requirement to realize standalone walls is a thickness of 0.020" or 0.508 mm. The result of this requirement is that the WR-10 section *b* dimension must fit the interface gap, illustrated in Figure 4.6. Rather than including a taper or other waveguide transition, simply modifying the WR-10 *b* dimension is sufficient for this application. The *b* dimension does not have an impact on the dominant mode that propagates in rectangular waveguide. Therefore the *a* dimension matches the square waveguide side length, 2.54 mm and 2.29 mm for transmit and receive waveguide blocks, respectively, and the *b* dimension were modified from 1.27 mm to 1.106 mm and 0.889 mm for transmit and receive waveguide channels to accommodate the septum polarizer width.

The waveguide sections have to include a transition from the WR-12 waveguide ports on the frequency converter modules the the modified WR-10 waveguide runs. This transition is accomplished by have a gradual loft between the WR-12 face and the WR-10 face, the key parameter is

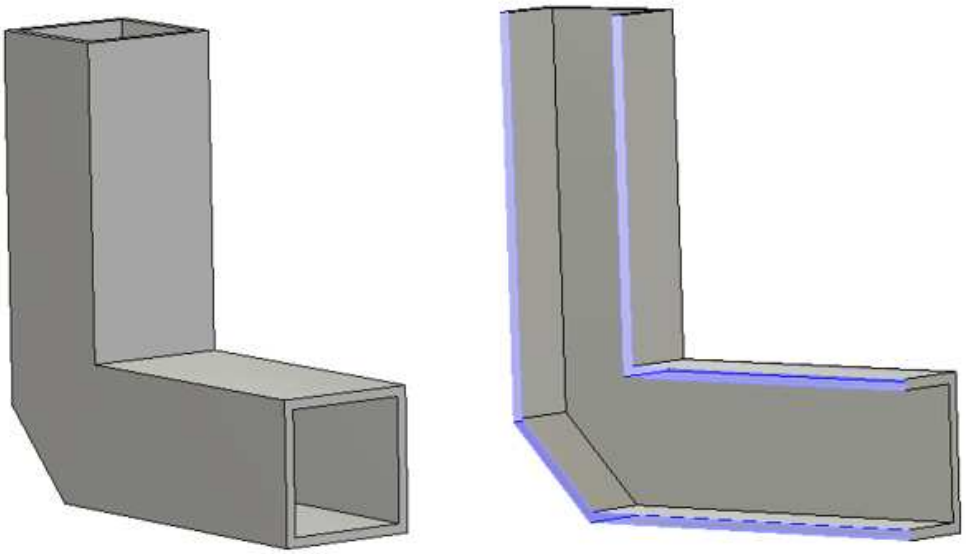

Figure 4.3: The perspective view and sectioned view of the a mitered bend square section CAD model used to evaluate the mitered bend. The mitered bend is made at a 45 degree angle with a length of $\lambda/2$.

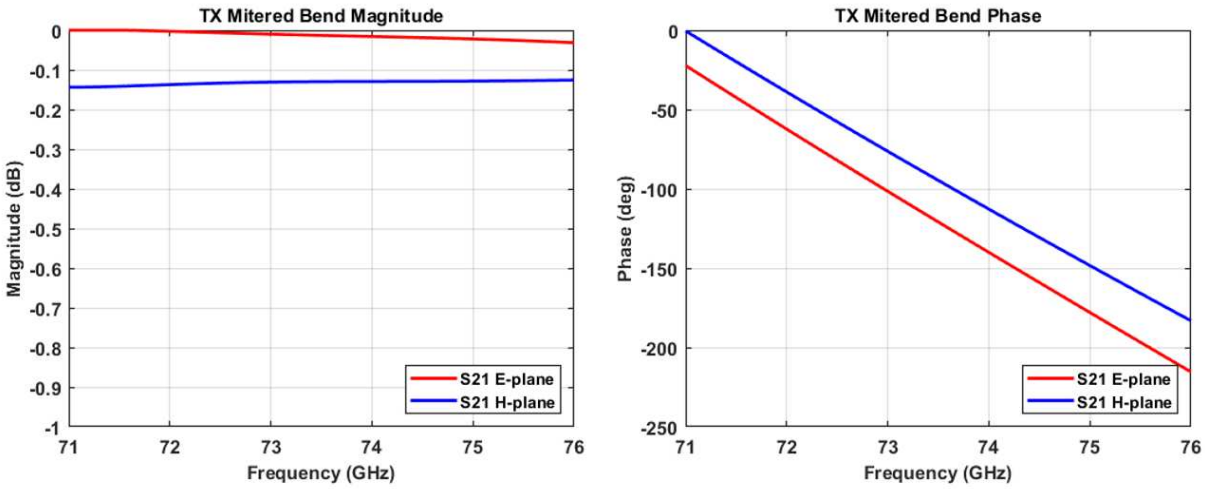

Figure 4.4: The transmission results of a two-port simulation including the square waveguide section and the mitered bend for the transmit band waveguide block. The insertion loss a maximum of 0.15 dB for either waveguide mode. The phase lag between the orthogonal waveguide modes due to the mitered bend.

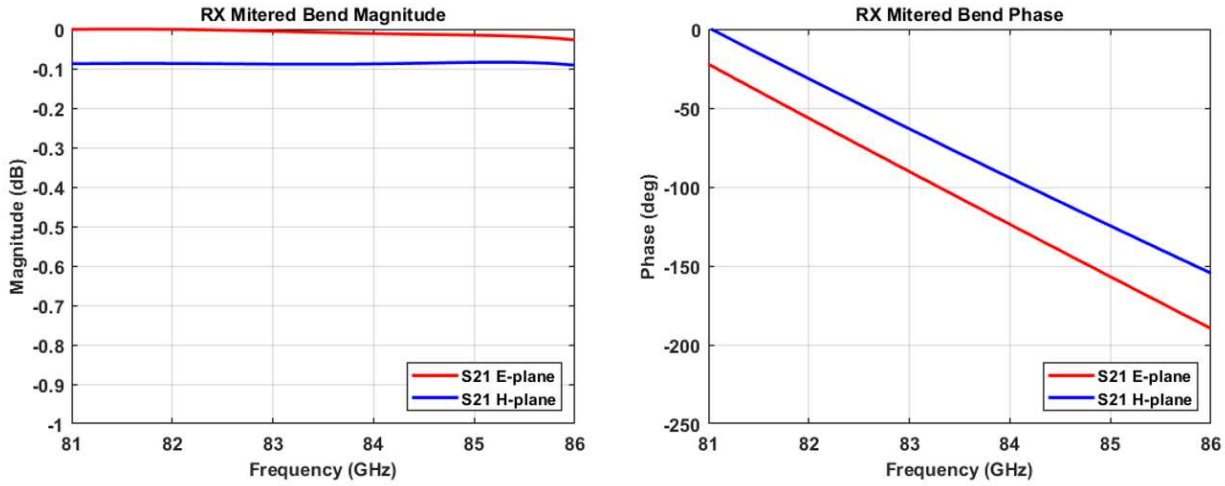

Figure 4.5: The transmission results of a two-port simulation including the square waveguide section and the mitered bend for the receive band waveguide block. The insertion loss a maximum of 0.09 dB for either waveguide mode. The phase lag between the orthogonal waveguide modes due to the mitered bend.

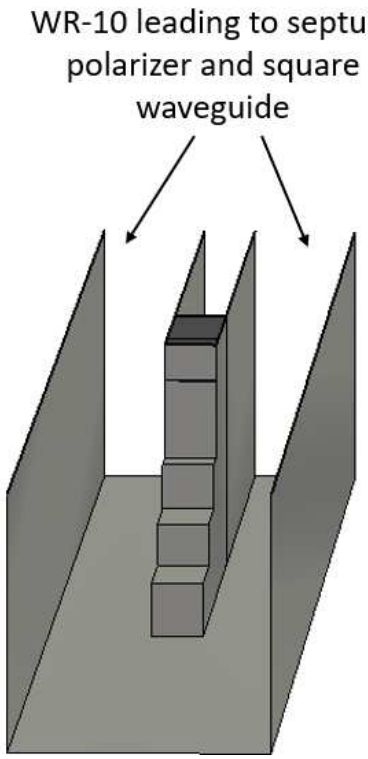

Figure 4.6: The junction between the modified WR-10 waveguide and the septum polarizer in the square waveguide section. The septum thickness must be accounted for as well to integrate the waveguide inputs.

that the lofted length is 2λ. This transition is straight forward and is included in some waveguide prototype models.

Prototypes were built and tested in a bench top settings to validate the designs and the manufacturability of these components. A standard WR-10 straight waveguide section was manufactured to determine the reliability of machining these small channels. An E-bend and H-bend waveguide coupon was built using standard WR-15 sizes for testing convenience to validate a mitered bend in both waveguide modes, the CAD models are shown Figure 4.7 and include a standard WR-15 waveguide flange. The lofted transition was validated using the septum polarizer coupon, discussed more in the next section, and it transitions from a WR-15 interface to the modified WR-10 dimensions.

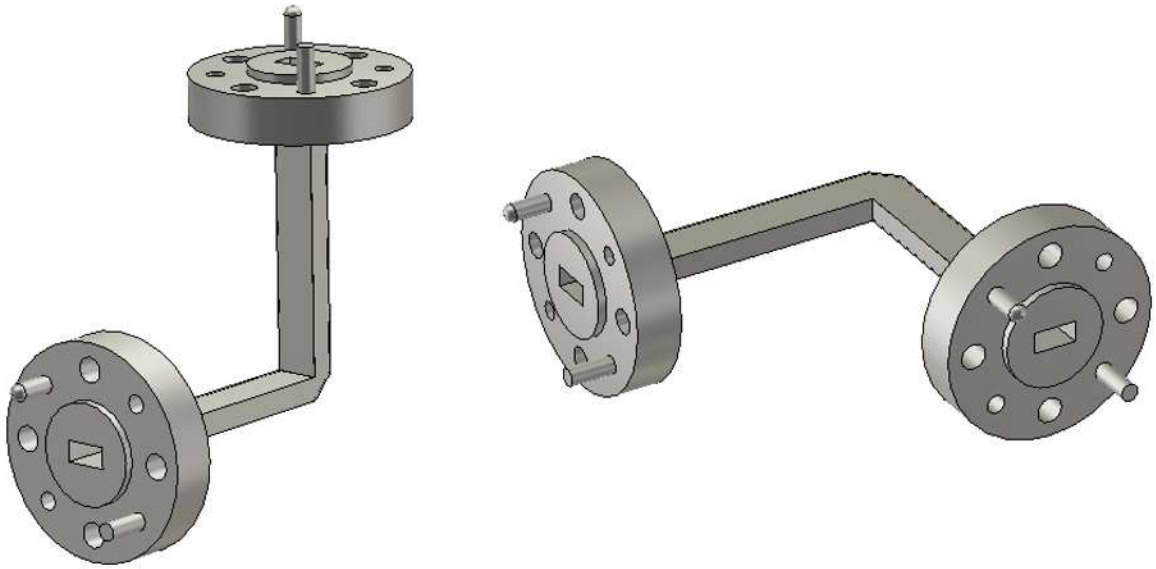

Figure 4.7: E-bend (left) and H-bend (right) WR-15 CAD models to be machined and tested with a VNA.

4.2.2 Septum Polarizer

The frequency converter modules interface with a linearly polarized port for the waveguide system. Inside the waveguide block, the beam was transformed from the linear input into two orthogonal modes to create a circularly polarized wave in the transmit block, and vice versa to interface with the receivers. A septum polarizer is a 3-port device resultant from a conductive wall that gradually steps down to reveal a waveguide junction. There are applications from rectangular waveguides directly into circular or square waveguides in which a standard, dominant, waveguide mode is equally converted into orthogonal waveguide modes. The principle elements for the waveguide system are the rectangular-to-square transition with the septum polarizer, and a square-to-circular waveguide junction that propagates the dominant TE_{11} mode after being excited by the two orthogonal modes, TE_{10} and TE_{01}, present in the square waveguide, after the septum polarizer transition [16].

The septum polarizer was baselined from Franco [17] which designed an L-band septum polarizer to transition from standard rectangular waveguide to circular waveguide. The L-band design is given parametrically, referring to Figure 4.8, to assist in the practical application of septum polarizers scaled to any frequency. This type of beam shaping feature can be used for a wide range of frequencies, and is only limited by the manufacturability of the features [18]. The septum polarizer was initially built with the steps scaled through the guidance of the paper, and simulations were ran to evaluate its performance in the transmit and receive frequency bands.

The septum polarizer simulation model included two rectangular ports at the terminals of the septum polarizer, where it transitions to the square waveguide section. The square waveguide section is terminated with an ideal square waveguide port, monitoring modes in both planes. The septum polarizer was included with parametrically defined steps, as indicated in Figure 4.8. After scaling the steps to the WR-10 and square waveguide, defined by the *e* dimension, the CST MWS Optimizer was utilized with the Evolution Algorithm with the design goals defined in Table 4.1 and Table 4.2. Two septum polarizers were independently optimized using this method, one for each band.

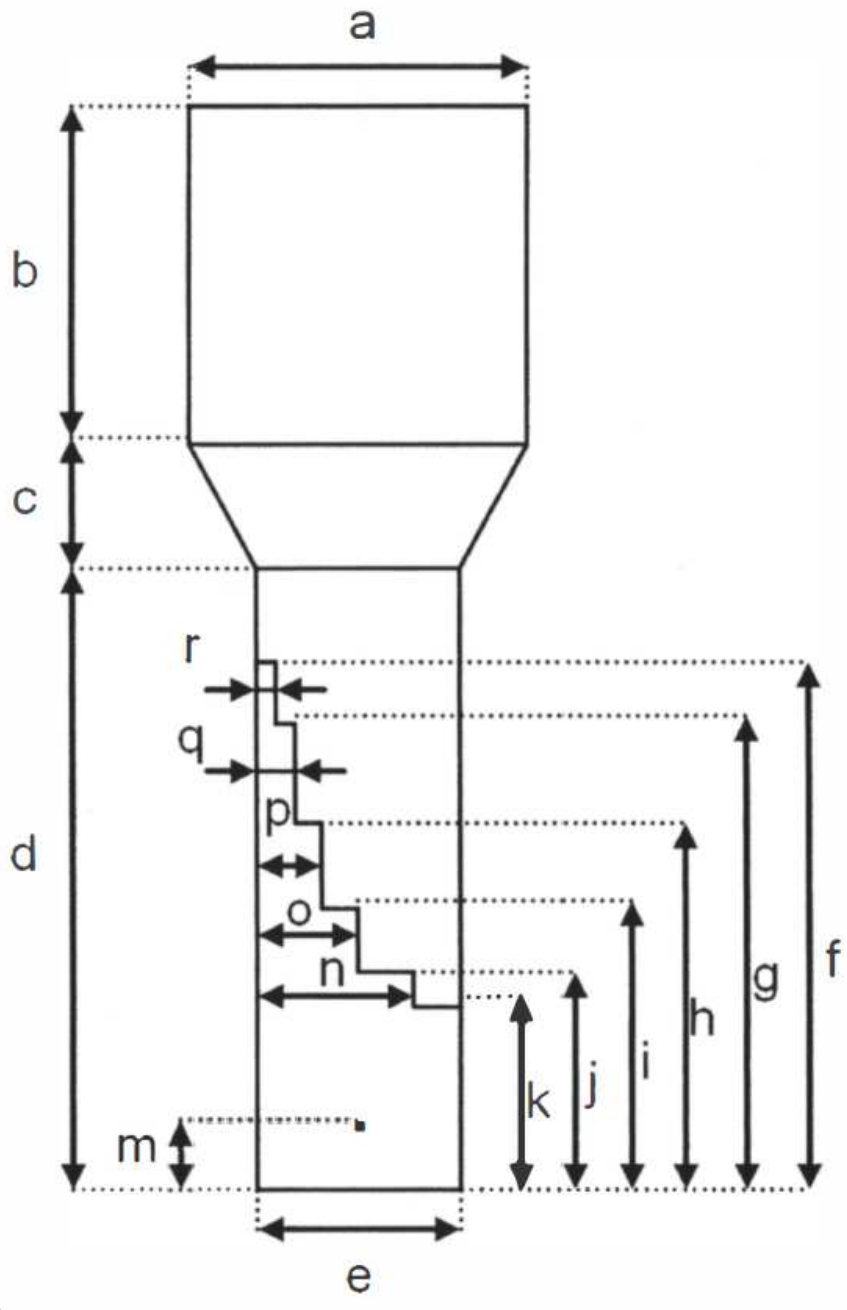

Figure 4.8: This is a representation of the septum polarizer design in Franco [17] with the dimensions defined parametrically. The *e* dimensions is the long dimension of the rectangular waveguide input, and consequently the first section of septum polarizer.

Source: [17]

Table 4.1: CST MWS Optimizer Goals for TX Septum Polarizer

Parameter	Goal	Frequency range	Weight
S3,1(1)	S31(1) = -3 dB	71-76 GHz	1.0
S3,1(2)	S31(2) = -3 dB	71-76 GHz	1.0
Mixed Result	S31(1)phase - S31(2)phase = 90	71-76 GHz	1.0
S1,1(1)	S11 < -20 dB	71-76 GHz	1.0
S2,1(1)	S21 < -20 dB	71-76 GHz	1.0

Table 4.2: CST MWS Optimizer Goals for RX Septum Polarizer

Parameter	Goal	Frequency range	Weight
S3,1(1)	S31(1) = -3 dB	81-86 GHz	1.0
S3,1(2)	S31(2) = -3 dB	81-86 GHz	1.0
Mixed Result	S31(1)phase - S31(2)phase = 90	81-86 GHz	1.0
S1,1(1)	S11 < -20 dB	81-86 GHz	1.0
S2,1(1)	S21 < -20 dB	81-86 GHz	1.0

Through this iterative process, the CST MWS Optimizer satisfied all design goals and determined the step scaling required for optimum performance in both the transmit and receive frequency bands, using the CMA Evolution Strategy as the algorithm. The amplitude imbalance remained within 0.1 dB and the phase imbalance was less than 10 degrees from the ideal 90 degree phase difference at their designed frequency, according to the full-wave simulation performed using the F-solver. A septum polarizer waveguide coupon was manufactured to validate this design and the manufacturability of these features. To perform these measurements with the available equipment, standard WR-15 ports were used and the lofted transition was implemented into the modified WR-10 waveguide section. The back-to-back septum polarizer was included in the square waveguide section so that standard measurements with a WR-15 port can be performed on a four-port device, providing an opportunity to do a thru measurement. The model used to simulate this coupon is shown in Figure 4.9 with example ports labeled.

The next step for the design of the septum polarizer is to once again optimize its step design to adjust the phase balance between the orthogonal modes to compensate other phase impacts in the waveguide transmission line. As mentioned in the previous section, the mitered bend delays the phase of one waveguide mode by nearly 20 degrees across the band in the simulated models, similar

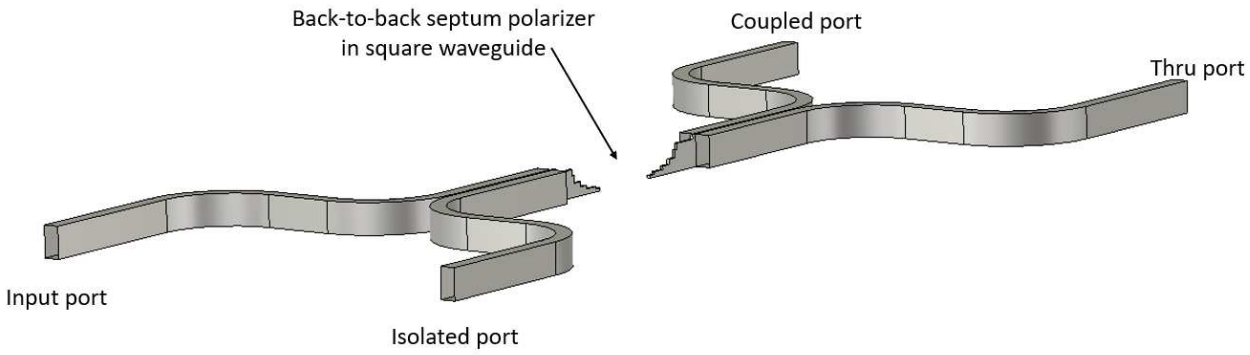

Figure 4.9: Simulated model for waveguide coupon. This four-port coupon validates the septum polarizer transforming a linear waveguide input on the input port, where it is transformed into orthogonal components of equal magnitude and then recombined and measured at the thru port.

to what was reported in [14]. The septum polarizer was then built with parametric in the application model, shown in Figure 4.10, and optimized using the same algorithm and optimizer goals. The septum polarizer was able to sufficiently compensate for the phase imbalance introduced by the next feature and maintain the design tolerance.

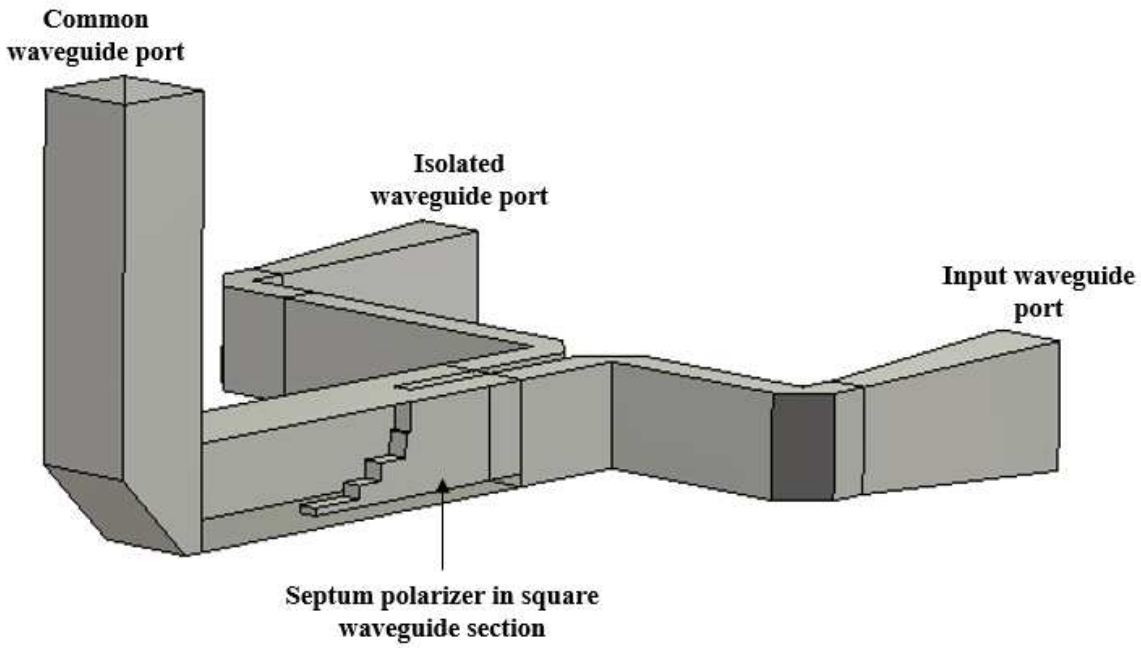

Figure 4.10: This model incorporates the major transitions in the waveguide section for a single channel. This model is used to tune the septum polarizer to compensate for the phase impact of the mitered bend. The effectiveness of the lofted transition from WR-12 to the modified WR-10 waveguide section is also verified.

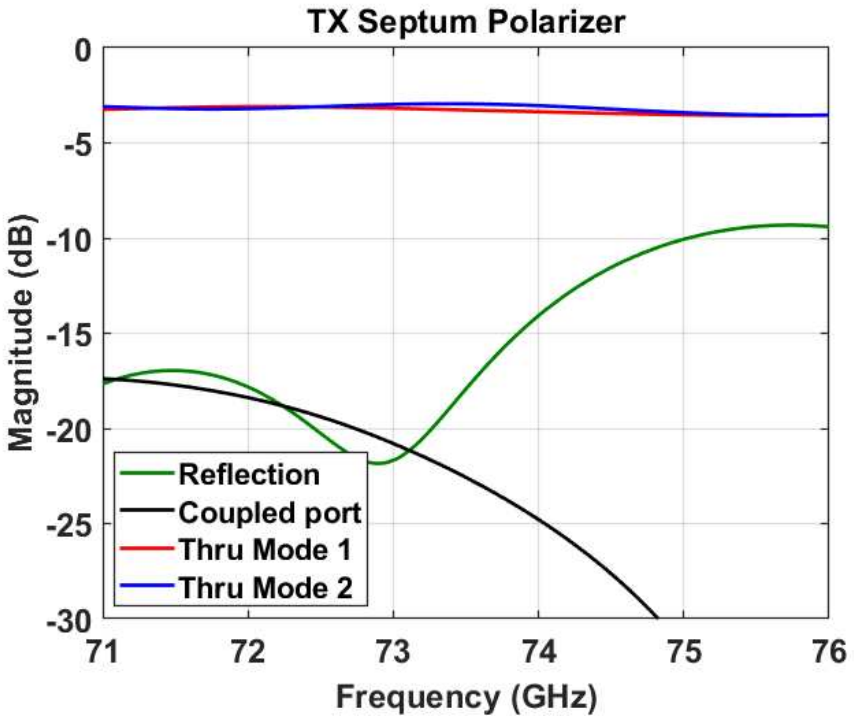

Figure 4.11: Transmit septum polarizer simulated S-parameters. The two thru mode are power split into equal parts, giving a -3 dB magnitude. The reflection is energy rejected at waveguide transitions. The coupled port is the other input of the septum polarizer.

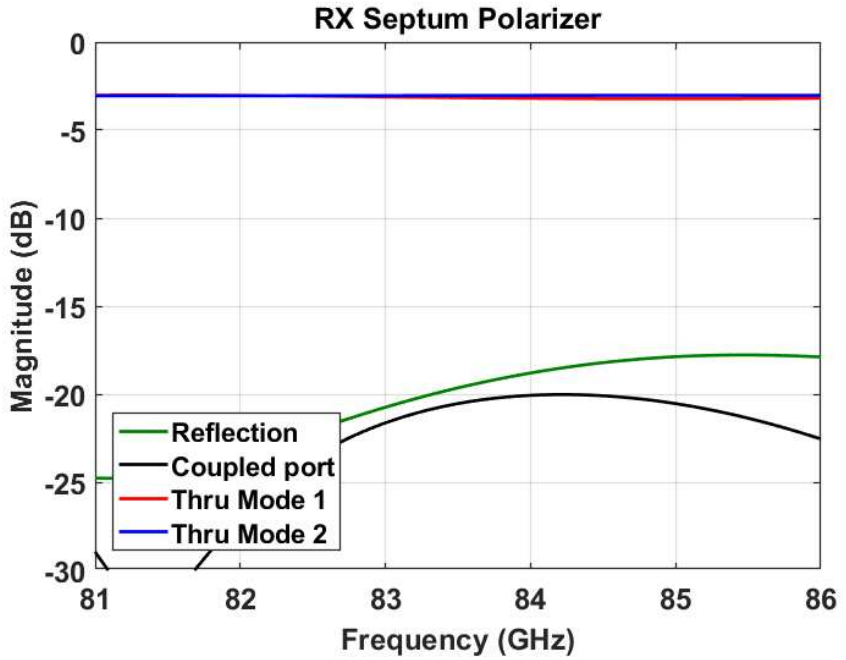

Figure 4.12: Receive septum polarizer simulated S-parameters. The two thru mode are power split into equal parts, giving a -3 dB magnitude. The reflection is energy rejected at waveguide transitions. The coupled port is the other input of the septum polarizer.

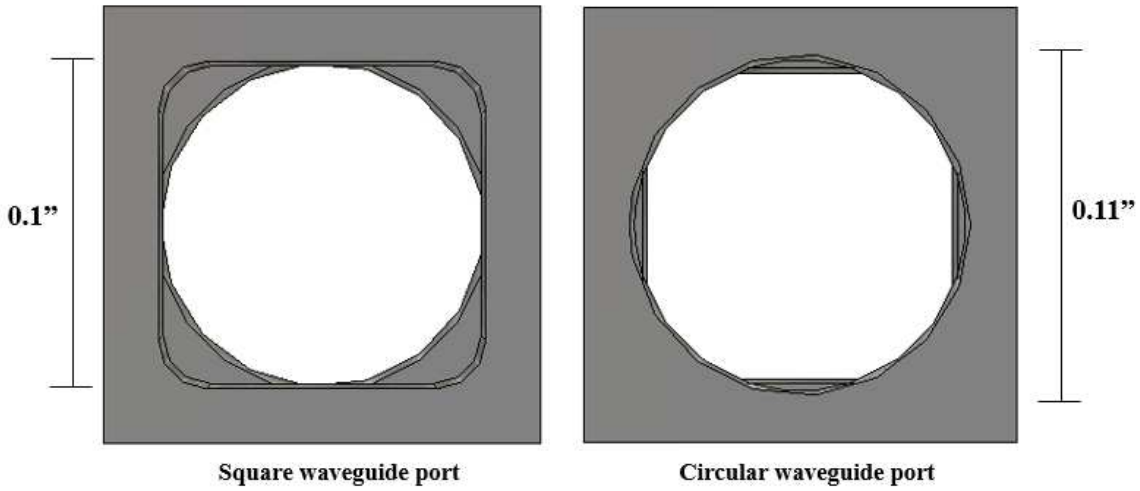

Figure 4.13: The square side length and diameter of a straight waveguide section for the transmit band, modeled in CST MWS, that includes the transition from square waveguide to circular waveguide. A corner radius is included for the square section in this model to better represent what is machinable for this feature. The length of the square and diameter of the cylinder are shown for the transmit waveguide section.

4.2.3 Square-to-Circular Waveguide Transition

The cylindrical waveguide requires a diameter of 2.54mm or 2.78 mm to operate above the cutoff frequency for the receive and transmit bands, respectively. These dimensions are close to the side length of the square waveguide leading to this transition in both bands. A transition from one size to the other would be very gradual if it was implemented over two wavelengths.

Typically, stepped or lofted transitions are used for waveguide size and shape transitions, such as the lofted waveguide to join the standard WR-15 interfaces with the modified WR-10 waveguide that connects to the septum polarizer transition. Due to the construction of the waveguide feed blocks, it is significantly easier to have an immediate transition from square waveguide to a circular waveguide with no lofts or steps. Analysis was done with CST MWS to observe any effects on transmission from this abrupt transition. The model includes radius corners in the square waveguide, an expected feature from machining, to give a more complete picture of the transition geometry. Simulations showed that this abrupt transition would introduce a typical insertion loss of 0.1 dB or less across the band, and reflections remained below -13 dB. It was determined that

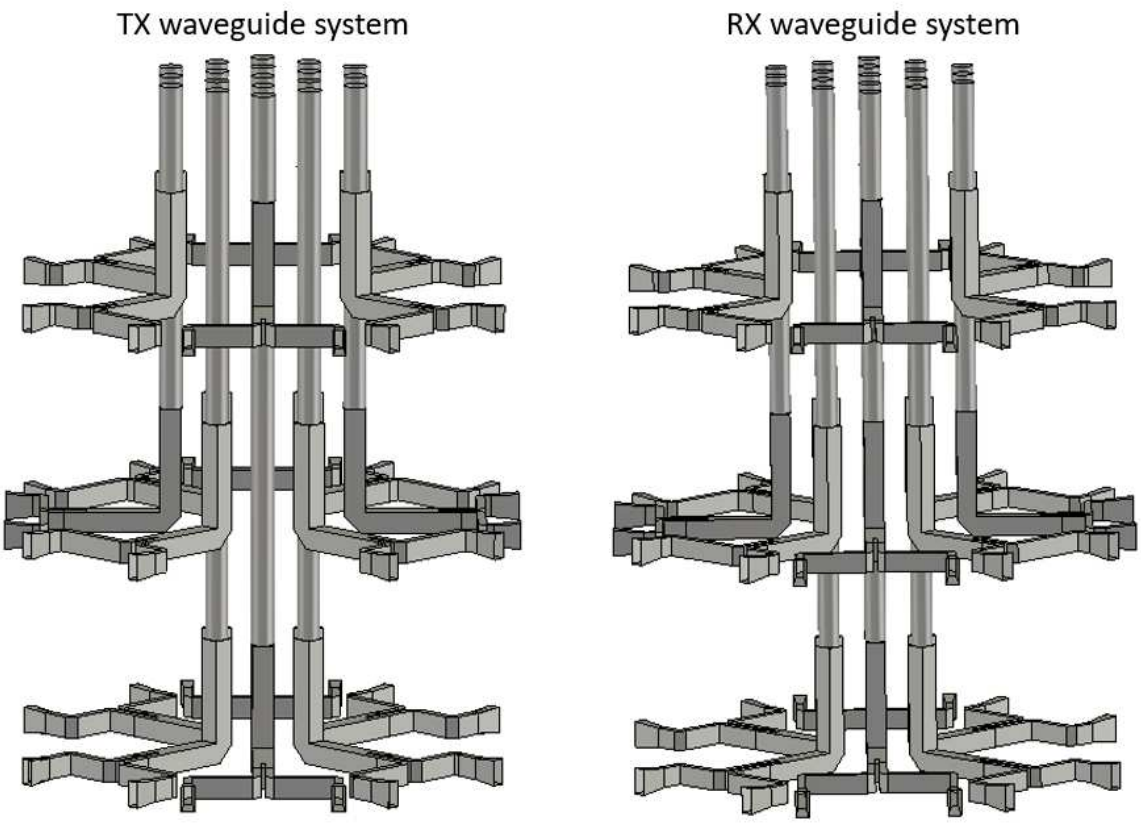

Figure 4.14: CST MWS models of the TX and RX plumbing inside the waveguide feed horn blocks. The TX and RX skeletons fit inside the same waveguide block for manufacture. They follow the same general structure, from the WR-12 waveguide input to the circular waveguide face directed towards the dish. There are 19 total waveguide runs in these images.

this transition is straight forward to implement and therefore is the best transition to the feed horn section, as it does not introduce significant losses or phase shifts.

4.2.4 Waveguide feed horn aperture

The waveguide system block terminates at the feed horn aperture. The 19 beam system waveguide terminals are cutoff at circular waveguide ends. All subsystems that have been discussed so far are included in this full waveguide block, shown in Figure 4.14 and Figure 4.15, for both the transmit and receive systems.

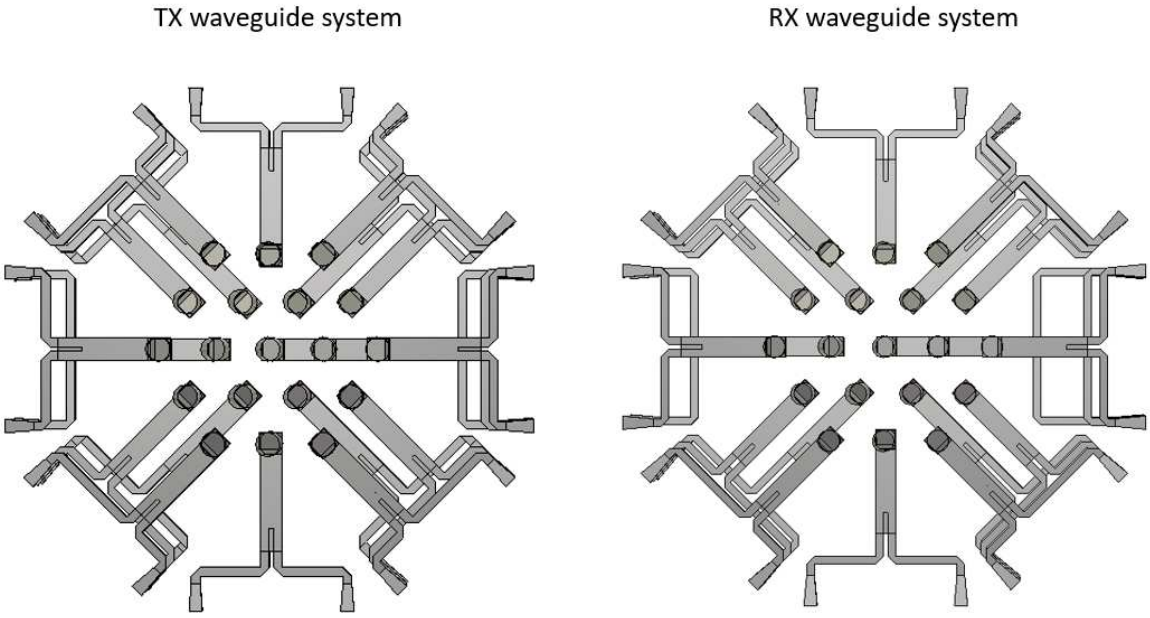

Figure 4.15: CST MWS waveguide models from the top perspective view.

The basis of the feed horn design begins with the feed horn aperture that is terminated from the waveguide system, which is analyzed in an isolated CST MWS model. The comparative model is an ideal waveguide model with all 19 cylindrical waveguide ends present. The relevant simulation models are shown in Figure 4.16. The simplified 19 beam system is modeled in a free space environment and constructed with PEC material. The models are excited by ideal waveguide ports that provide an ideal TE_{11} mode propagating in the cylindrical section. The farfield radiation patterns are simulated using these models, along with the S-parameters for the ports. Nearfield sources are also generated using these ideal models to provide a stimulus for simulations of the reflector dish that will be examined in the next section.

The simulated feed horn patterns and shown in figures 4.17 - 4.20 for the principal plane cuts. Figure 4.17 and Figure 4.18 and the $\phi = 0$ and $\phi = 90$. Figure 4.19 shows the TX and RX patterns for port 10 along its principal plane, and the same for Figure 4.20 for port 19, in the orthogonal plane. The simulated results indicate good performance for all beams, noting that the directivity of each beam has been maximized and the beam shapes optimally illuminate the reflector. The

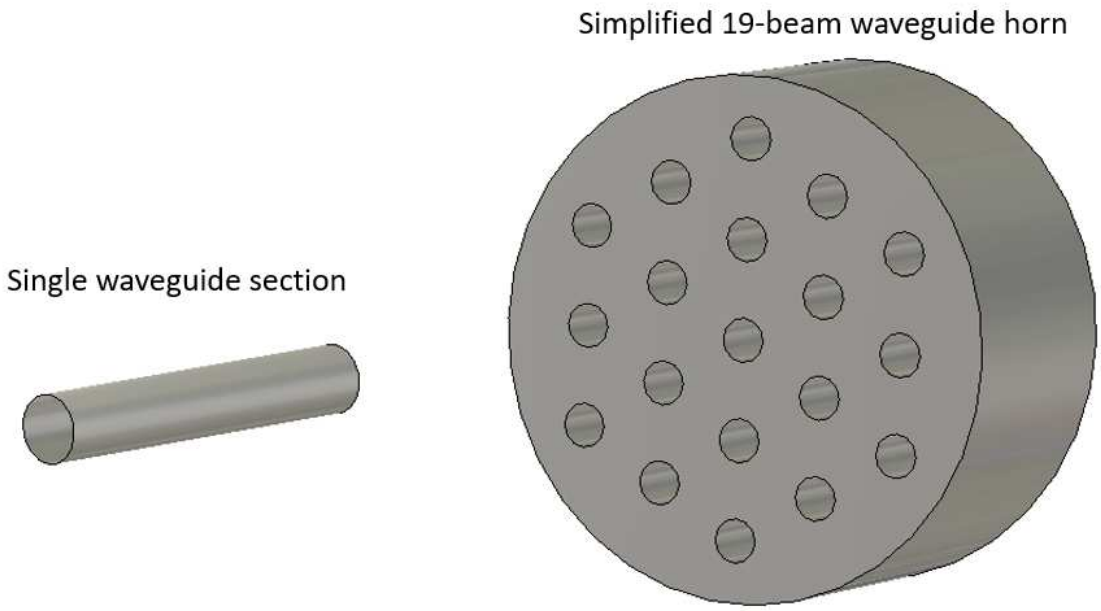

Figure 4.16: The single cylindrical waveguide section is simulated in a free space environment to provide a baseline for the 19-beam waveguide horn. The model is simple due to it eliminating all waveguide features except the cylindrical waveguide section for the feed horn, and it is excited by an ideal circular waveguide port. These models provide an ideal basis to model the reflector dish.

simulated results also indicate good isolation of the co-pol and cross-pol patterns, with over 30 dB of isolation at boresight in all cases.

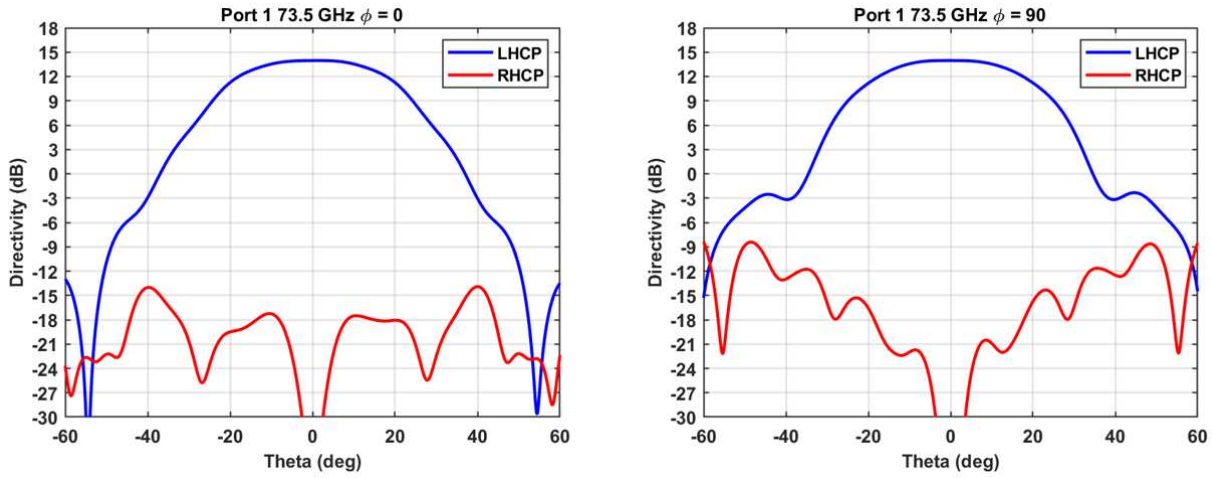

Figure 4.17: Simulated principal plane patterns for port 1 at the center frequency of the transmit band feed horn aperture.

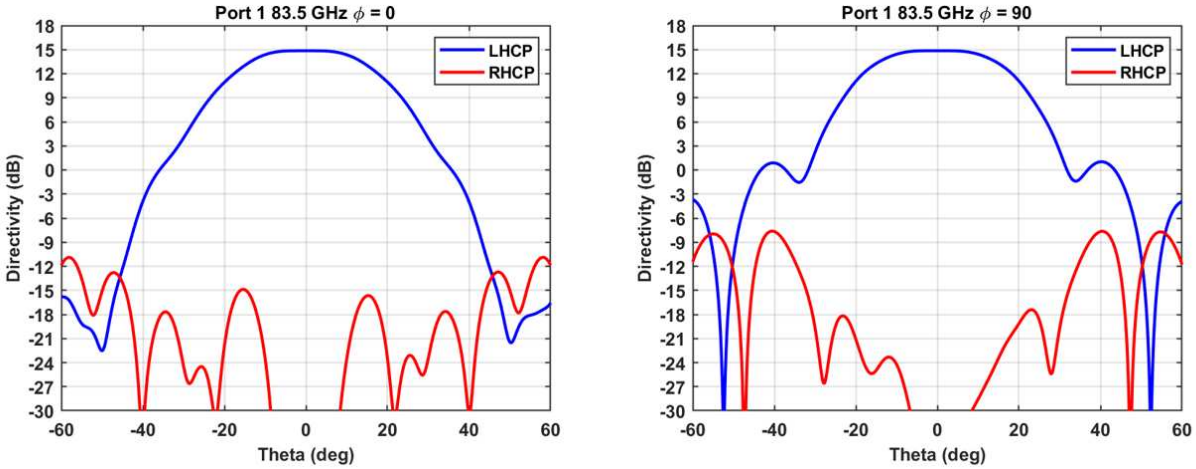

Figure 4.18: Simulated principal plane patterns for port 1 at the center frequency of the receive band feed horn aperture.

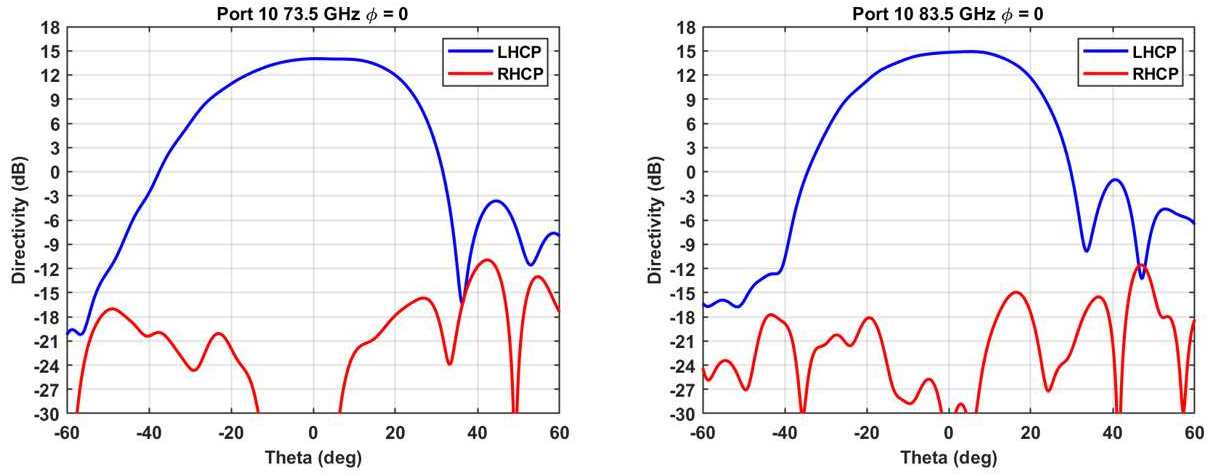

Figure 4.19: Simulated principal plane pattern for port 10 at the center frequencies of the transmit (left) and receive (right) bands.

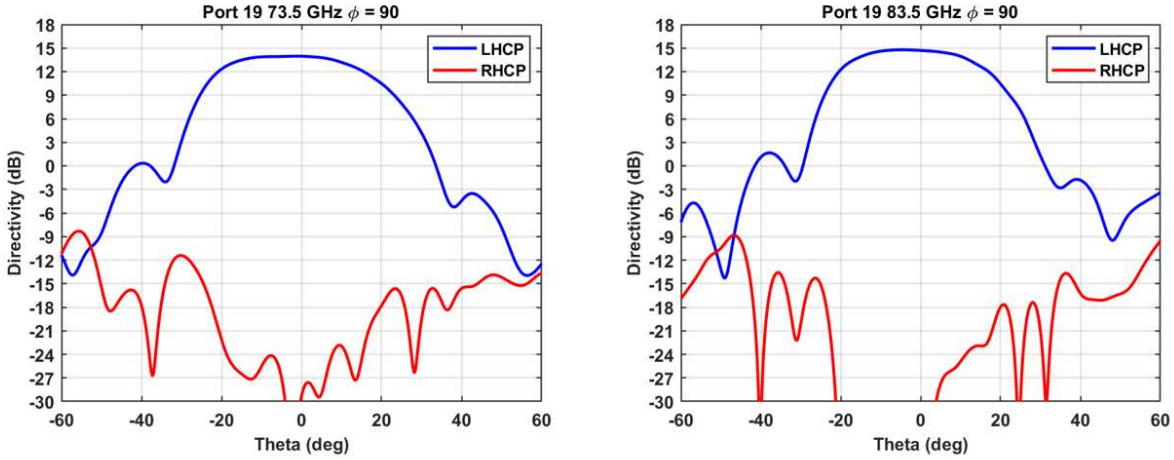

Figure 4.20: Simulated principal plane pattern for port 19 at the center frequencies of the transmit (left) and receive (right) bands.

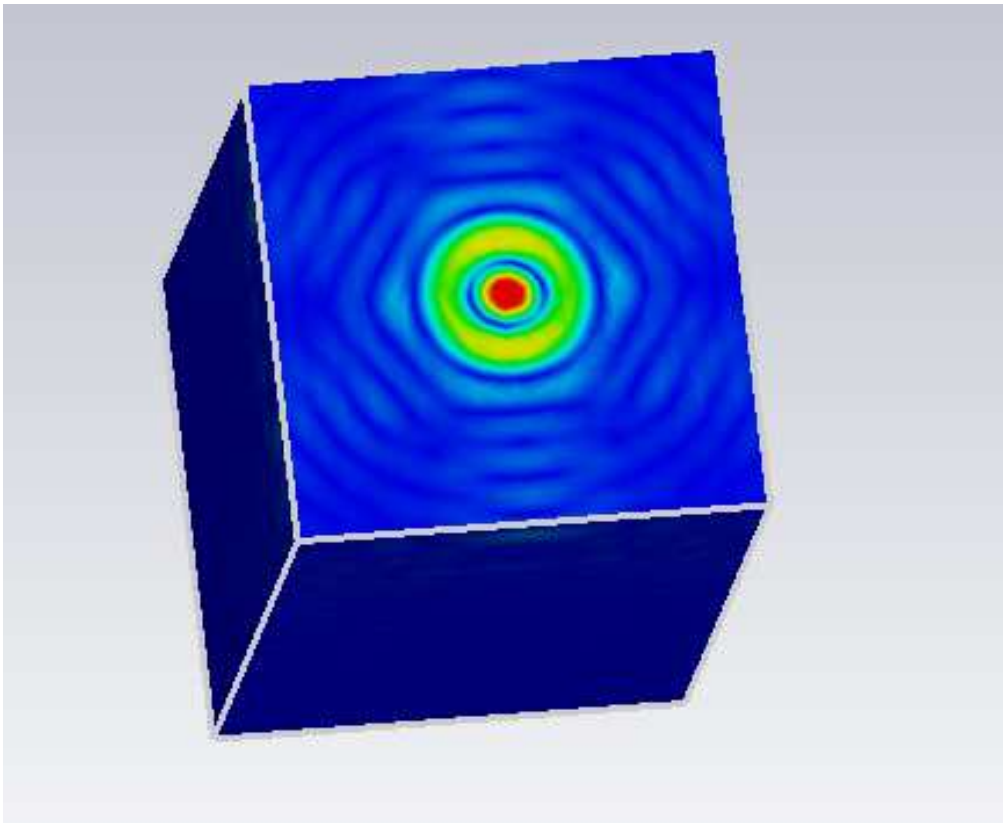

Figure 4.21: The near field source import to analyze large reflector model. The electric and magnetic fields are saved on a bounding box from the simulated horn models, and these fields are used to efficiently simulate the reflector system.

The reflector is electrically very large, and is built in a model without the fine electrical details of the feed horn. The Asymptotic Solver is the most optimal environment to characterize electrically large models. Separate iterations of the feed horn were modeled and simulated to generate near-field sources to be imported into the reflector model. Figure 4.21 shows the electric fields on the box of the near field source, preserving fields generated by the feed horn aperture.

The directivty far field result is examined from the reflector model. The simulations report expected main beam shapes, directivity, side lobe levels, edge taper, spill over loss, and the beam spacing. All of these parameters are considered along with the feed horn characteristics, and its pointing towards the reflector.

4.2.5 Reflector System

The multibeam system is designed to consist of 19 beams, each with a 0.3 degree beamwidth, that all fit within a 2 degree space. Waveguide feed horn spacing, and f/D ratios were analyzed to simulate how the 19 beams locate within their 2 degree overall beam space once reflected from the antenna dish. The ideal parameters for this system were and f/D of 0.97, very close to 1, and the spacing between each waveguide horn is 6.32 mm center-to-center.

The reflector was simulated in CST MWS by using an imported near field source that was generated from the feed horn model, shown in Figure 4.22 which used ideal ports to simplify the simulated source generation, while still being an accurate depiction of fields emitted at the feed horn. The reflector model has the near field source oriented towards the reflector, as shown in Figure 4.23. This is the model that is used to evaluate the offset fed parabolic reflector dish. This simulation setup is able to optimize the aperture location and inclination angle to optimize antenna efficiency. The farfield monitor allows us to record the individual beam locations, the beam directives, and the spacing between the beams. Another important result that can be gathered from this model is the shadow that is cast on the dish from the RF feed system. The feed must be positioned such that rays incident, within a plus or minus 1-degree angle of incidence from boresight, on the reflector are not blocked by the feed housing system.

Antenna Efficiency Results

The aperture efficiency was determined through simulation, using the F-solver, of the models mentioned above along with the farfield monitor defined at frequencies of interest. Table 4.3 lists the resultant parameters from simulation and analysis. The system results in an edge taper of -6 dB for both the TX and RX configurations , as indicated by the [reference to aperture efficiency diagram] and the results collected from these simulations. The co-polar and cross-polar performance of the reflector system is also shown in the following figures 4.24-4.31. The simulated isolation between polarization states is greater than 50 dB at the beam peaks.

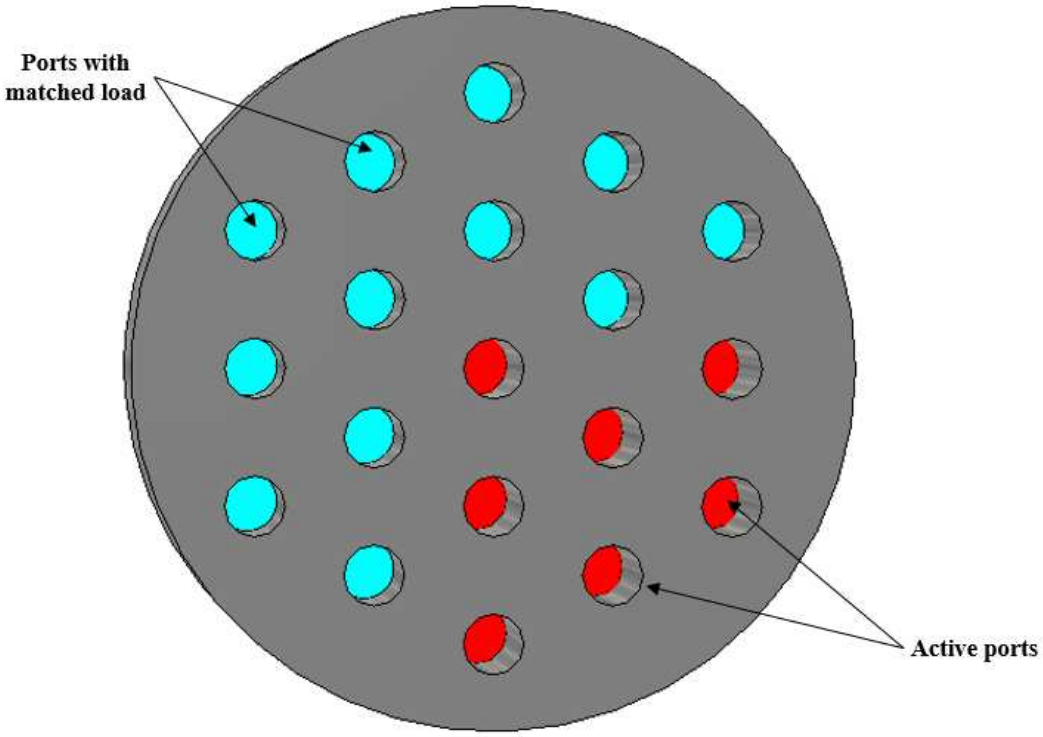

Figure 4.22: This is a simplified model of the feed horn face. The seven red ports are ideal circular waveguide ports, while the twelve light blue ports are terminated with a matched load. The feed horn can be full characterized with the rotational symmetry of the seven waveguide ports. The symmetry is additionally used in Figure 4.36 and Figure 4.37.

Table 4.3: Aperture Efficiency, A_e, simulation results

	Transmit	Receive
Frequency	73.5 GHz	83.5 GHz
Free Space Wavelength	4.1 mm	3.6 mm
Ideal Directivity	55.4 dB	56.5 dB
Simulated Directivity	52.7 dB	53.8 dB
First Side Lobe Level	-19.9 dB	-20.5 dB

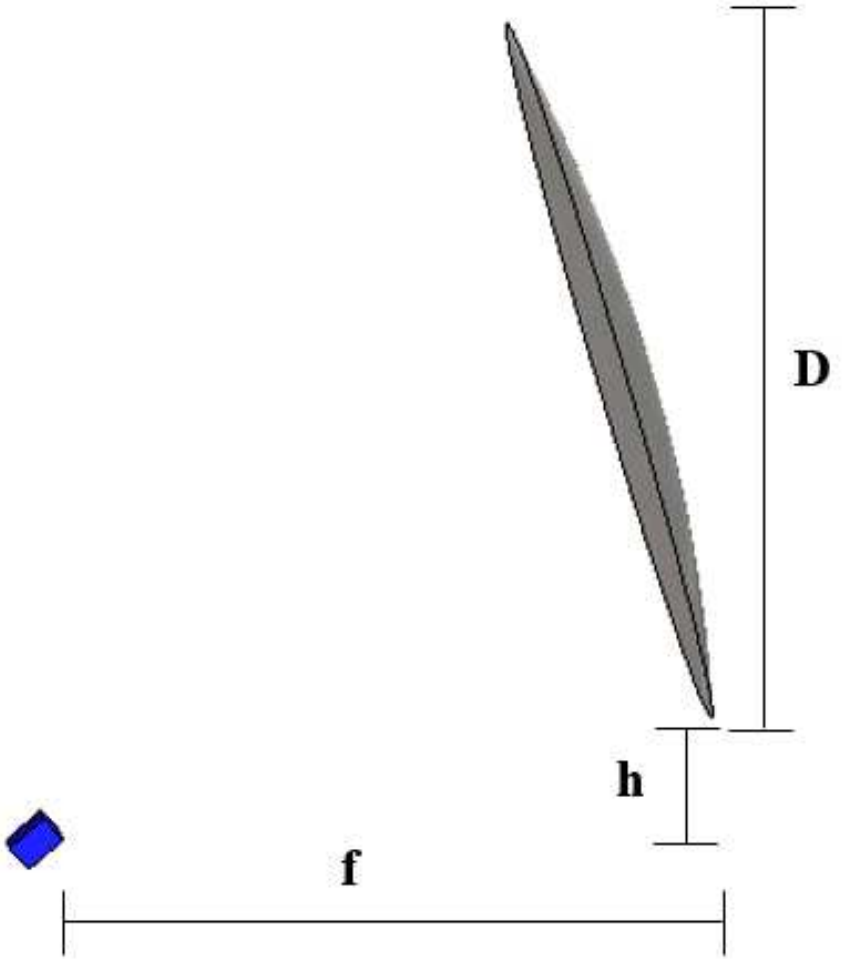

Figure 4.23: This model uses an imported field source, seen as the blue box, to evaluate the reflector dish, also shown. The key parameters for this system design are the height of the offset for the reflector dish, h, the diameter of the dish aperture, D, and the focal length, f.

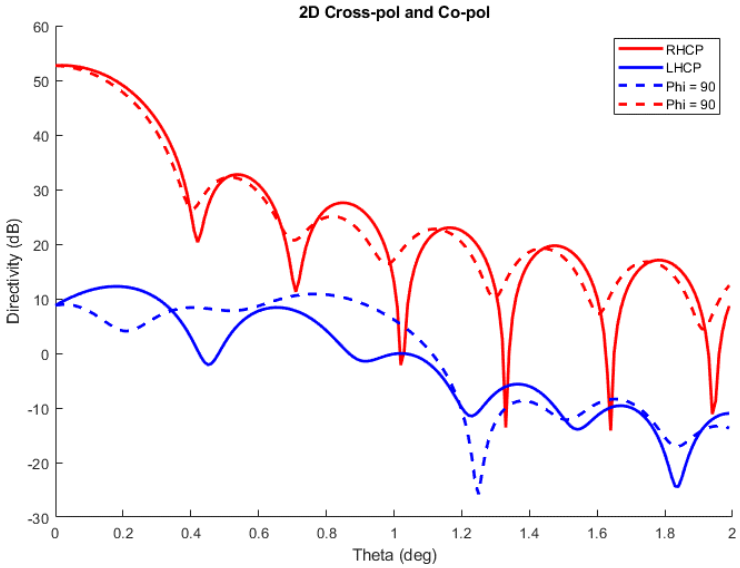

Figure 4.24: 2D cross-pol and co-pol radiation patterns for beam 1 (TX)

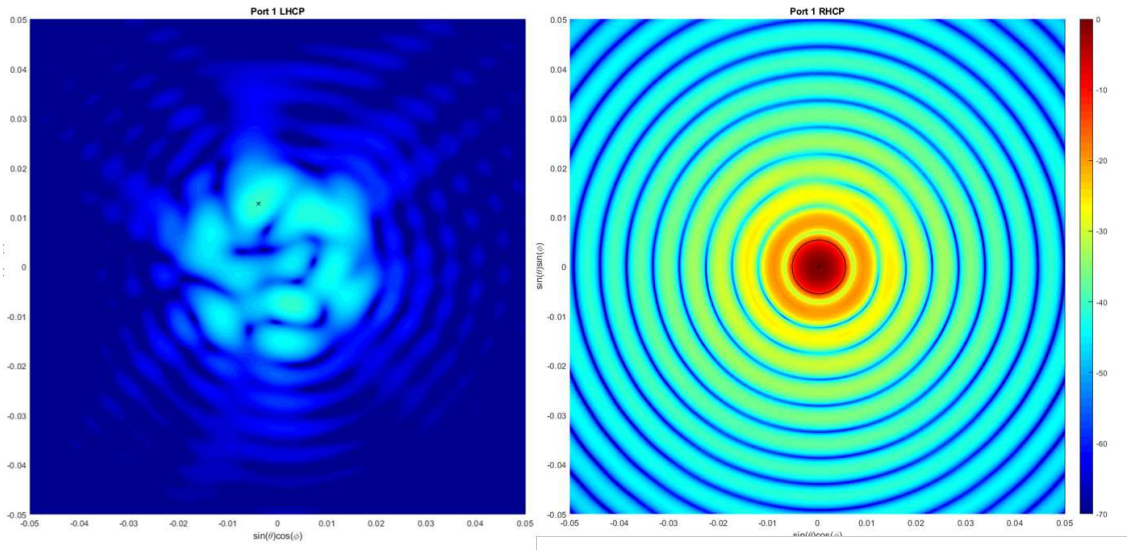

Figure 4.25: Cross-pol and co-pol radiation patterns for beam 1 (TX)

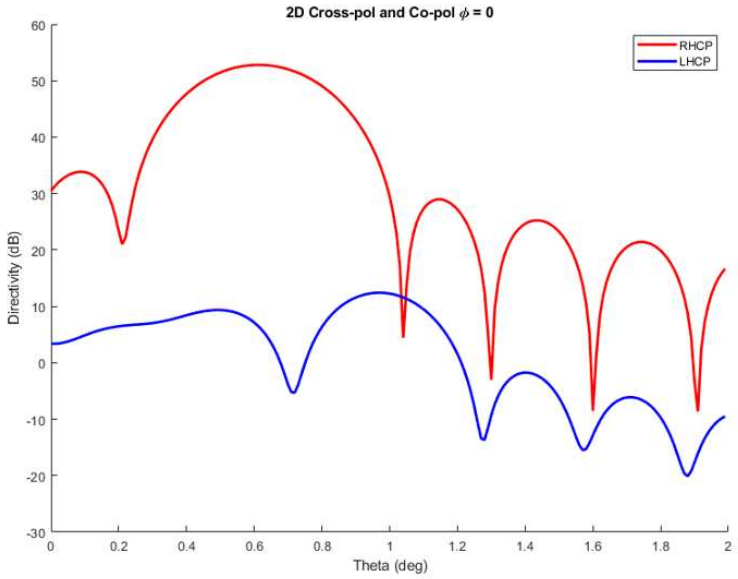

Figure 4.26: 2D cross-pol and co-pol radiation patterns for beam 10 (TX)

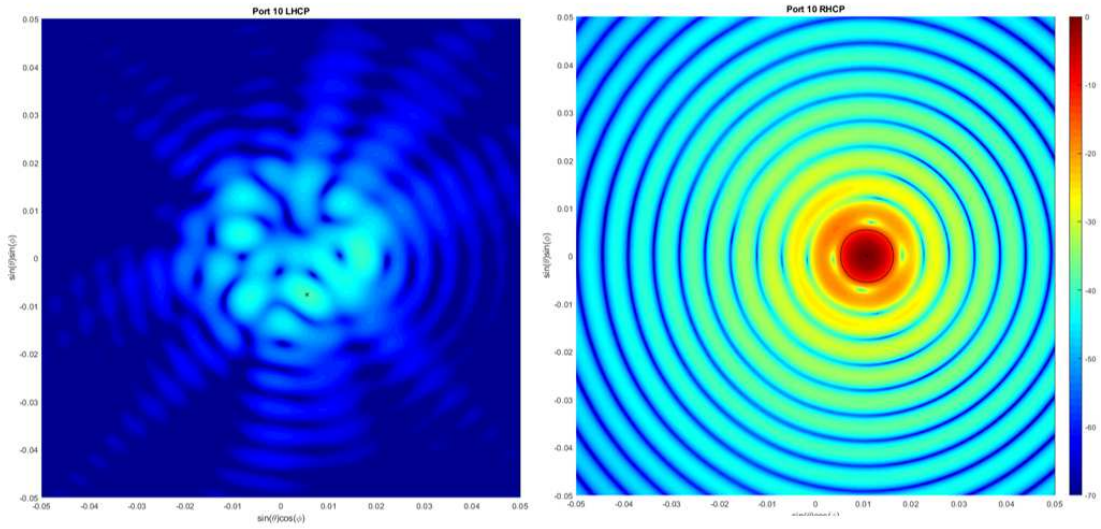

Figure 4.27: Cross-pol and co-pol radiation patterns for beam 10 (TX)

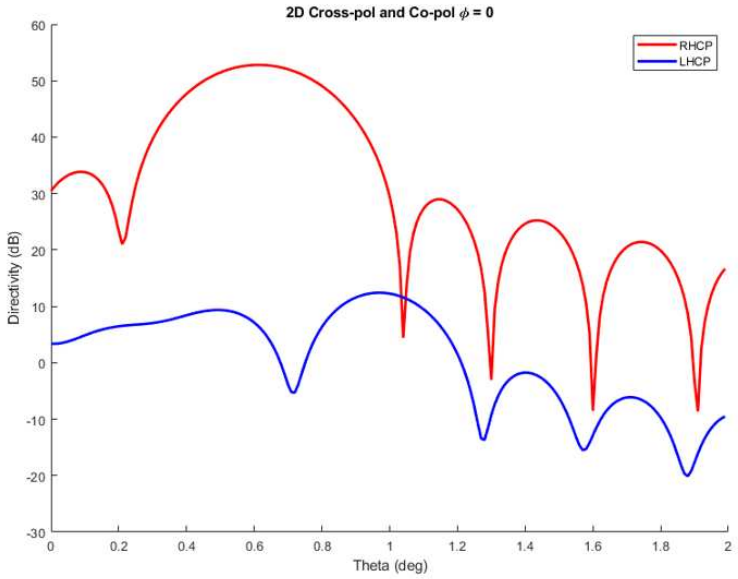

Figure 4.28: 2D cross-pol and co-pol radiation patterns for beam 19 (TX)

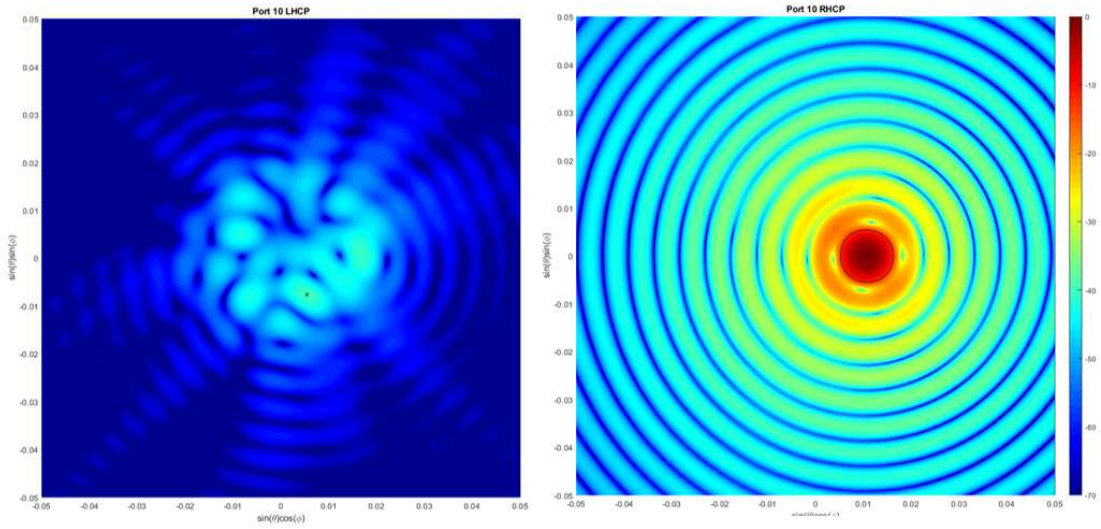

Figure 4.29: Cross-pol and co-pol radiation patterns for beam 19 (TX)

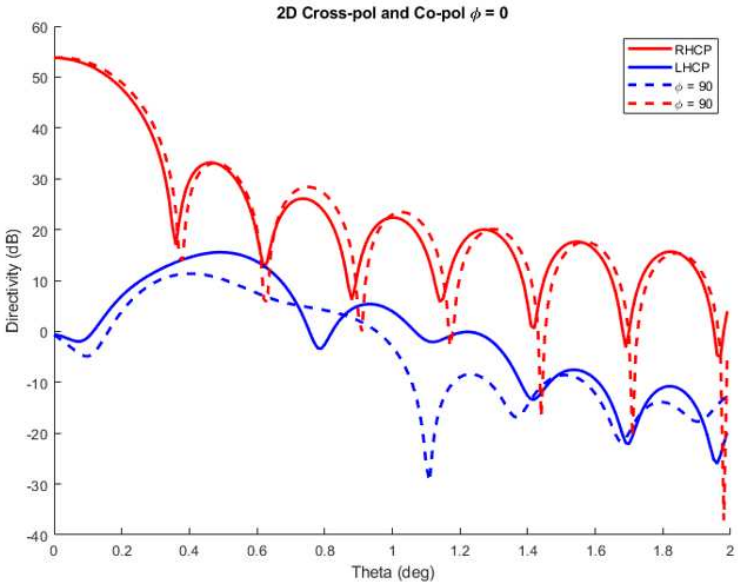

Figure 4.30: 2D cross-pol and co-pol radiation patterns for beam 1 (RX)

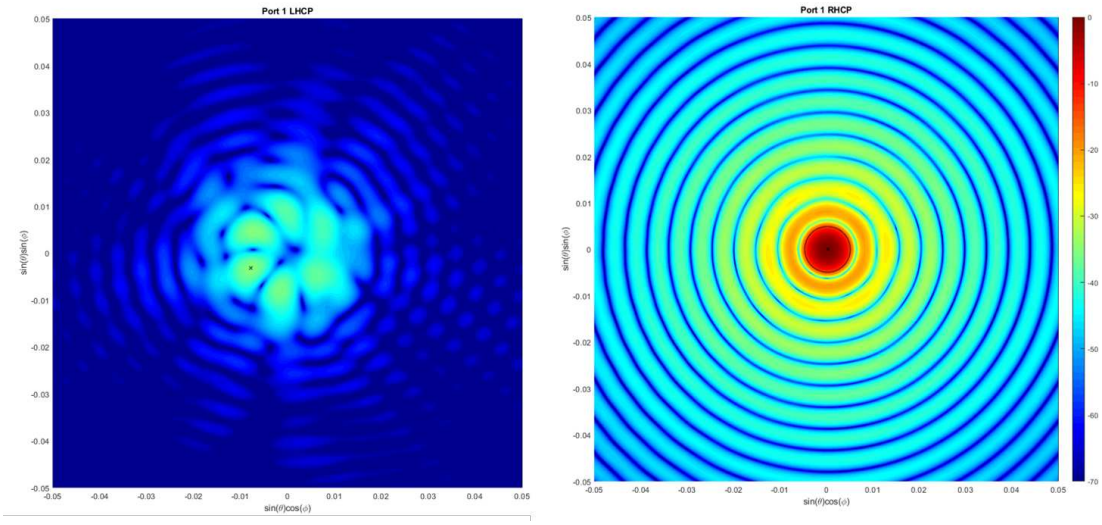

Figure 4.31: Cross-pol and co-pol radiation patterns for beam 1 (RX)

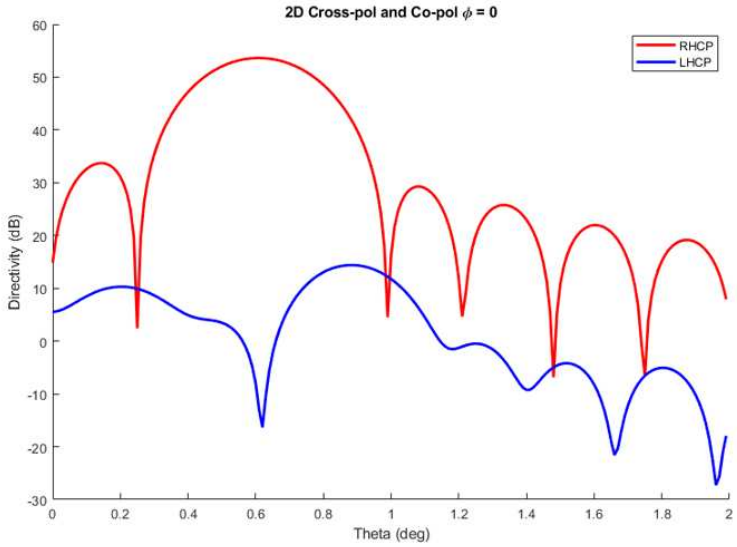

Figure 4.32: 2D cross-pol and co-pol radiation patterns for beam 10 (RX)

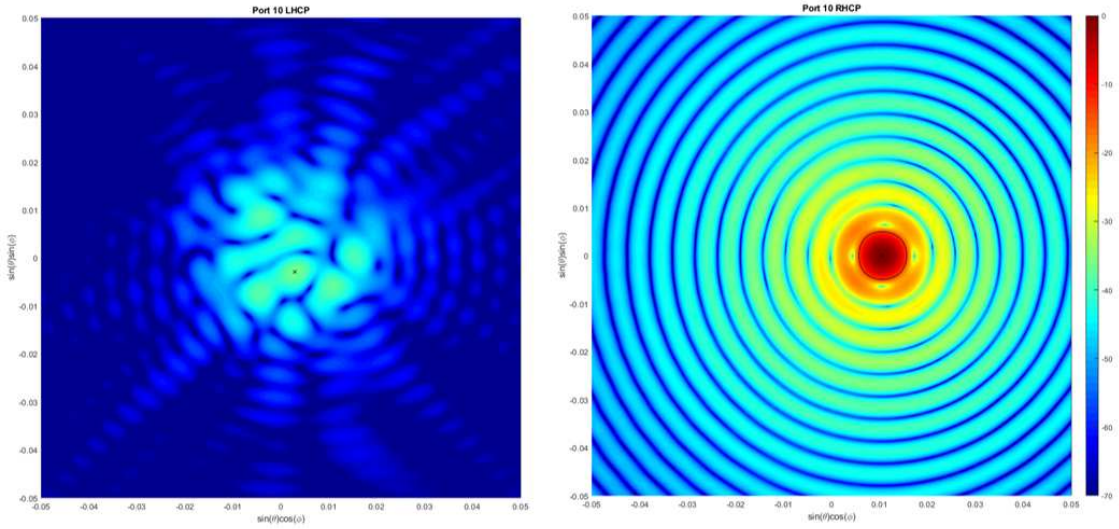

Figure 4.33: Cross-pol and co-pol radiation patterns for beam 10 (RX)

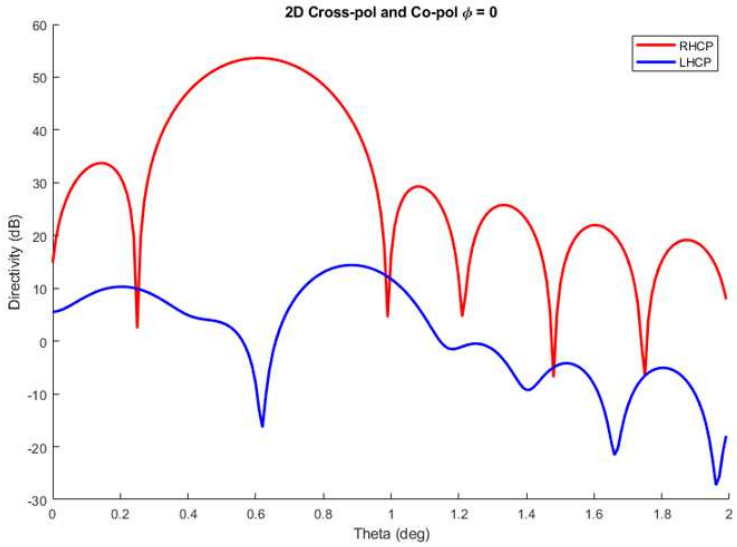

Figure 4.34: 2D cross-pol and co-pol radiation patterns for beam 19 (RX)

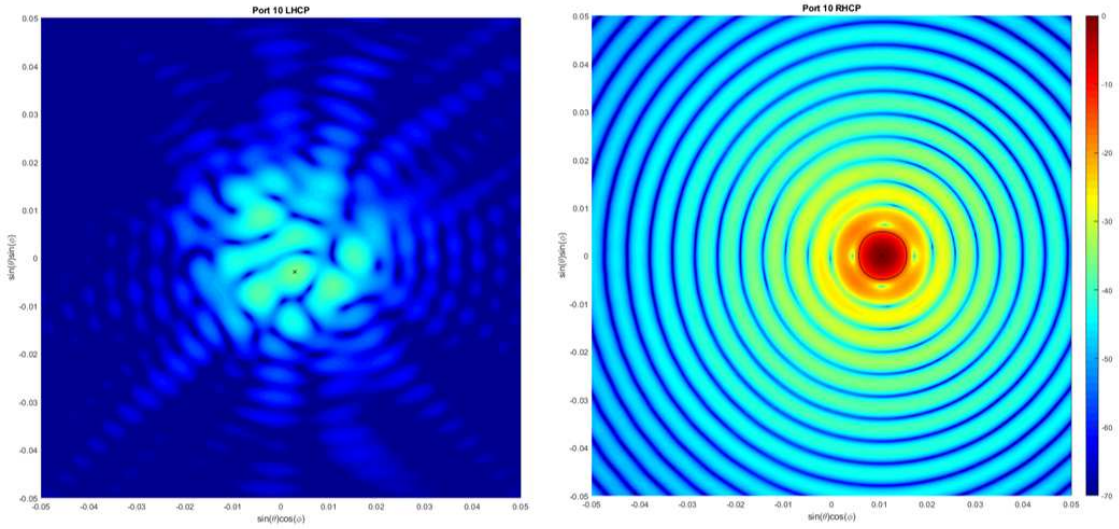

Figure 4.35: Cross-pol and co-pol radiation patterns for beam 19 (RX)

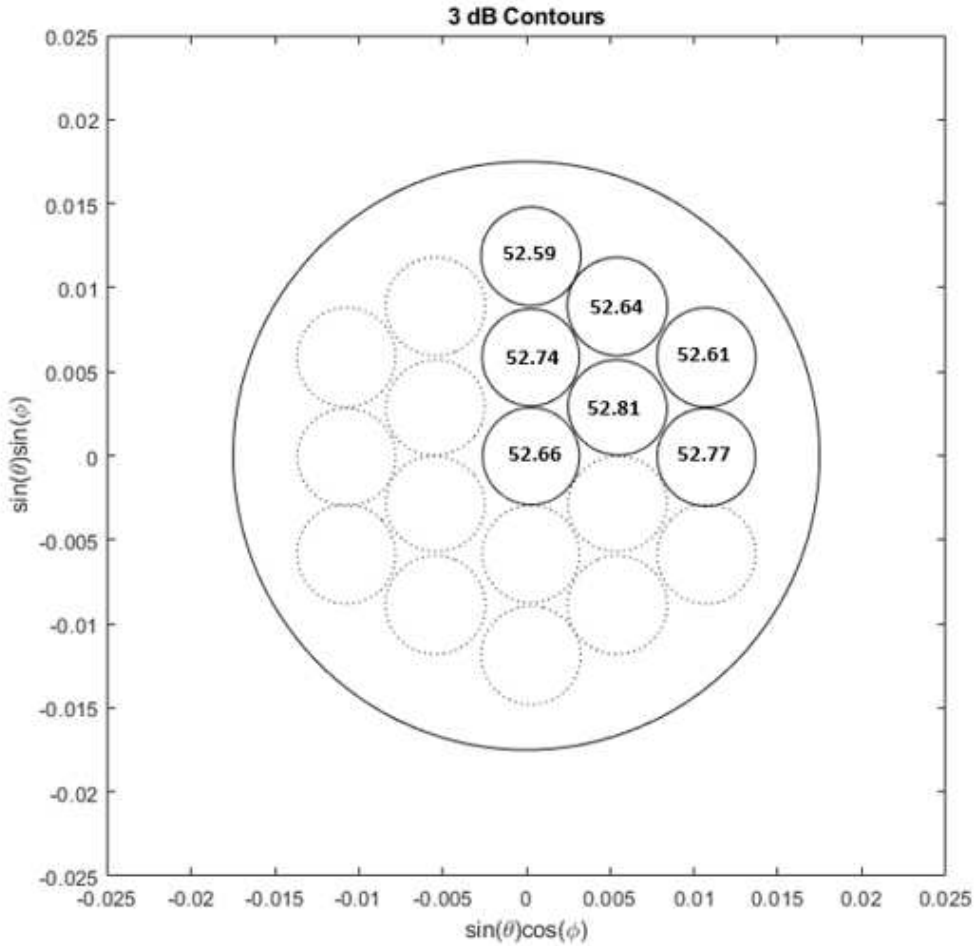

Figure 4.36: Simulated 3 dB contours of 7/19 beams excited using the TX waveguide feed horn simulated radiation patterns. The simulated directivity of the beams is noted in each beam at the center frequency, 73.5 GHz. The beam locations that were not directly simulated are derived through the symmetry of the feed horn.

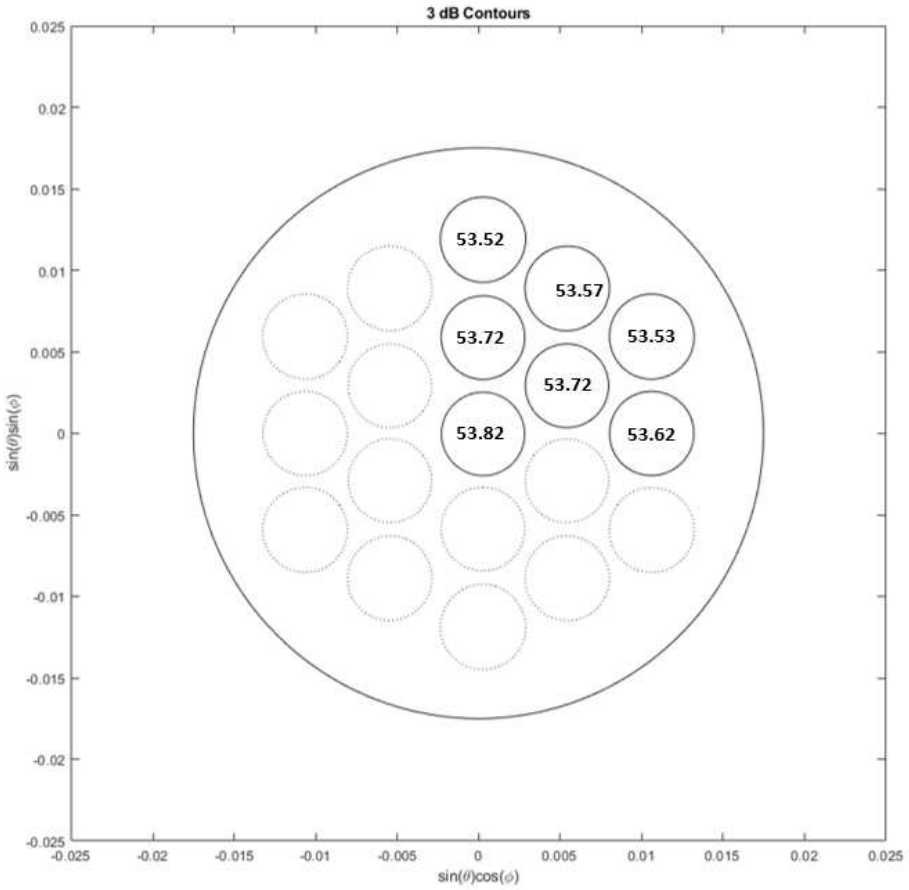

Figure 4.37: Simulated 3 dB contours of 7/19 beams excited using the RX waveguide feed horn simulated radiation patterns. The simulated directivity of the beams is noted in each beam at the center frequency, 83.5 GHz. The beam locations that were not directly simulated are derived through the symmetry of the feed horn.

4.2.6 Dish Illumination

The location of the feed horn and the surrounding structure are key attributes for the reflector system. Simulations are designed to ensure there is no blockage of the reflector dish from the mechanical structures necessary for the feed horn. The edge taper and spillover efficiency is also determined through simulation and analysis to increase the overall efficiency of the system.

A ray stimulus was utilized with the Asymptotic Solver in CST MWS to determine the range of incident angles that is not blocked by the hardware illuminating the antenna dish. The model used is shown in Figure 4.38, where you can see the teal colored rays emitting from the source placed at the focal point, and the darker blue lines are the first bounce from a surface. Two model blocks are placed to represent the feed horn and their mounting structure to estimate ray blockage from the feed housing structure. The design goal is no blockage in the field of view for an incident angle between -1 degree and 1 degree. The results in Figure 4.39 indicate there is no blockage for the range -2 degrees to 2 degrees. A shadow is not cast on the reflector dish from the feeds until the field of view is extended beyond 5 degrees, shown for example in Figure 4.40.

Uniform illumination of the reflector dish is paramount to maximizing the efficiency of this communication system. The feed positioning and pointing angle are adjusted while the results from a 2D plane E-field monitor reports the distribution of energy on the face of the reflector dish. The surface currents on the dish are also analyzed as an additional method to confirm that the maximum power is being directed from this parabolic dish. In Figure 4.41 the distribution of the farfield power plotted for different inclination angles of the feed horn. The result was gathered through simulation by monitoring the farfield on a defined plane in the field of view for the reflector dish. The design goal is to uniformly distribute the feed horn power across the plane face of the reflector, and the analysis indicates 47 degrees centers the energy appropriately.

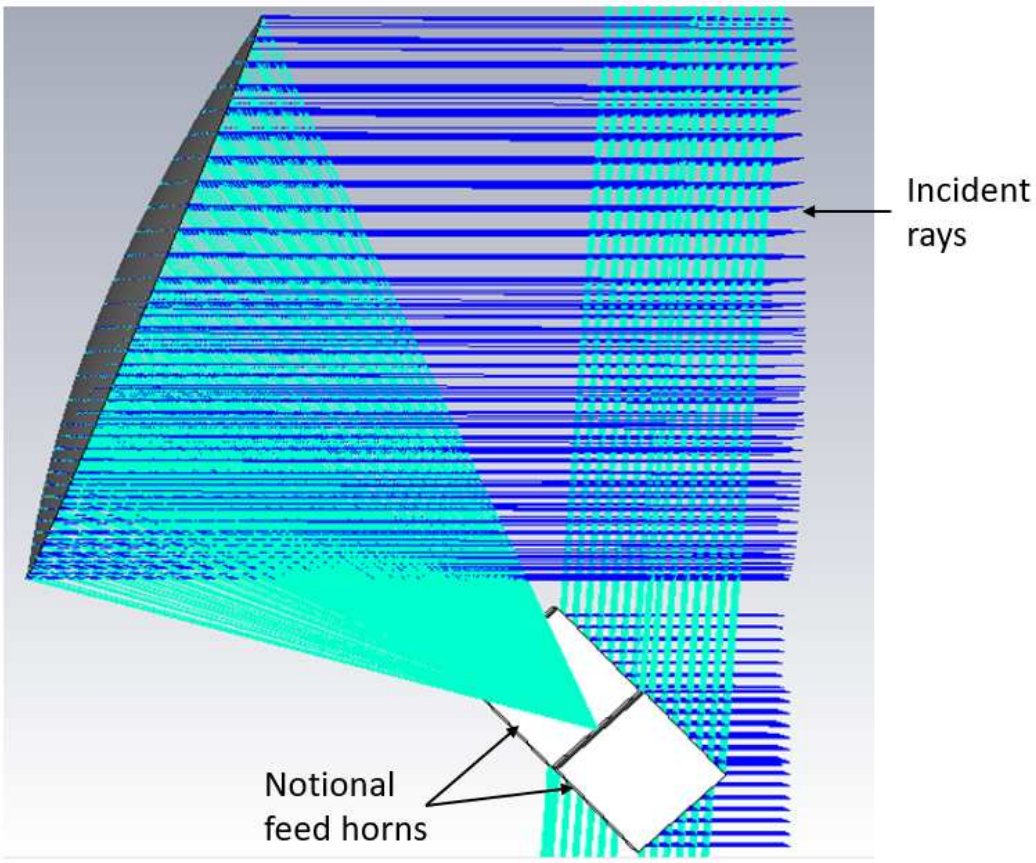

Figure 4.38: Rays are incident on the structure from the right of the figure, seen as the darker blue lines. Teal lines are the first reflection off of a surface for ray tracing purposes. There is feed blockage deflecting rays, but the dish has a full field of view and receives all of the incident rays in its area for this incidence angle. Incident angles are swept from -2 degrees to 2 degrees.

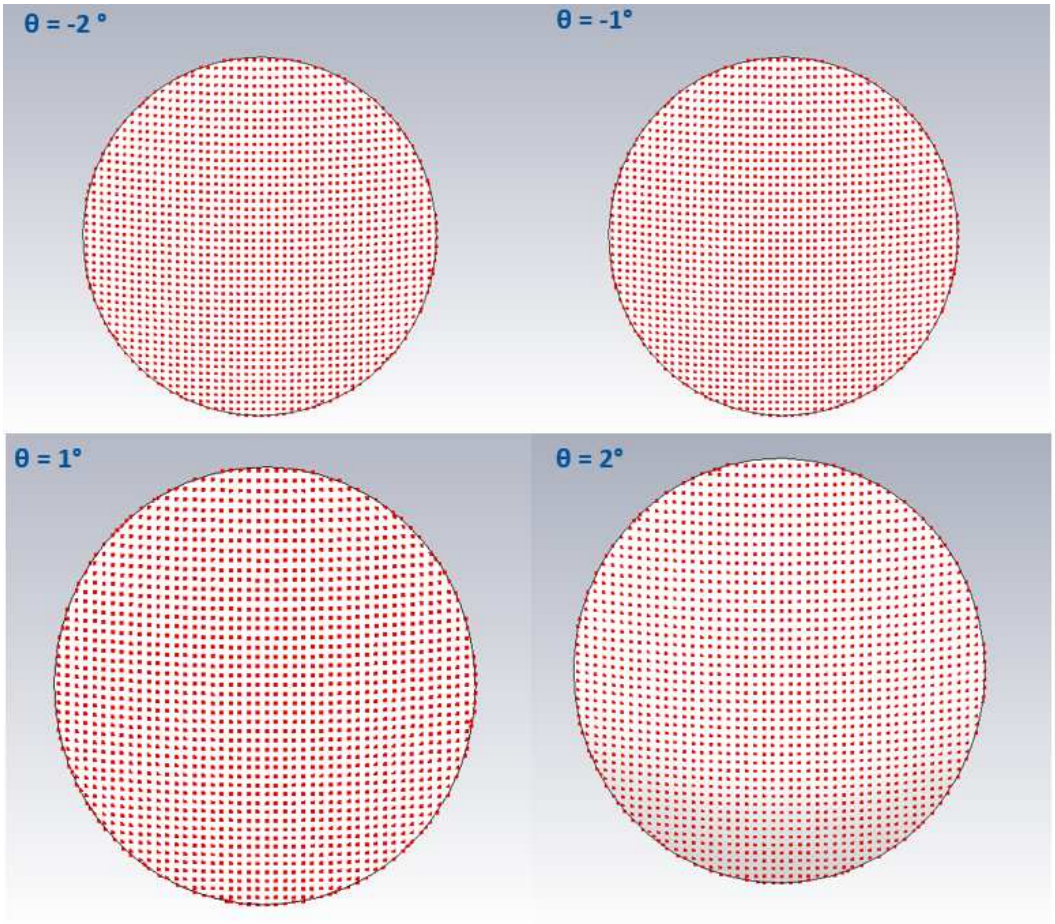

Figure 4.39: The results of the incident rays on the reflect from angles between -2 and 2 degrees. The red dots are rays that had their first impact on the surface of the dish. In all four cases for theta, there is no blockage from the feed structure.

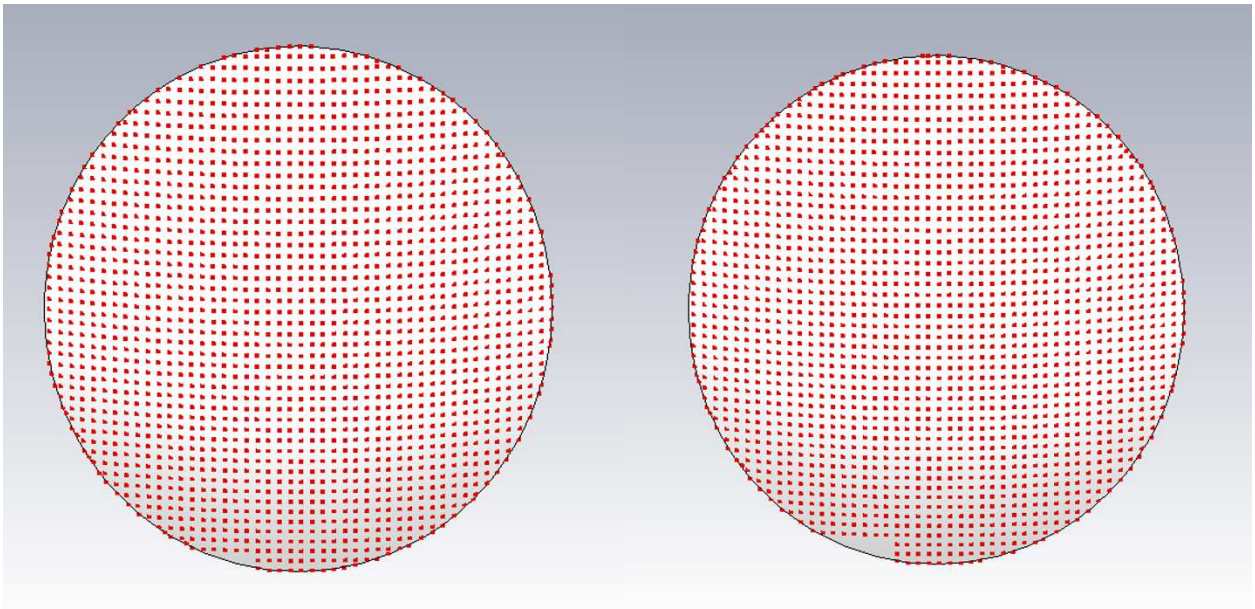

Figure 4.40: The left and right show the shadow cast on a field of view extended to 5 and 7 degrees. In the bottom left corner, the incident rays begin to be blocked rather than impacting the face of the dish. This is well outside the required field of view for this communication system.

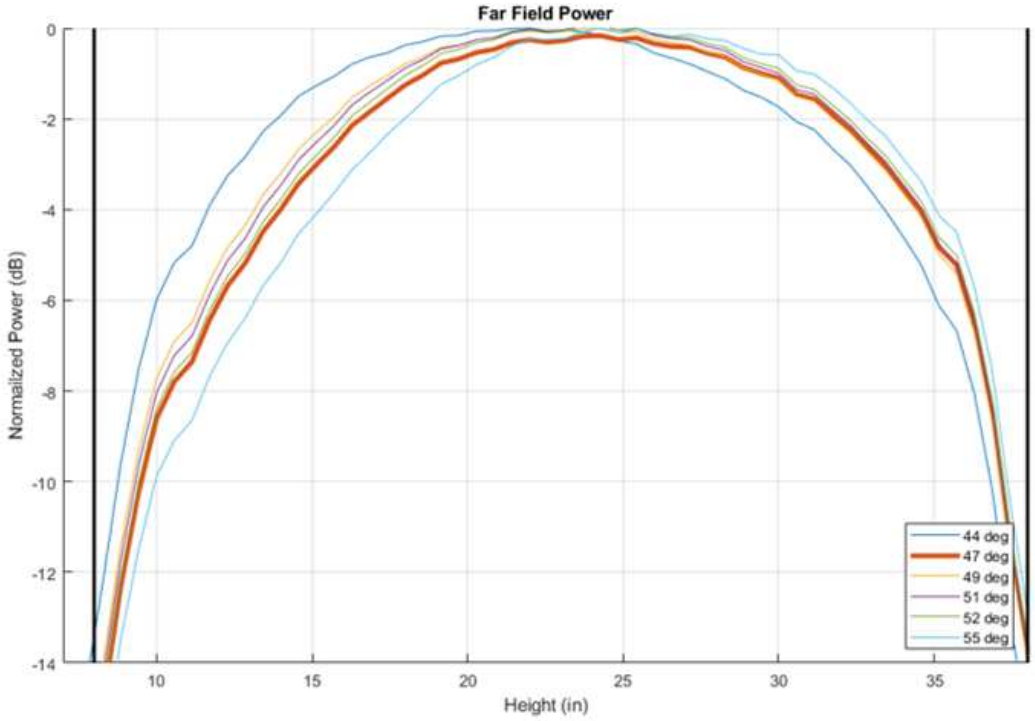

Figure 4.41: Normalized farfield pattern observed by a planar farfield monitor 20 cm from the reflector. This plot shows the spacial distribution of power in the farfield for several feed tilt angles to determine which angle provides an even illumination across the surface of the dish.

4.3 Waveguide prototypes

4.3.1 3D Printed Waveguide Coupons

Producing millimeter wave RF components is still an area of ongoing research and development, and the the availability of COTS components is still limited. 3D printing is a popular manufacturing method to realize these small channels and waveguide features in networks. The initial waveguide coupons were 3D printed to explore that as an option to build the V/W waveguide network prototype. The first step to determining the best path forward is to build the simple waveguide coupons that are straight forward to test with a network analyzer, and compare the measurements to simulated results. The coupons in Figure 4.42 each test an element of the network necessary to realize the waveguide feed horn. There are mitered bends in both E-plane and H-plane of a WR-12 waveguide section, a straight WR-12 section, and a 4-port septum polarizer coupon.

The waveguide coupons were measured with a network analyzer to validate the 3D printing fabrication process. The 3D printed waveguide did not perform as well as expected, and noticeable issues were discovered mechanically inspecting the units. The channels were not able to maintain their size and integrity with features such as bends, or the septum polarizer walls. A decision was made to abandon the 3D printing approach to realize the WR-10 to WR-15 sized channels, and instead the channels would be milled into aluminum and copper blocks for the next round of coupons.

4.3.2 Milled Waveguide Coupons

The same iteration of waveguide coupons were constructed for another round of development towards the waveguide feed horn. Figure 4.43 shows the same waveguide coupons to represent the transitions required for the full feed assembly. The E-bend, H-bend, a straight section, and another 4-port septum polarizer coupon were built as proof of concept coupons. The mechanical inspections of the milled waveguides indicated they were built to specifications. The coupons were then electrically tested by measuring their S-parameters, and the results are shown in the following figures, 4.46 - 4.50.

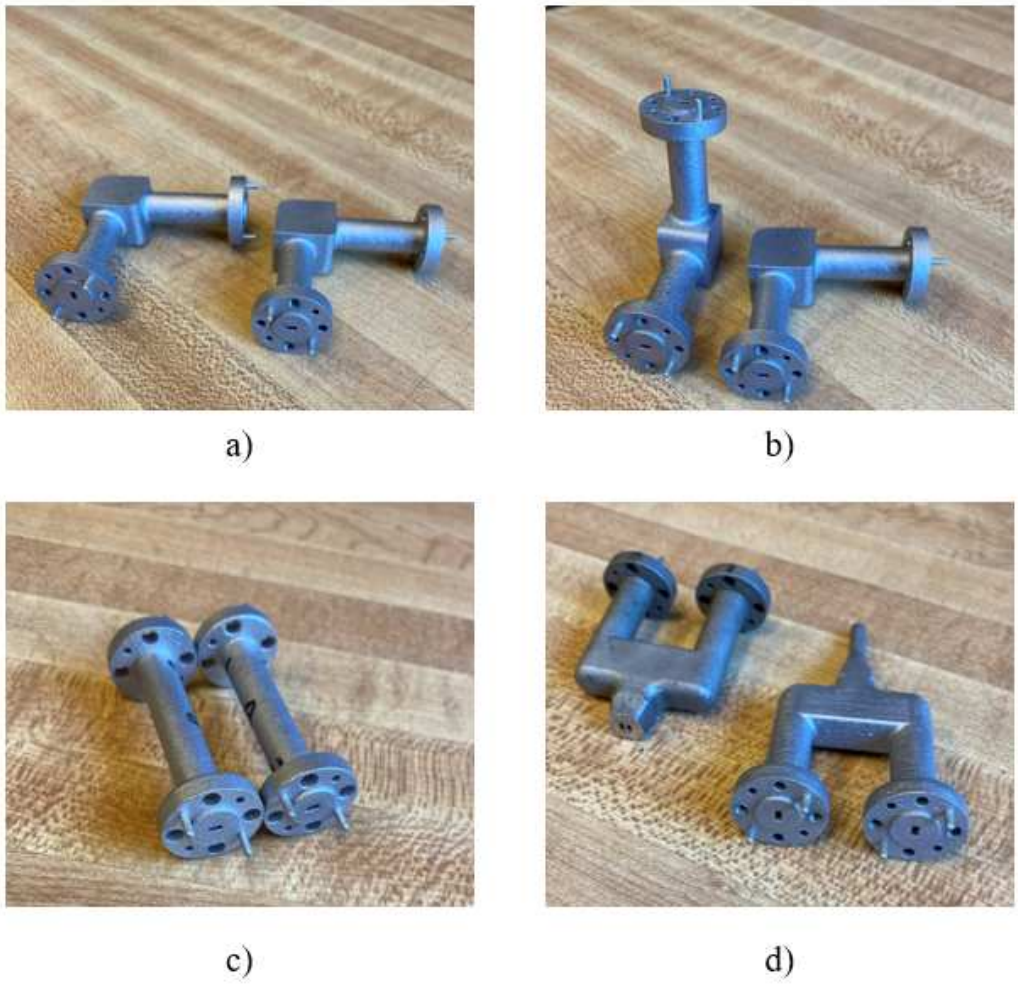

Figure 4.42: a) E and H-bend b) E and H-bend c) Straight WR-12 waveguide d) WR-12 septum polarizer coupon (sectioned)

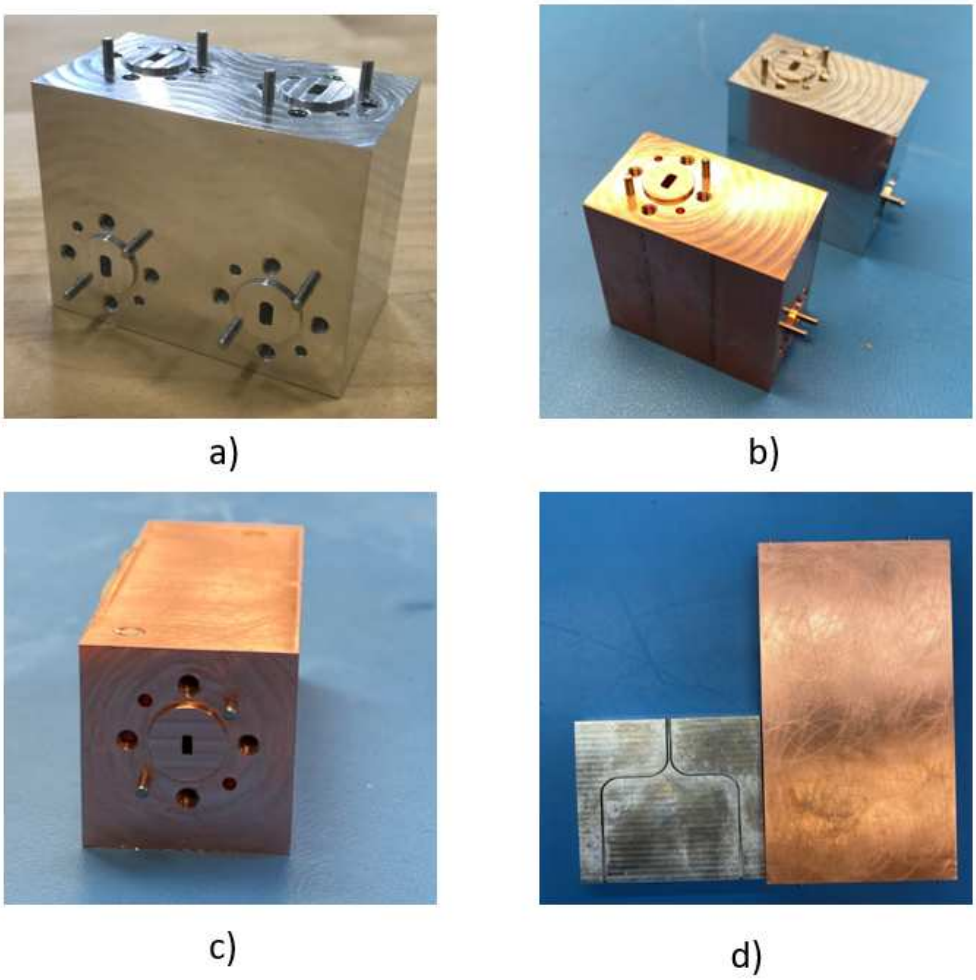

Figure 4.43: a) H-bend WR-12 waveguide b) E-bend WR-12 waveguide c) Straight WR-10 waveguide d) WR-12 to modified WR-10 transition and septum polarizer

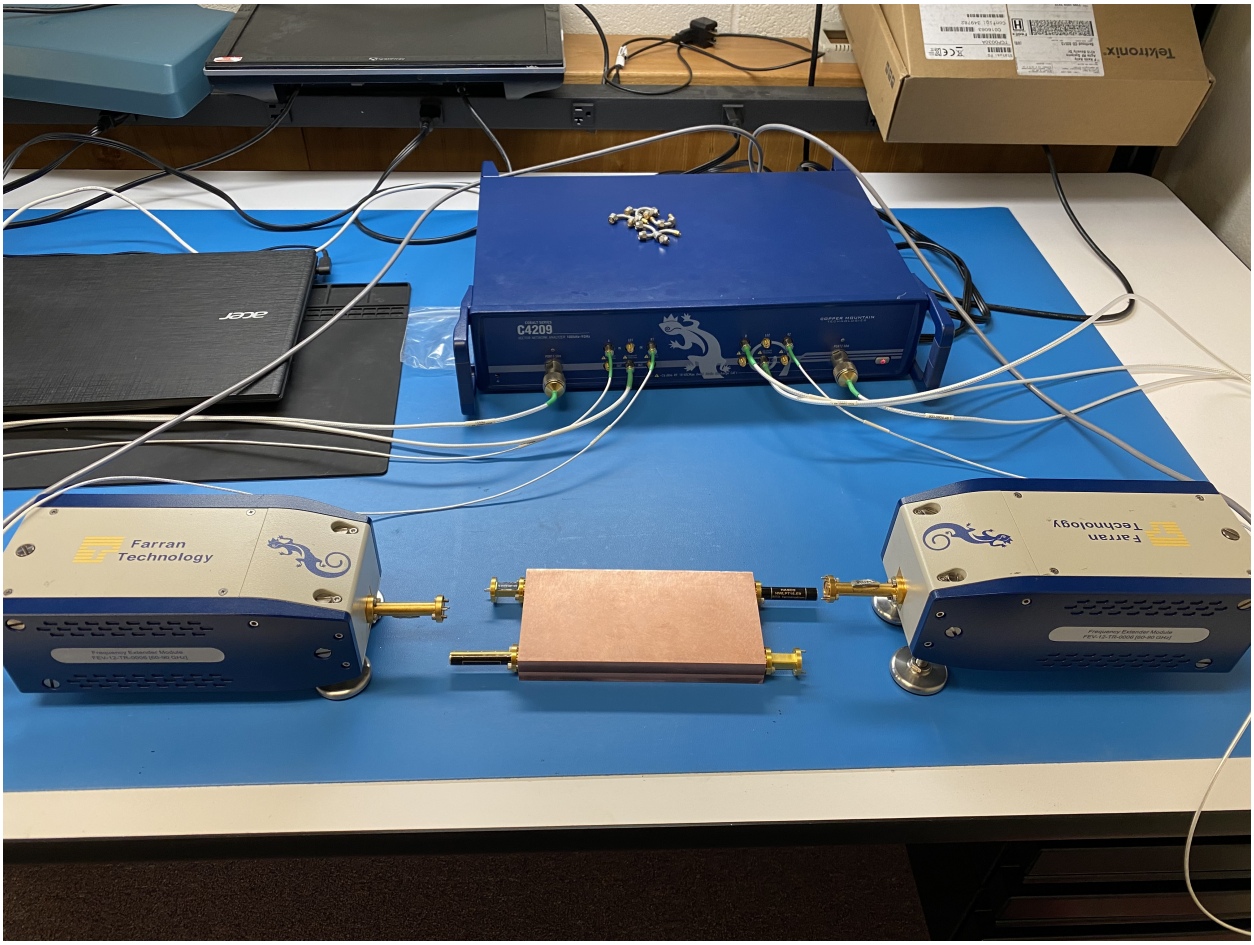

Figure 4.44: The septum polarizer coupon was tested using frequency extenders to make S-parameter measurements from 60 - 90 GHz. The 4-port septum polarizer coupon is pictured with the isolated and coupled ports loaded by a 50 Ohm load. The input and thru ports have WR-12 to WR-15 waveguide adapters to interface with the network analyzer.

The benchtop tests were carried out using a Copper Mountain C4209 2-Port 9 GHz Analyzer, in conjunction with the CobaltFx FEV-12 Frequency Extension System, which extends the testing range to 60-90 GHz and features WR-12 waveguide interfaces. The benchtop test setup for the 4-port septum polarizer coupon measurement is shown in Figure 4.44. Similar setups were used for all waveguide coupons.

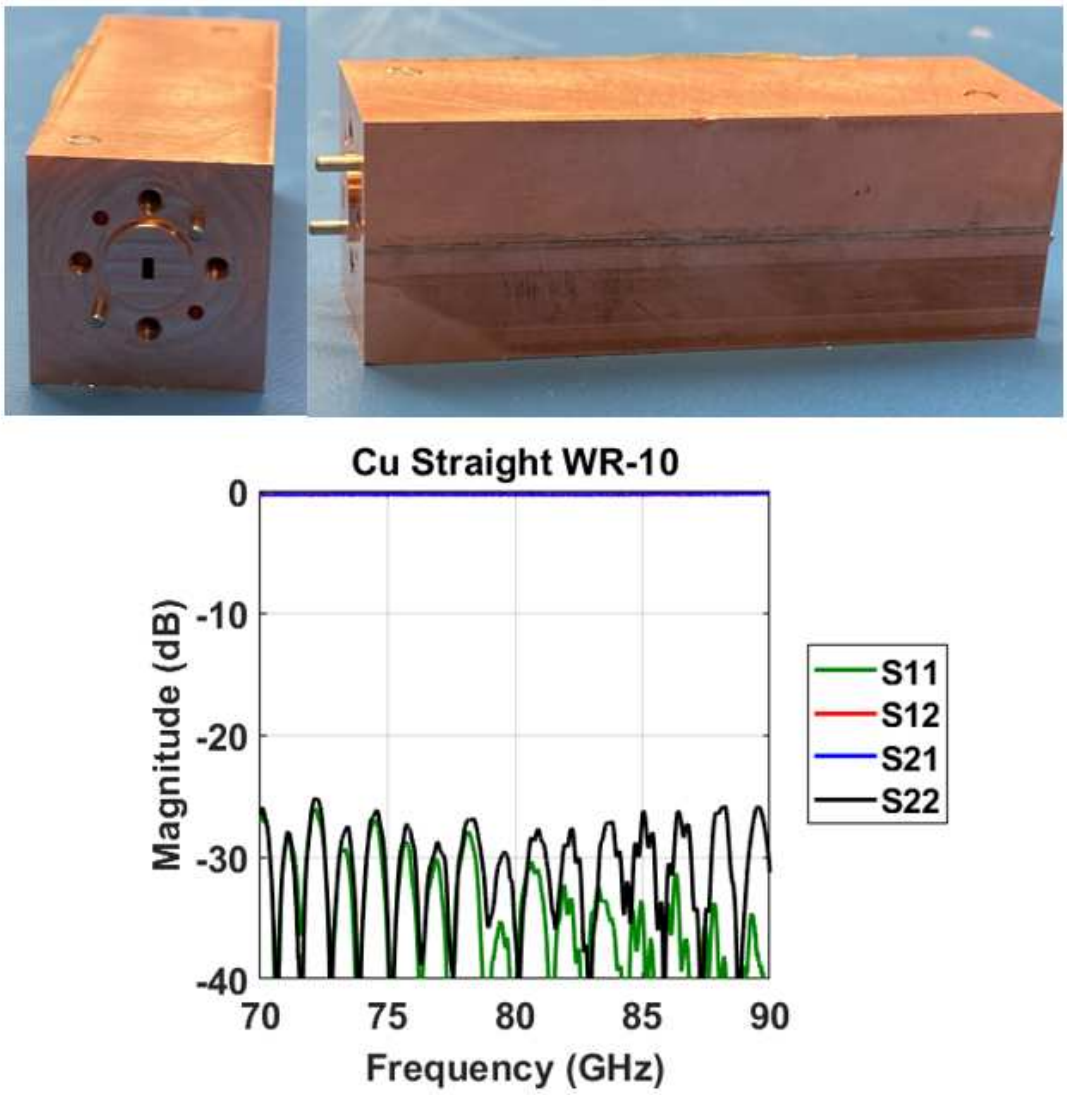

Figure 4.45: Bench test for copper straight WR-10 coupon across V and W-band

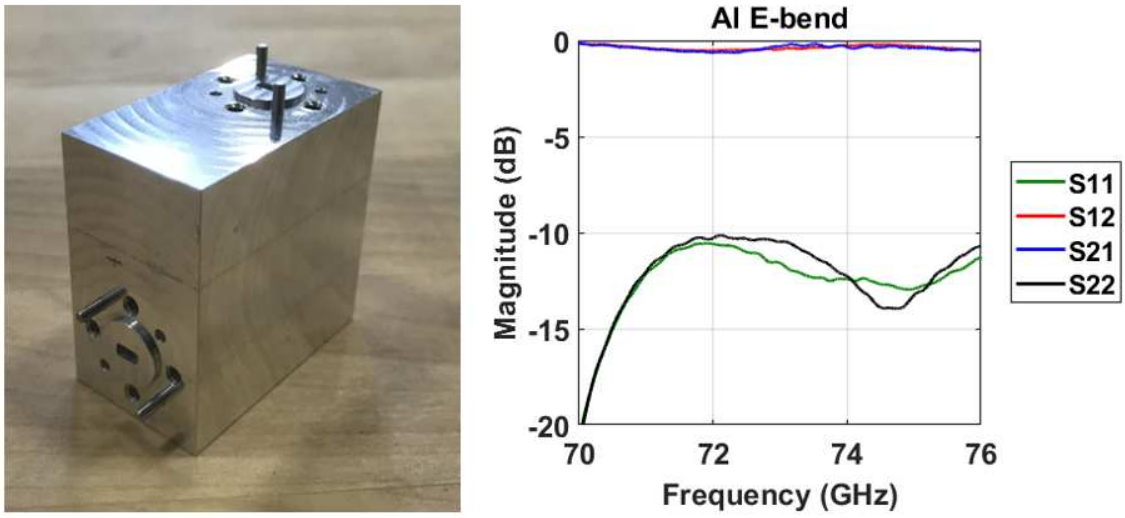

Figure 4.46: Bench test results for aluminum E-bend waveguide coupon.

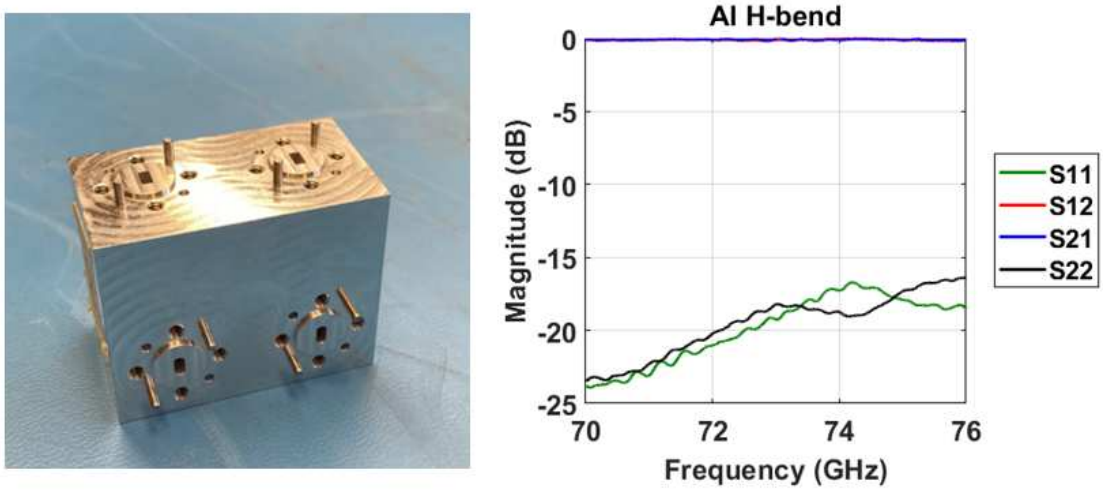

Figure 4.47: Bench test results for the operational aluminum H-bend waveguide coupon.

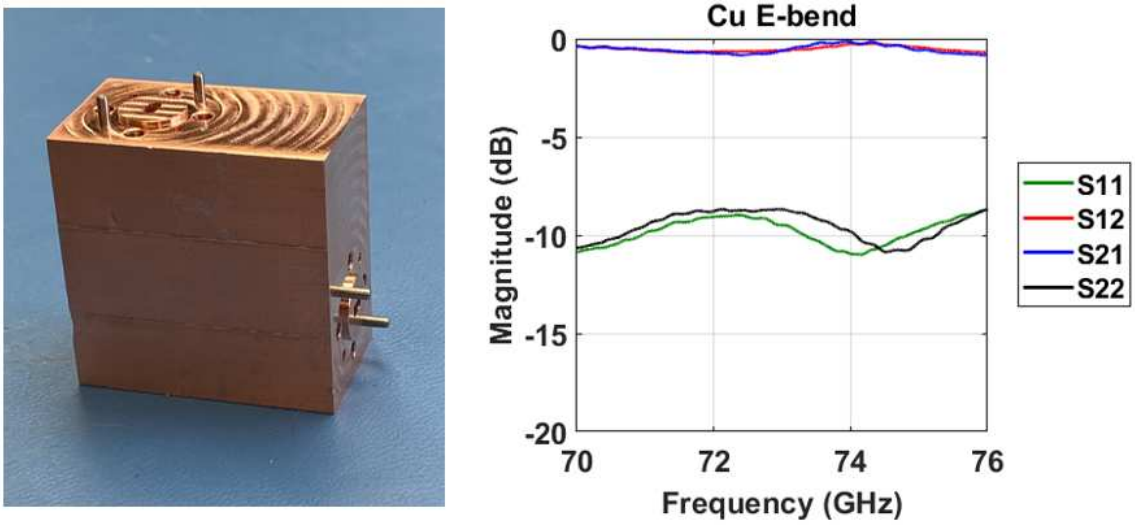

Figure 4.48: Bench test results for the copper E-bend waveguide coupon

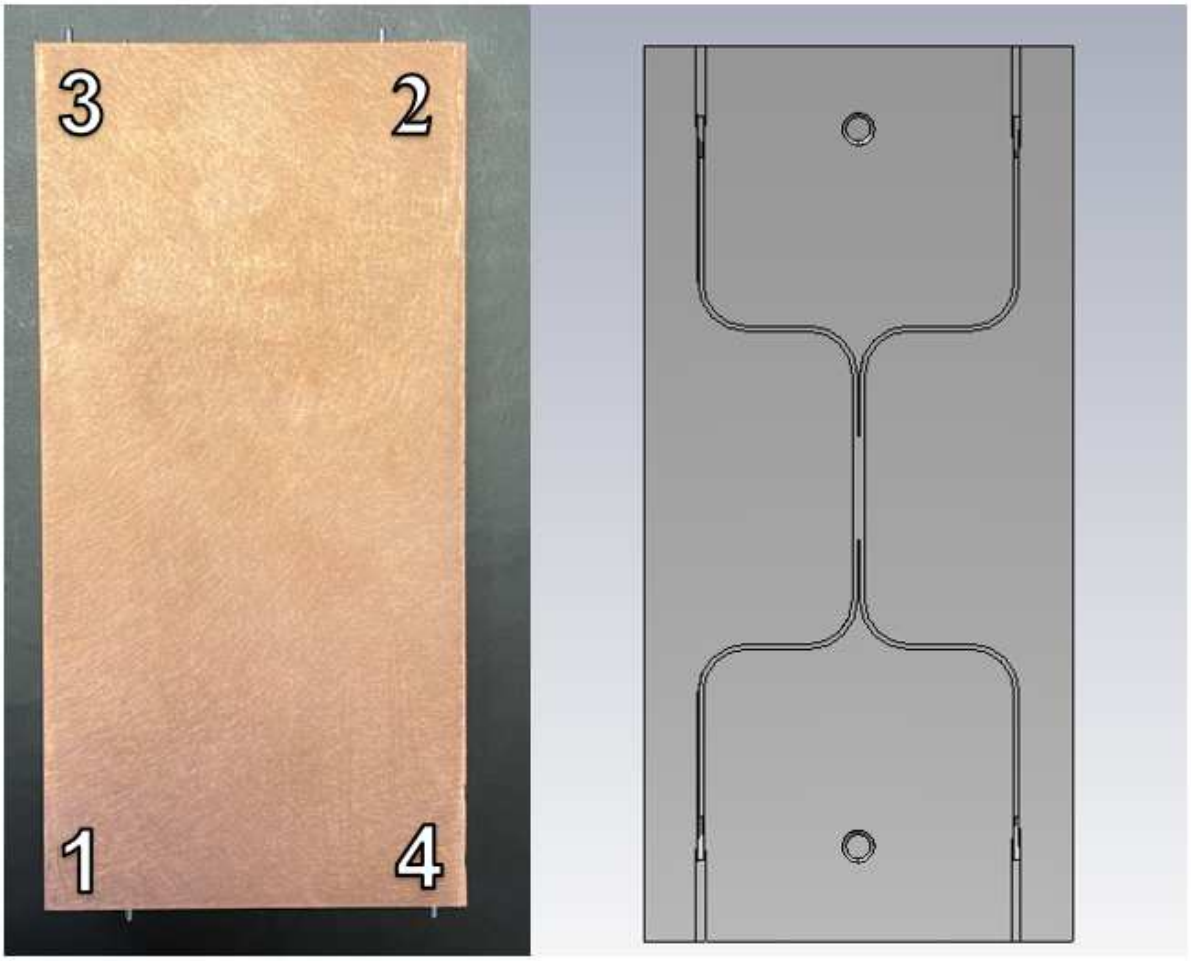

Figure 4.49: The image on the left is the copper block housing the waveguide channels to prove the manufacture method for the septum polarizer, based on the CST MWS model on the right which shows the inner channel layer. There are two septum polarizers back-to-back separated by greater than two wavelengths. The square section has the two orthogonal waveguide modes present, and the second septum polarizer in the chain combines the modes back into the single dominant mode to be propagated along the thru channel. The test setup defines the two input ports as Port 1 (labeled 1) and Port 2 (labeled 4), which are side by side. The thru measurements are related as 1 to 2, and 4 to 3.

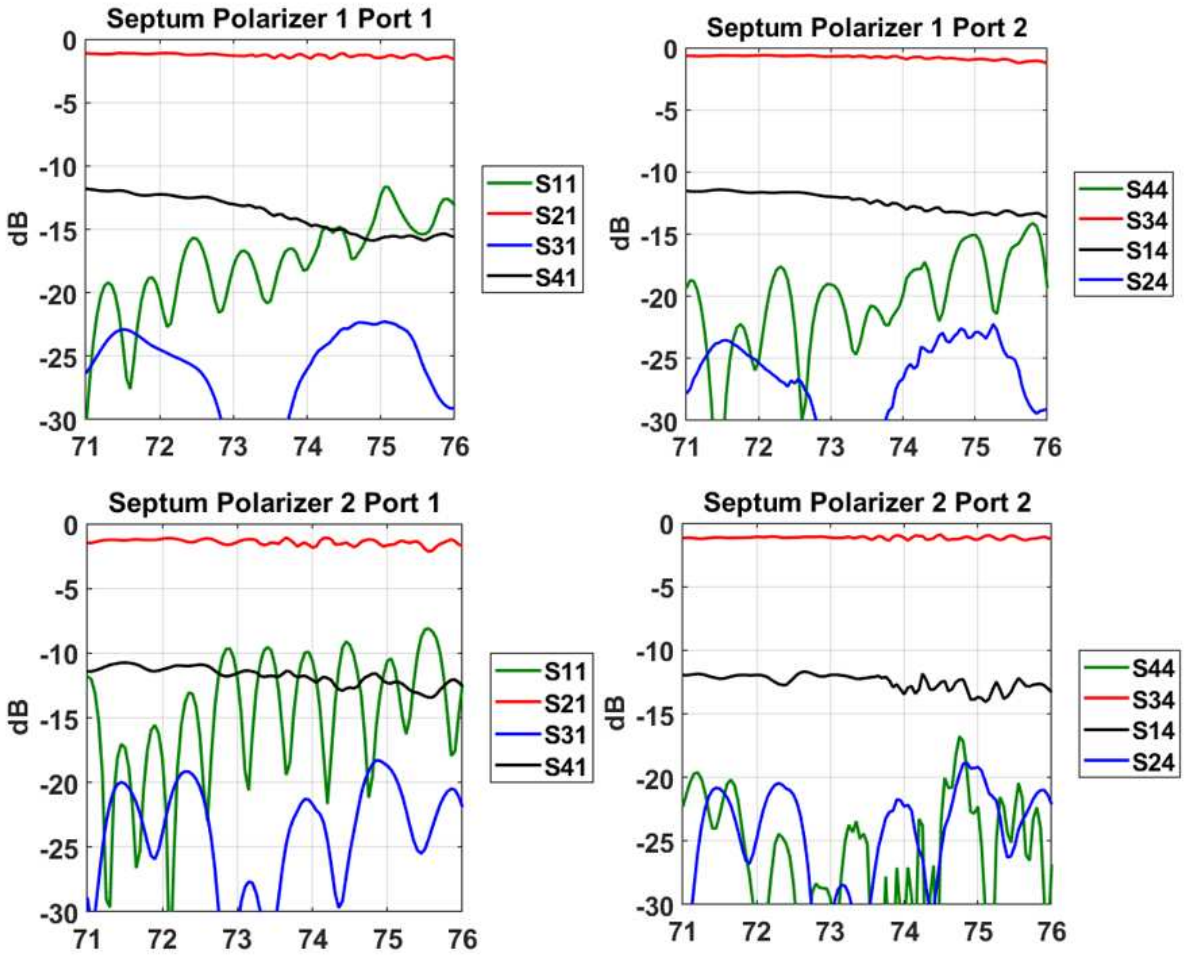

Figure 4.50: Septum Polarizer results. The septum polarizer inputs 1 and 2 are labeled as ports 1 and 4. When measuring from input 1, port 1 is the input, port 3 is the thru port, port 2 is the coupled port, and port 4 is the isolated port. When measuring from input 2, port 4 is the input, port 2 is the thru port, port 3 is the coupled port, and port 1 is the isolated port.

The measured results for all waveguide coupons match simulated results well. The reflection and thru parameters for each waveguide section indicate the bends and channels were all manufactured to the required specification to maintain a good signal through the waveguide sections. The septum polarizer coupons also performed as expected based on simulation. The two separate coupons, each with back-to-back septum polarizers, increase the confidence that a stepped septum polarizer is reliably manufacturable. Based on the successful coupon fabrication and tests, the waveguide feed assembly is next to be manufactured. The only pieces that have not been tested at this point are the square-to-circle transition, and the straight circular waveguide sections. No devices were available to measure cylindrical waveguide pieces at V/W-band, so these transitions did not have coupons built. Given that the transitions are straight forward for manufacture, these were considered low-risk for the system build.

4.4 Waveguide Feed Horn

This section discusses measuring the first complete component to be fabricated for the V/W-band system, the waveguide feed assembly. The purpose of these measurements are to provide a baseline for what can be expected when taking pattern measurements using the tools available. A back-to-back horn measurement serve as a fit-check for the necessary equipment, and indicates that the waveguide channels are functional. A WR-12 open-ended waveguide probe was used to measure V and H amplitude and phase of the waveguide feed horns.

4.4.1 Benchtop Feed Horn Verification

The next steps following the successful fabrication and test of the waveguide coupons are to bring the components together into the full system, and then perform bench top and over-the-air measurements to validate channel integrity. A total of four waveguide horns were built, two for each communication band. A completed waveguide is presented in Figure 4.51. The 19 beams are seen at the top of the cylindrical extrusion. The eight holes surrounding are mounting holes to attach the feed block to the housing structure in the reflector system. Figure 4.52 shows the assembly mounted into the structure on the base plate, as well as the reflector laser alignment system.

The frequency converter modules are required to perform electrical tests on the waveguide feed horns, given the interface is a non-standard WR-12 port designed to specifically fit these modules. The converter modules perform the conversion based on the LO source, taking 6x the LO source for the mixing up from IF or down to IF, for the transmitting and receiving packages, respectively. The IF is 1 GHz in all cases. These modules also include amplifier stages and require a DC power supply.

The first verification of the waveguide feed horns was a horn-to-horn bench top test to simplify verify that a signal is being transmitted over there air, and that there are no problems in the waveguide channels. Figure 4.53 and Figure 4.54 show the test setup and results of an initial test. The tests here verified that all four waveguide horns were transmitting and receiving as expected across

Figure 4.51: One machined waveguide feed horn block. These blocks are constructed with one inch sides to interface with the frequency converter modules. The blocks are 2.61" wide at their longest point, and 3.88" in height from their base to the top of the cylindrical extrusion.

the frequency bands, and the test equipment required to perform these measurements was working as intended.

Figure 4.52: One machined waveguide feed horn block. These blocks are constructed with one inch sides to interface with the frequency converter modules. The blocks are 2.61" wide at their longest point, and 3.88" in height from their base to the cylindrical extrusion. In this image the waveguide horn is mounted and the laser alignment system is attached to the feed horn housing structure. The laser alignment system reflects lasers off of the reflector and intersects at the focal point of the dish, where the feed horn is located.

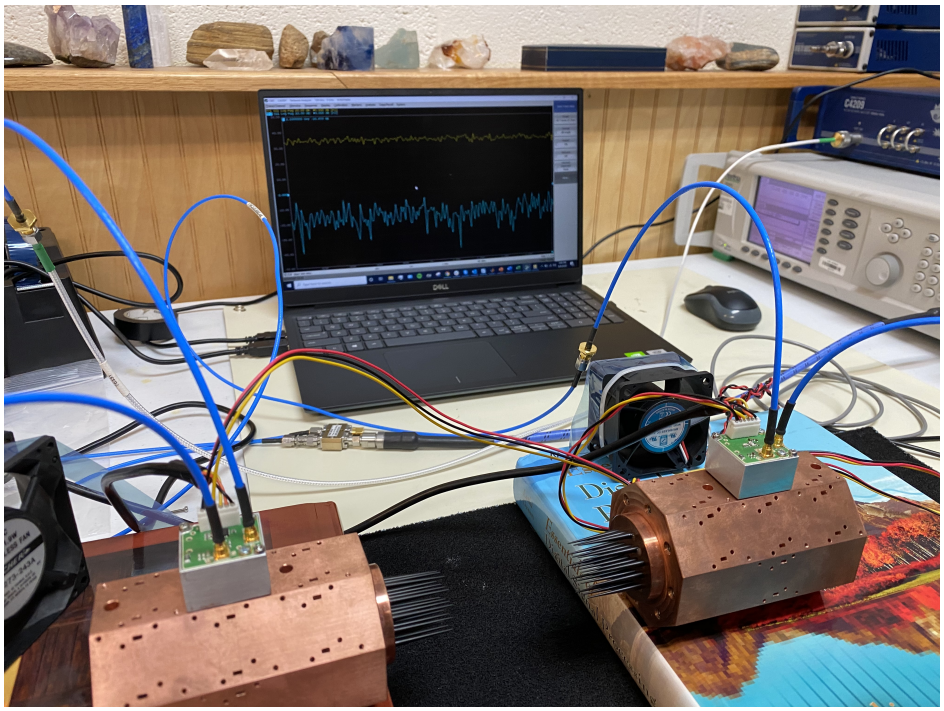

Figure 4.53: Horn-to-horn bench top test verifying signal transmission over-the-air. The relevant S-parameter results are shown in the next figure, 4.54.

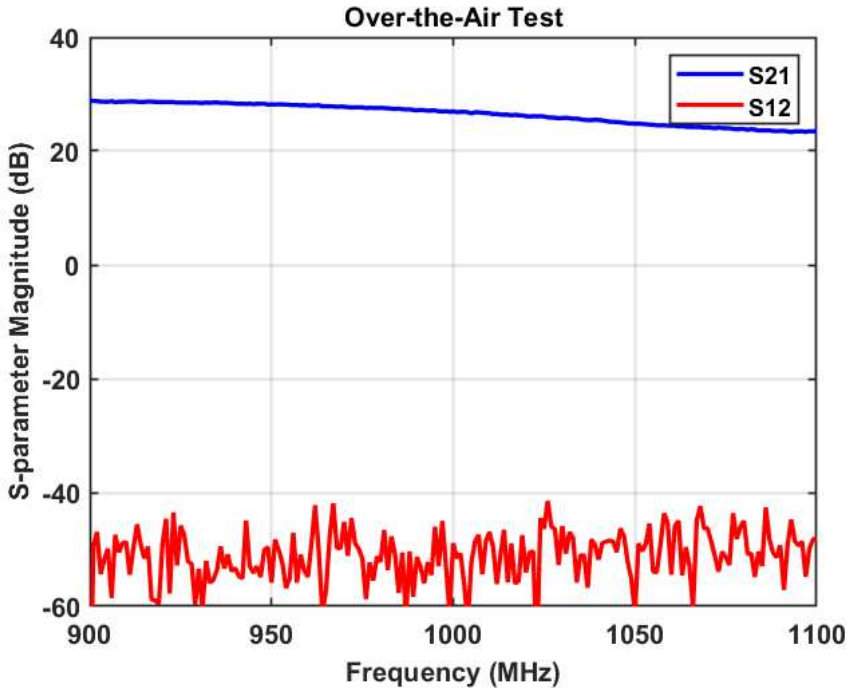

Figure 4.54: S-parameter result of the horn-to-horn over-the-air bench top test. S21 is the direction of transmission, and the opposite S12 shows the noise in the system. The expected magnitude of S21 indicates a clear transmission between the modules.

4.4.2 Septum Polarizer Measurements

Over-the-air measurements were done to evaluate the septum polarizers, and to examine the reprehensibility of the small components. The waveguide feed assembly was positioned so that the open ended waveguide probe was in the far field, and the probe was rotated 90 degrees to measure the V and H components of the circularly polarized wave generated by the waveguide feed horn. The balance in both phase and amplitude indicate the effectiveness of the beam forming septum polarizer. Measuring a total of 38 septum polarizers gives a large enough sample size to gather insight into how susceptible the beam forming features are to tolerance, and how reproducible they are. The relative measured results are shown in Figure 4.55 and Figure 4.56.

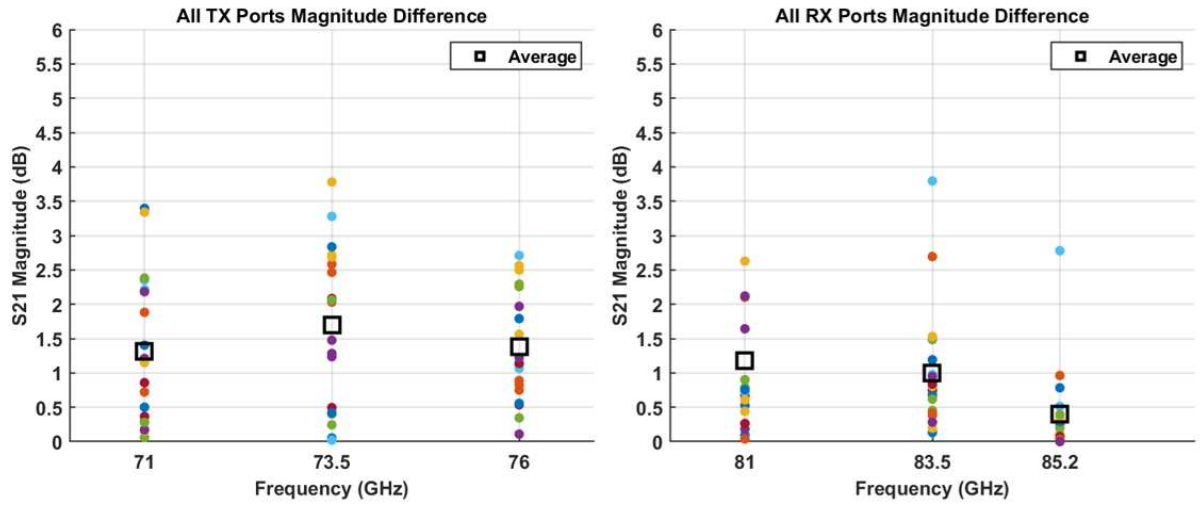

Figure 4.55: The open ended waveguide probe was used to measure the magnitude of the V and H components from the feed assembly at each port. The relative magnitude between polarizations is plotted here, with the average of all 19 ports marked.

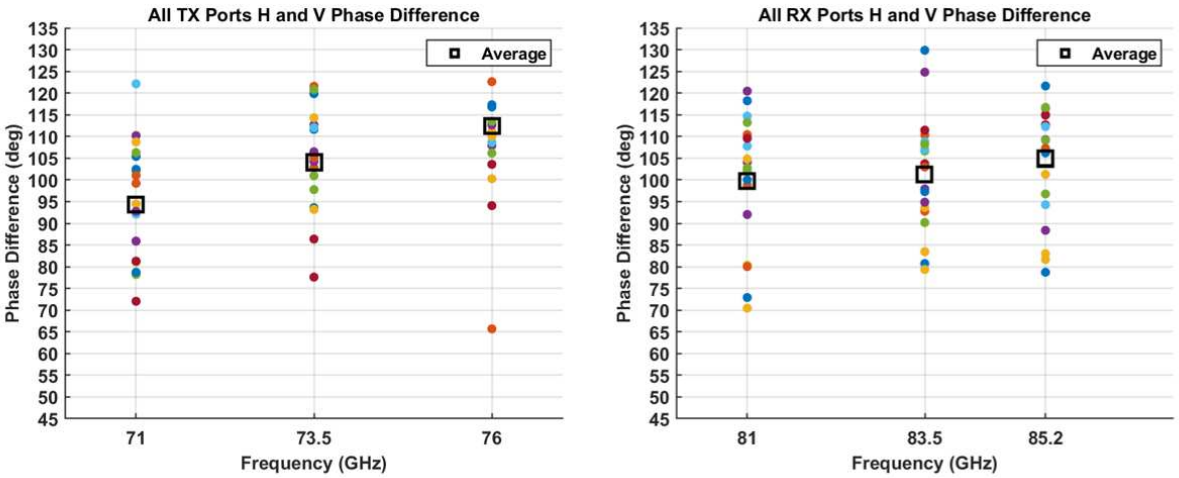

Figure 4.56: The open ended waveguide probe was used to measure the phase of the V and H components from the feed assembly at each port. The relative phase between polarizations is plotted here, with the average of all 19 ports marked.

Chapter 5

V/W Satcom System Evaluation

5.1 System Evaluation

The V/W-band Satcom system was characterized by evaluating the feed assemblies as individual systems, and then they were integrated into the full antenna system for full-scale measurements. A near field antenna range was used to measure the antenna radiation patterns and gain for the feeds and the reflector. The range was also used to measure the characteristics of the septum polarizers in each individual waveguide channel. The first measurements performed at the range consisted of one of each feed assemblies as individual antenna systems. Once the measurement process was fully validated, the full antenna system was assembled and measured at the near field range. Each septum polarizer was evaluated at the near field antenna range as well, by measuring the V-pol and H-pol amplitude and phase at each port, to examine the consistency between septum polarizers in all channels.

The first measurement of the feeds was also useful as a straight forward initial test run of the frequency conversion systems, and the data processing required to interpret the results gathered by the near field range. The small feed horns made alignment and test set up less complicated than the full system reflector measurements, and it took less time before measurements could be verified. The antenna range only recorded measurements for a single frequency, the 1 GHz IF utilized by the frequency converter modules. The external frequency conversion is a necessary piece of the antenna system, and it was also necessary due to the limited frequency range of the near field antenna range, so it was essential to verify this system component. The transformation from linearly polarized near field measurements, to far field circularly polarized results, was also a key feature of this measurement that had to be understood to evaluate this antenna system. To conclude this experiment, the simulated and measured beam patterns and directivity were compared for the feed assemblies and reflector system, and they are shown at the end of this chapter.

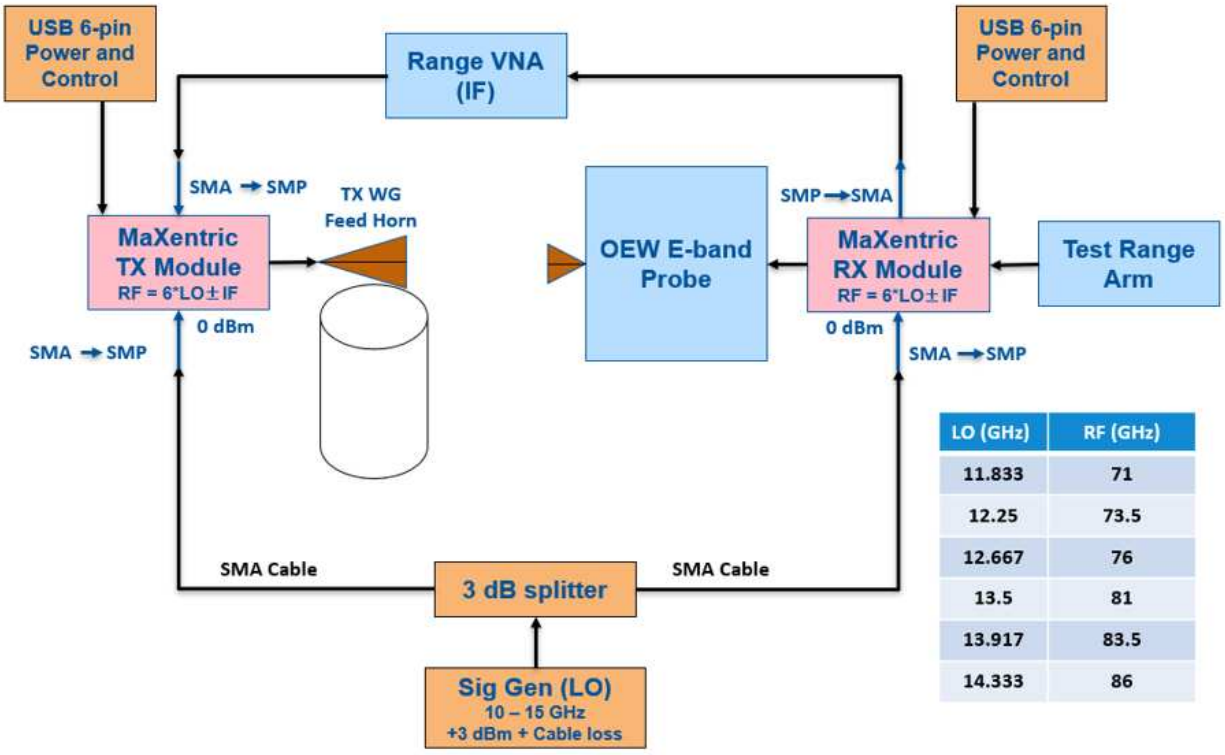

LO (GHz)	RF (GHz)
11.833	71
12.25	73.5
12.667	76
13.5	81
13.917	83.5
14.333	86

Figure 5.1: The test plan for the antenna range measurement of a feed horn assembly. The feed horn assembly under test interfaces with the frequency converter modules, which are fed DC power, and mix the IF from the range equipment with an external LO source to drive the RF. The WR-12 open ended waveguide probe interfaces with another frequency convert modules, and scans the aperture of the antenna under test. The same process was followed to test the fully integrated antenna system.

The test plan, shown in Figure 5.1, lays out the set up that was used to support measurements of the waveguide feed assemblies and the full antenna system. The active up and down converter modules require an LO source and a DC power source to perform frequency conversions and signal amplification. The antenna range only measures at the IF of 1 GHz for all RF configurations, due to the mixing scheme. The antenna range used an open-ended waveguide probe to measure the electric field in a sufficient area within the near field of each antenna aperture, with the area sampled in half-wavelength increments to satisfy the Nyquist criteria in the near field to far field transformation calculations. The antenna dish measurements was completed utilizing the same methods and procedures.

5.2 Waveguide Feed Horn Measurements

The transmit-band and receive-band waveguide feed horns were measured at the center port as a straight-forward test run of the measurement setup. The primary goals for this preliminary test was to validate the frequency converter modules, to ensure that they interfaced with the range measurement equipment as expected, and to measure the feed assembly patterns to compare with simulated patterns. The pattern measurements for a single frequency were captured in a 6-by-6 inch square in the plane of the waveguide probe. The feed measurements took nearly 20 minutes with a step size of $\lambda/2$ at the transmit and receive frequencies. The area captured the V and H components of the circularly polarized wave emitting from the feed horn, and in post-processing the V and H components were combined using the relationship in (5.1).

$$\begin{bmatrix} \mathbf{E}_R \\ \mathbf{E}_L \end{bmatrix} = \frac{1}{\sqrt{2}} \begin{bmatrix} 1 & -j \\ 1 & j \end{bmatrix} \begin{bmatrix} \mathbf{E}_h \\ \mathbf{E}_v \end{bmatrix} \tag{5.1}$$

The plots shown in Figure 5.3 and Figure 5.4 are results of transforming the near field data collected near the feed aperture to far field antenna patterns. The transmit band horn septum polarizer does not balance the phase between the H and V polarizations as predicted, and results in higher than expected cross polarization patterns. The receive band horn did have a good phase and

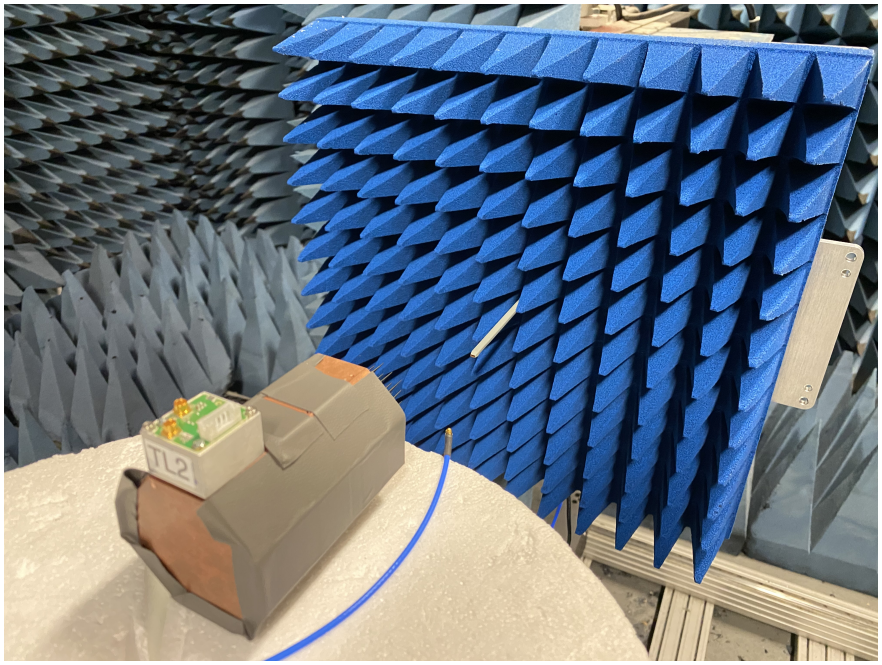

Figure 5.2: The transmit band feed horn is placed in front of the WR-12 open ended waveguide probe at the near field antenna range. The frequency converter module is attached to the active port, and the other 18 waveguide ports are covered with millimeter wave absorber.

amplitude balance to excite the circular mode, and does provide cross-pol isolation greater than 20 dB at the peak of the pattern.

5.3 Full System Measurements

The reflector and feed structure mechanism are affixed to a base plate which was positioned in the near field range, as shown in Figure 5.5 with the laser alignment system visible. The system was angled such that the reflected rays are parallel to the ground, in the same orientation as the open ended waveguide probe attached the range measurement arm. The laser alignment system reflected 4 laser beams off of reflective tape stuck to the parabolic dish, and the system was adjusted until the beams crossed at the location of the feed aperture. Handheld laser systems were also used to align the center of the dish with the measurement probe. The reflector laser alignment system was used to locate the feed cluster aperture at in the focal point of the parabolic reflector.

Once the system was visually aligned with the laser systems, a feed assembly was placed into the feed structure, shown in Figure 5.6. With the feed placed, one-dimensional antenna measure-

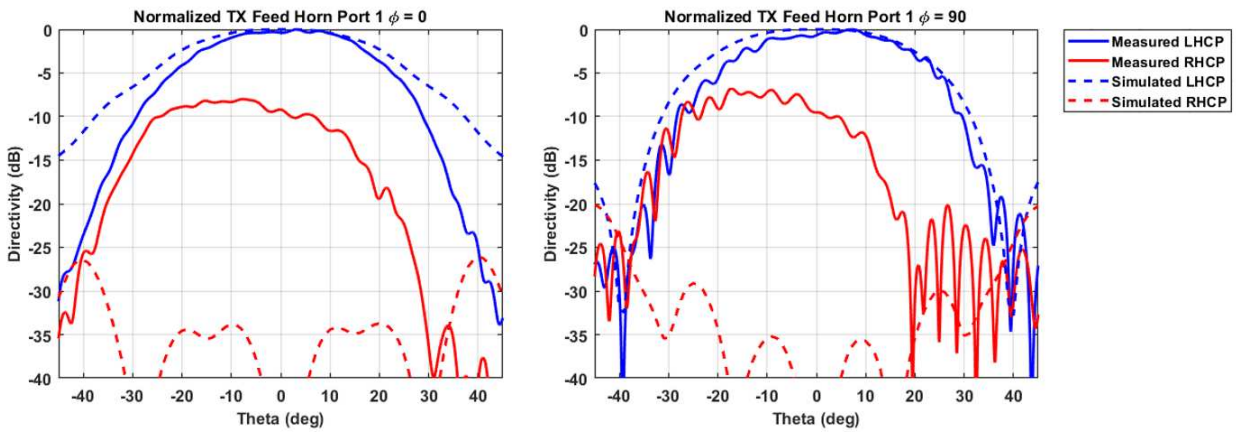

Figure 5.3: Model concept for reflector and feed housing structure mounted to base plate for range testing.

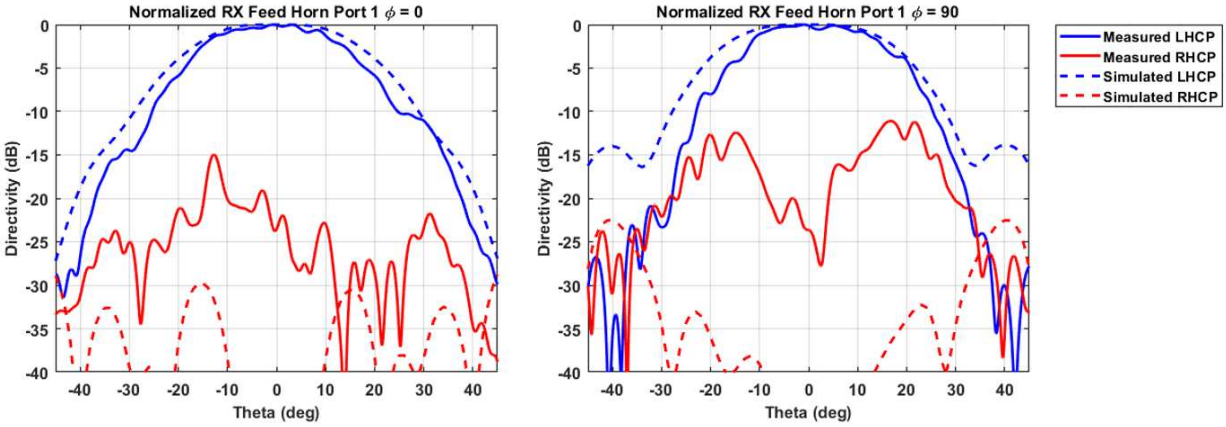

Figure 5.4: Model concept for reflector and feed housing structure mounted to base plate for range testing.

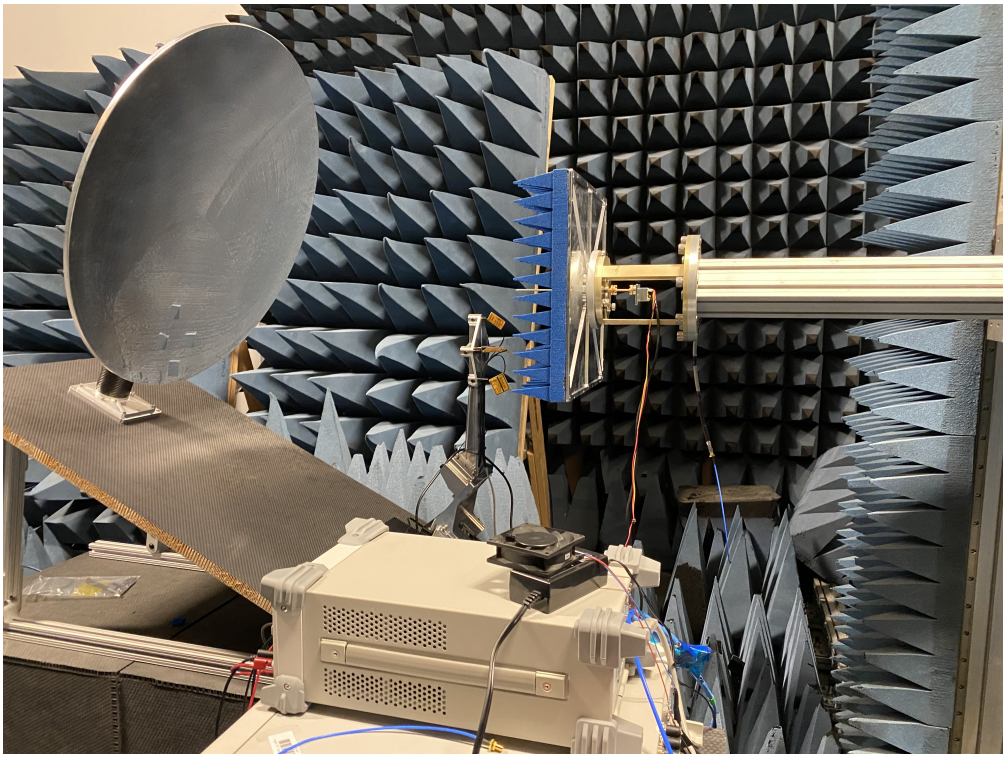

Figure 5.5: The base plate and reflector are mounted in their tilted configuration so that the reflected rays are in-line with the probe.

ments were taken in the x-axis and y-axis across the dish aperture. One-dimensional scans were used to fine tune the location of the feed aperture in the phase center of the dish. The scans are taken to quickly and very accurately assess the feed alignment by viewing the near field raw amplitude and phase data. The phase measured across the aperture should be the same value at the edges of the dish if the feed is aligned to the center, so fine adjustments were made to the mounting structure so that the phase at opposite ends of the dish is equal. The flatness of the phase across the aperture indicates whether or not the feed cluster aperture is at the phase center of the system. Fine adjustments were made in the axis pointing directly towards the center of the dish to flatten the curve until it was well aligned. The raw data collected, and subsequent scans to improve the alignment, are shown in Figures 5.7 - 5.9 for the transmit setup to illustrate this process. The measurements for the receive band were done by simply swapping the feed blocks, so the alignment did not change. The results of the alignment scan after the swap are shown in Figure 5.10.

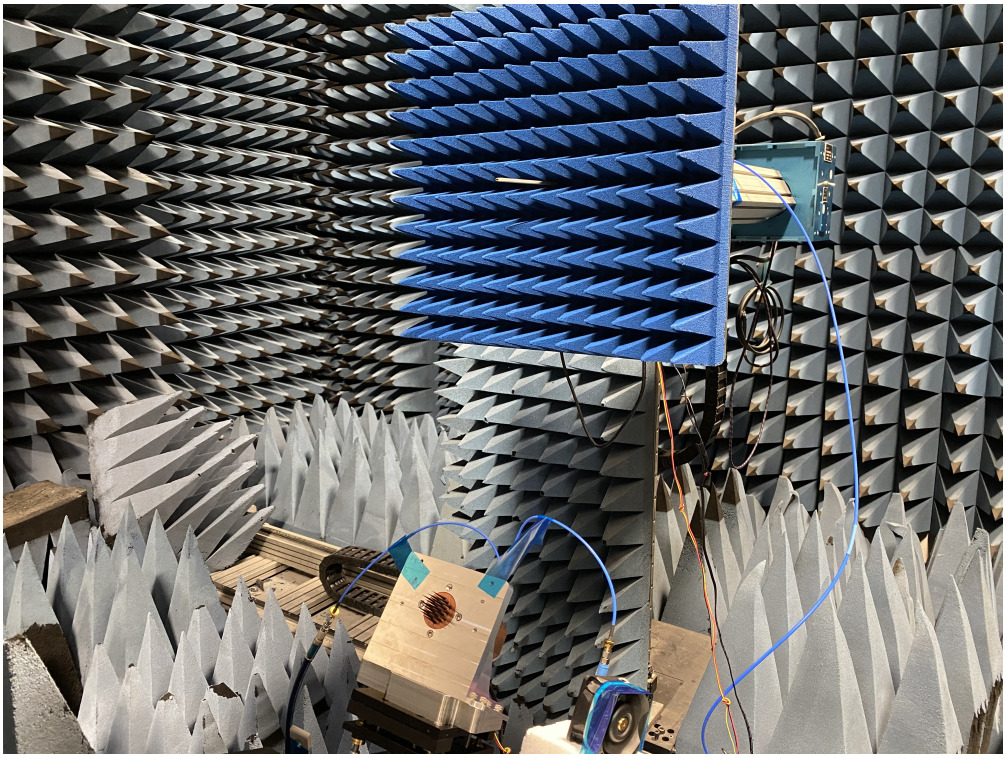

Figure 5.6: Here a feed horn is mounted and pointed towards the dish after visual alignment. This shows the final step to take the full-system measurements.

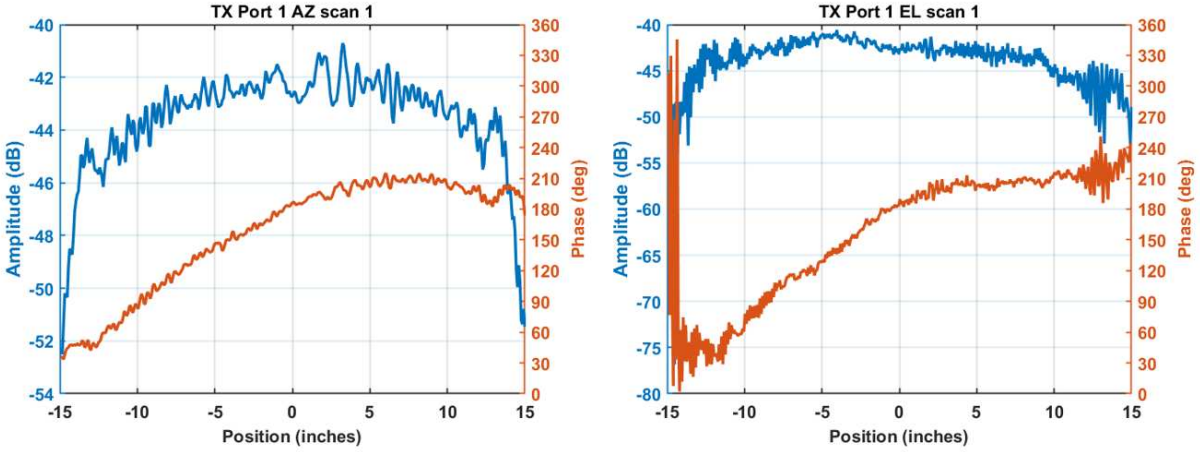

Figure 5.7: The AZ and EL plane scans both indicated slight feed adjustments were necessary. The feed was adjusted and the scans were taken once again.

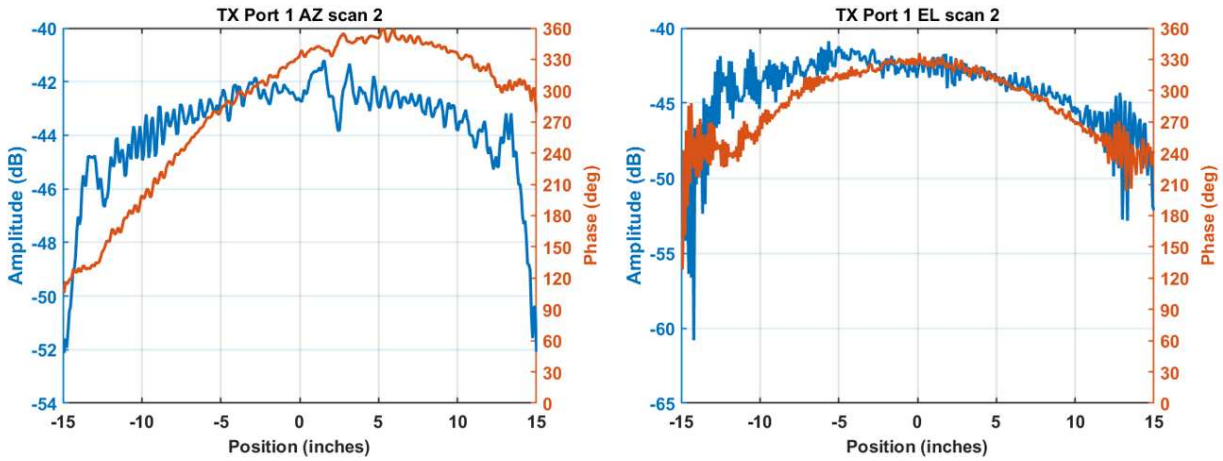

Figure 5.8: The AZ scan indicated more adjustment was necessary, and the EL scan indicates it is very close and was not changed.

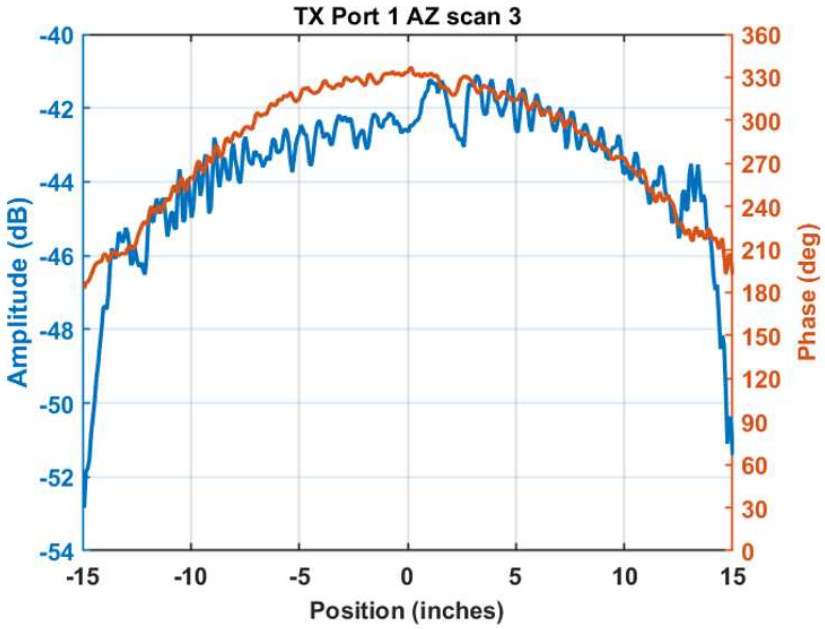

Figure 5.9: The final AZ scan indicated that the feed was well aligned with the dish. The z-axis control point was adjusted to its maximum setting to flatten the phase curve. This feed alignment setting was used to take the TX near field scans.

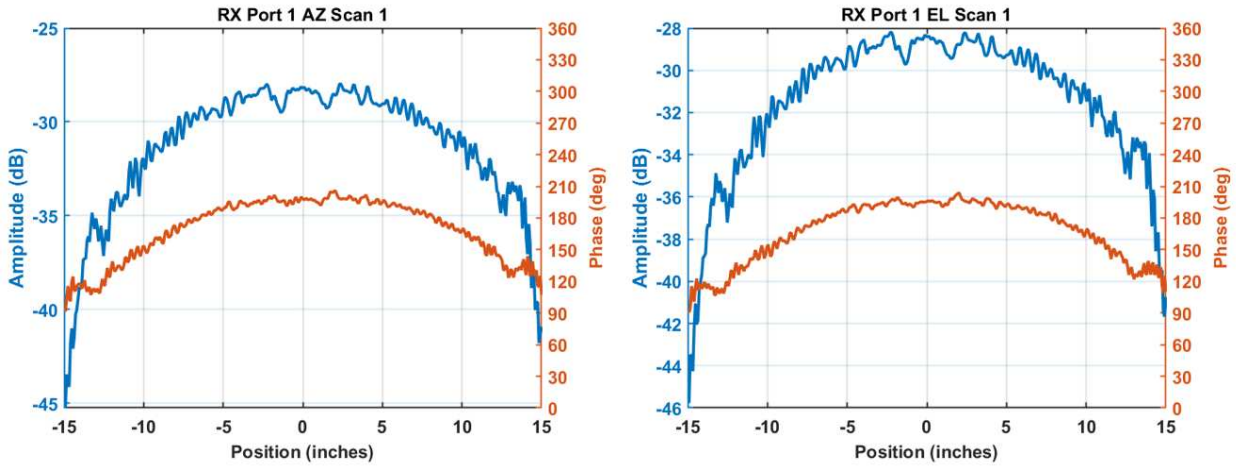

Figure 5.10: The alignment was not expected to change when swapping feed blocks, and these results are indicative of such. The z-axis of the feed could not be further adjusted to flatten the phase across the dish.

With the system aligned properly, near field scans were taken across the full 30 by 30 inch aperture area. With the half-wave spacing at the frequency of interest, the scans would taken nearly 7 hours to complete both H and V polarization scans. The raw data from the measurement was processed with a near field to far field transformation to obtain the results shown in figures 5.11 - 5.22. The contour plots are shown for the full dish aperture, and then zoomed in to more clearly show the individual beams in the center. The U and V axes are related to spherical coordinates, as shown in equation (5.2), to map the beam patterns to a Cartesian grid. The 2D patterns are shown below the contour plots for the respective ports, and are cut in the principal plane of the port under test. The simulated results for the reflector dish are plotted for comparison.

$$U = \sin\theta\cos\phi \tag{5.2a}$$

$$V = \sin\theta\sin\phi \tag{5.2b}$$

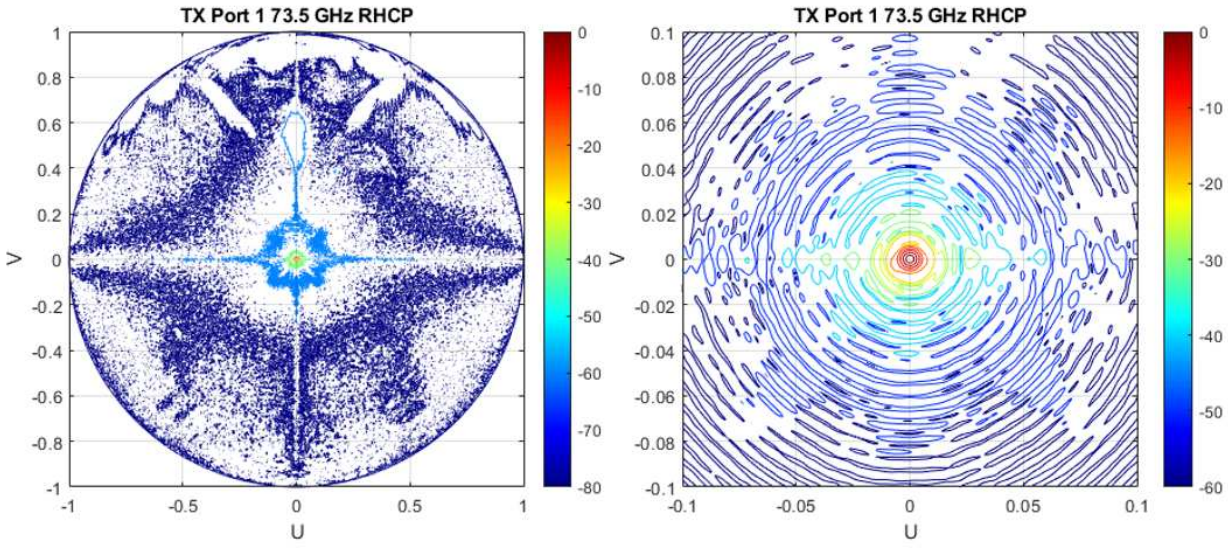

Figure 5.11: TX port 1 measured contours. Full dish area results (left) and a zoomed in view of the same result on the center to show beam contours more clearly (right).

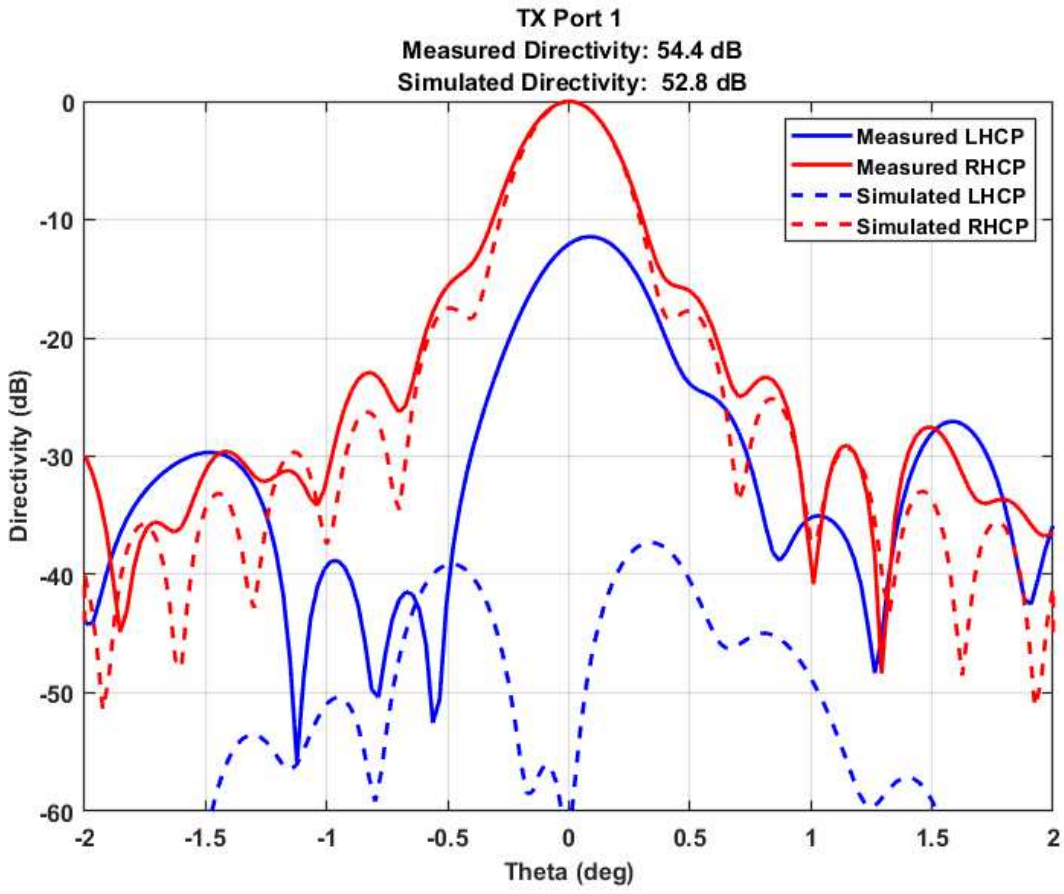

Figure 5.12: TX port 1 principal plane patterns. Measured and simulated patterns are shown.

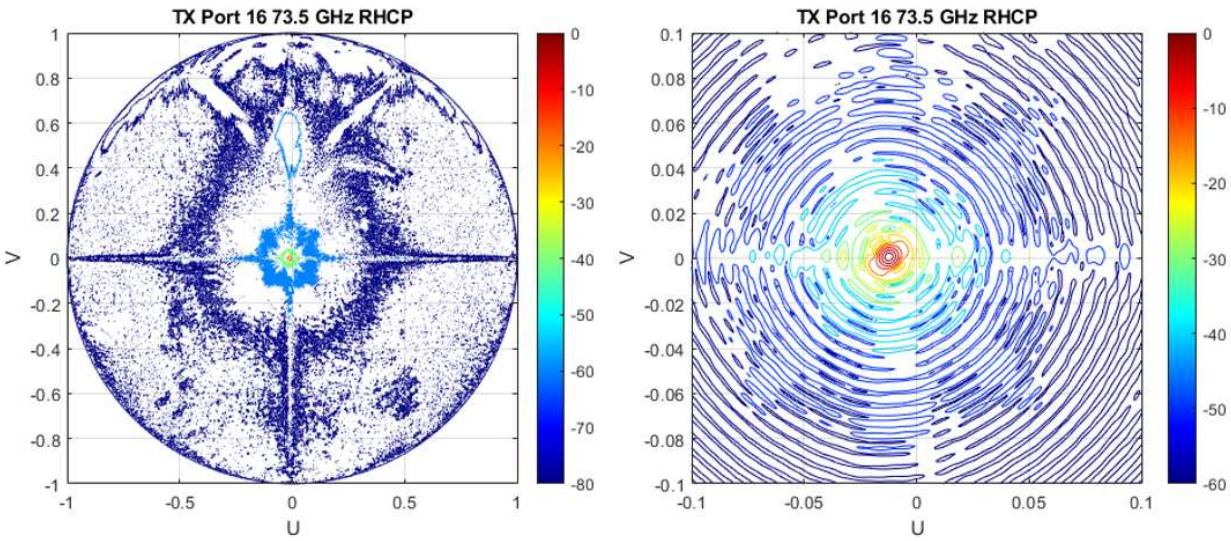

Figure 5.13: TX port 16 measured contours. Full dish area results (left) and a zoomed in view of the same result on the center to show beam contours more clearly (right).

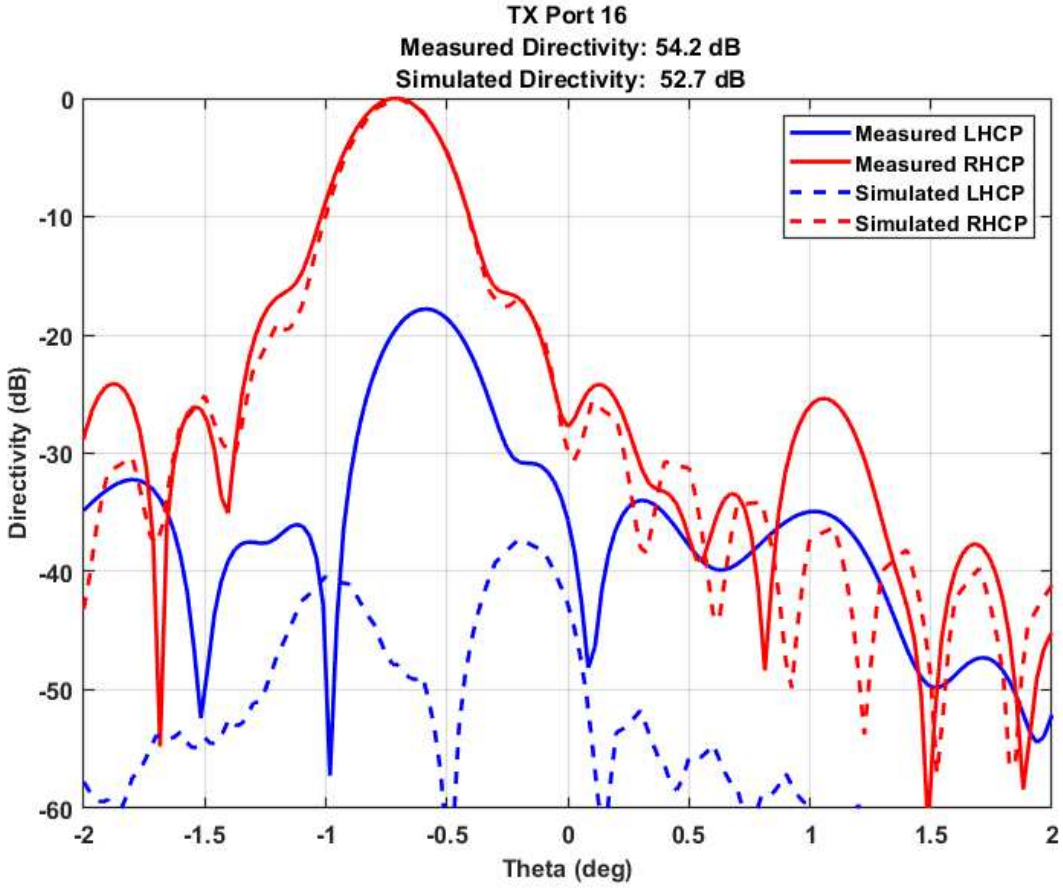

Figure 5.14: TX port 16 principal plane patterns. Measured and simulated patterns are shown.

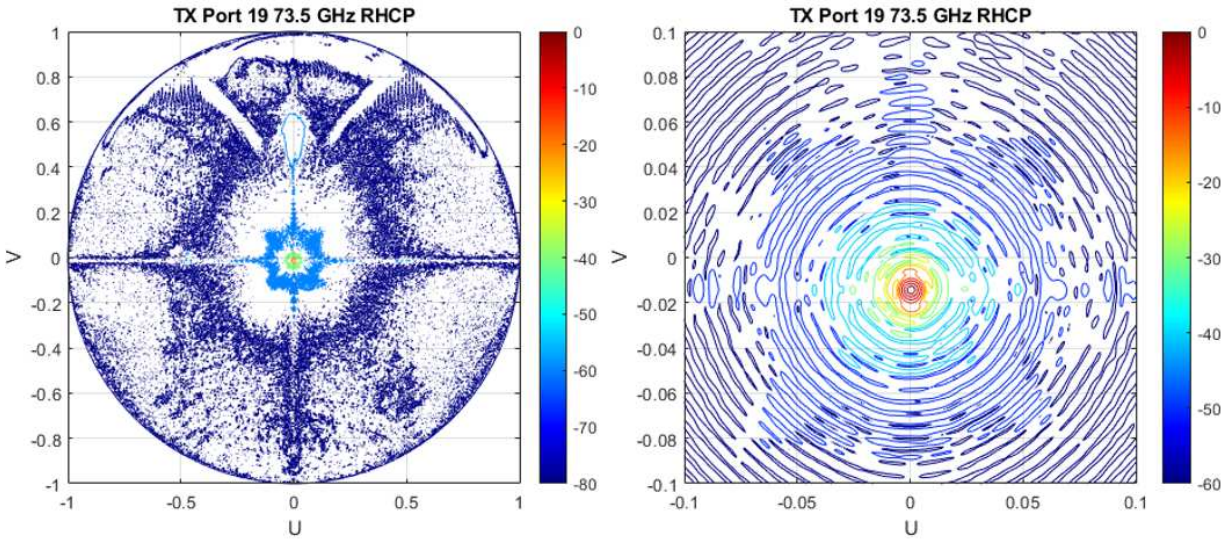

Figure 5.15: TX port 19 measured contours. Full dish area results (left) and a zoomed in view of the same result on the center to show beam contours more clearly (right).

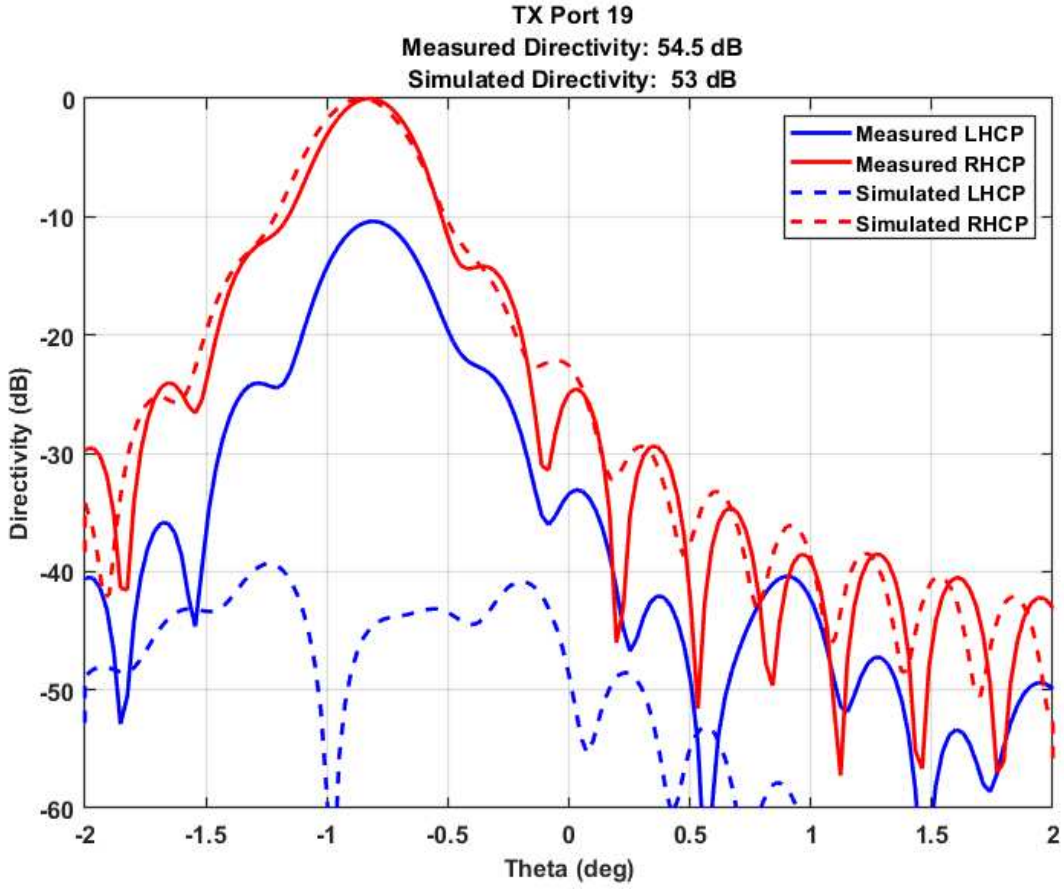

Figure 5.16: TX port 19 principal plane patterns. Measured and simulated patterns are shown.

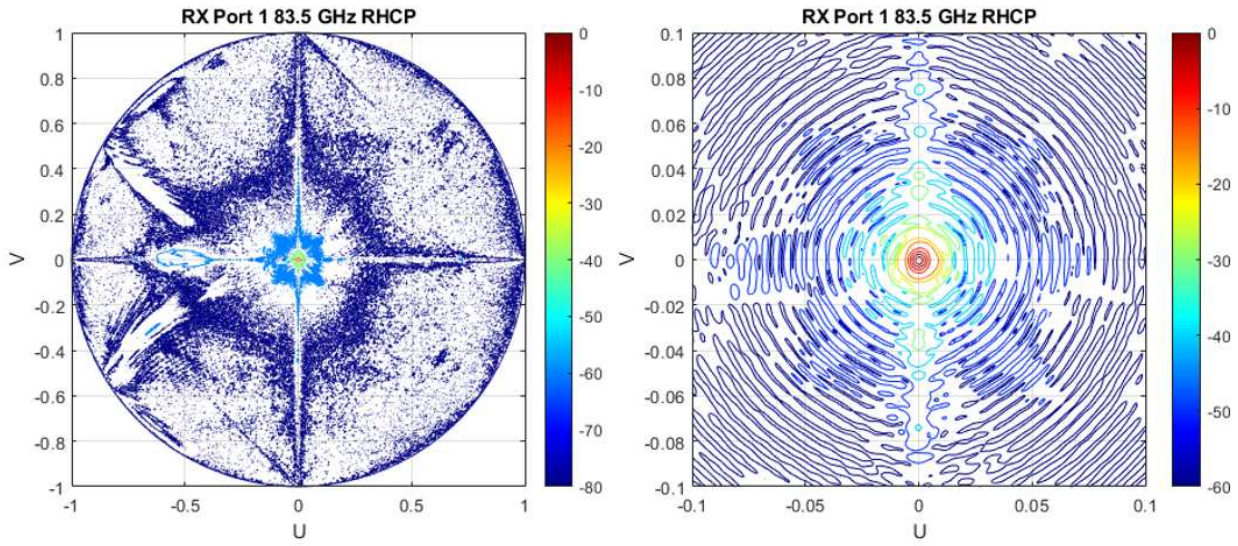

Figure 5.17: RX port 1 measured contours. Full dish area results (left) and a zoomed in view of the same result on the center to show beam contours more clearly (right).

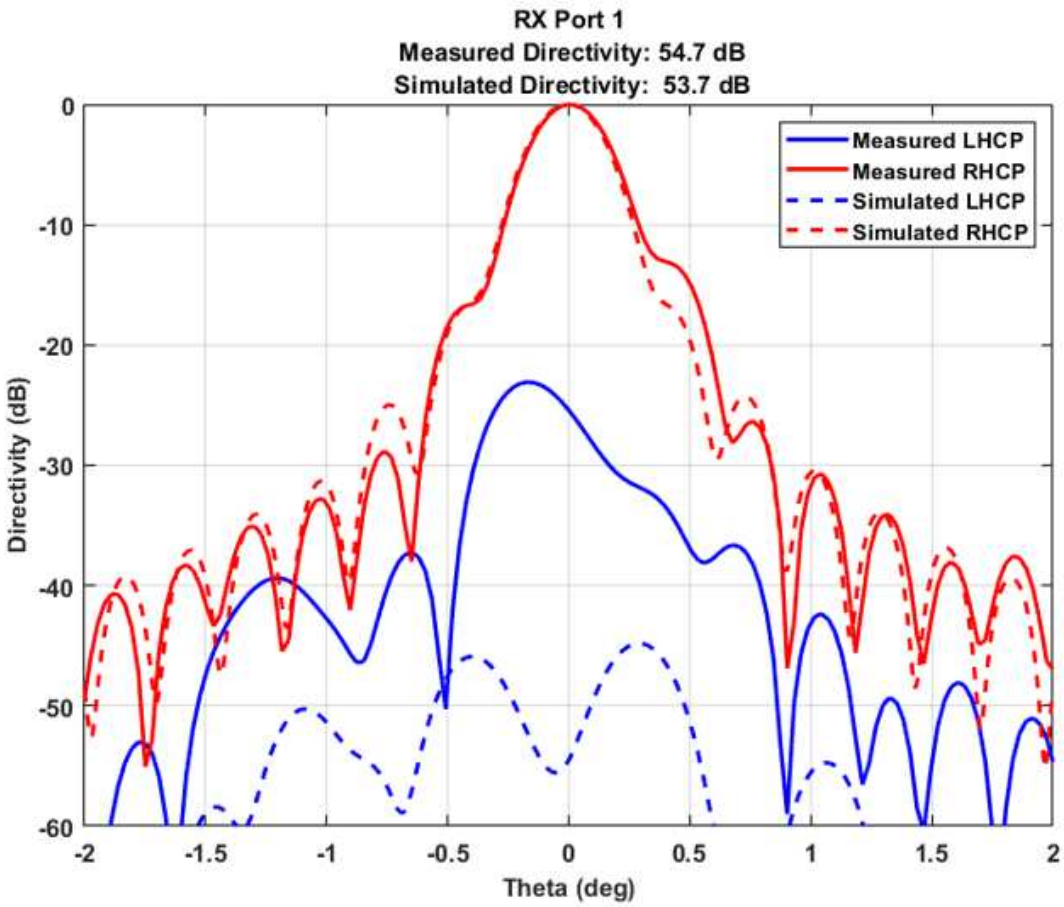

Figure 5.18: RX port 1 principal plane patterns. Measured and simulated patterns are shown.

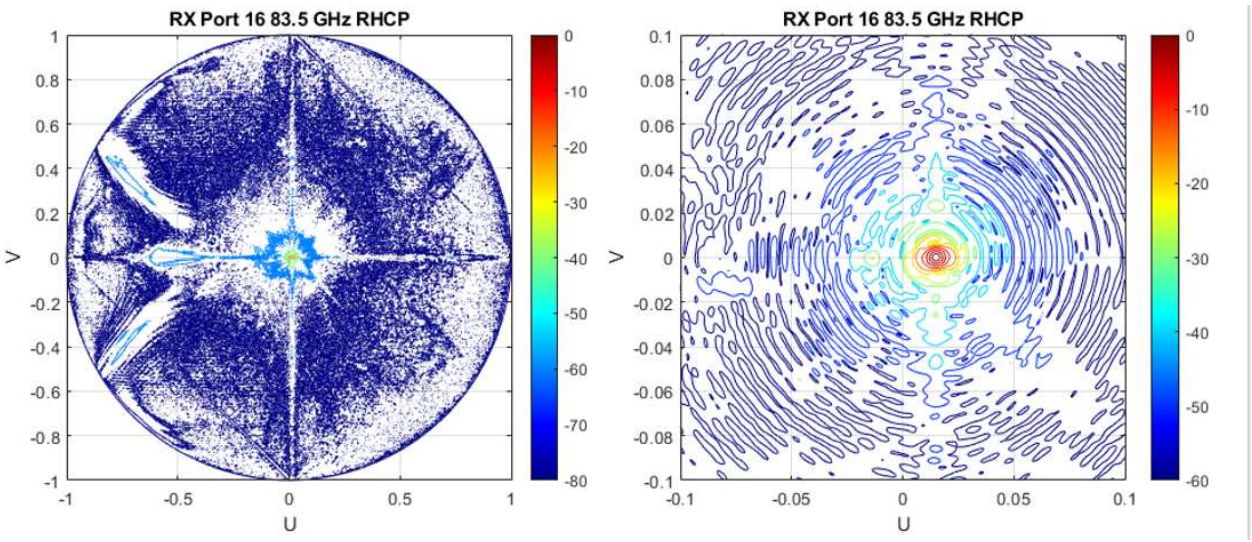

Figure 5.19: RX port 16 measured contours. Full dish area results (left) and a zoomed in view of the same result on the center to show beam contours more clearly (right).

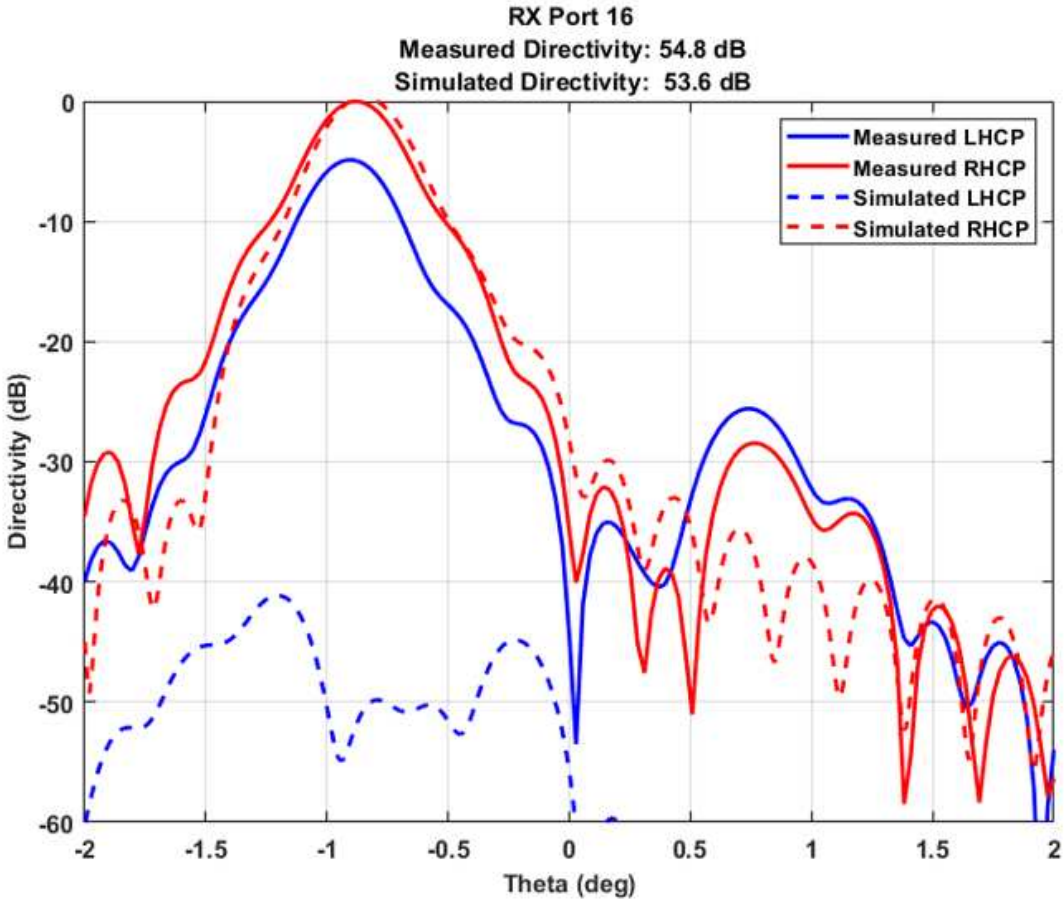

Figure 5.20: RX port 16 principal plane patterns. Measured and simulated patterns are shown.

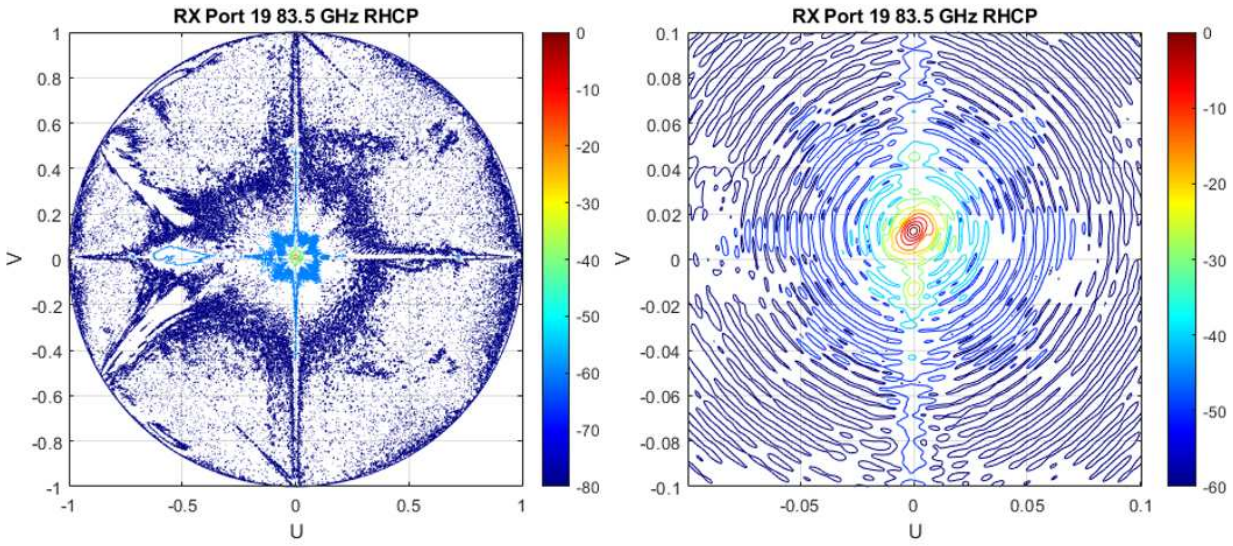

Figure 5.21: RX port 19 measured contours. Full dish area results (left) and a zoomed in view of the same result on the center to show beam contours more clearly (right).

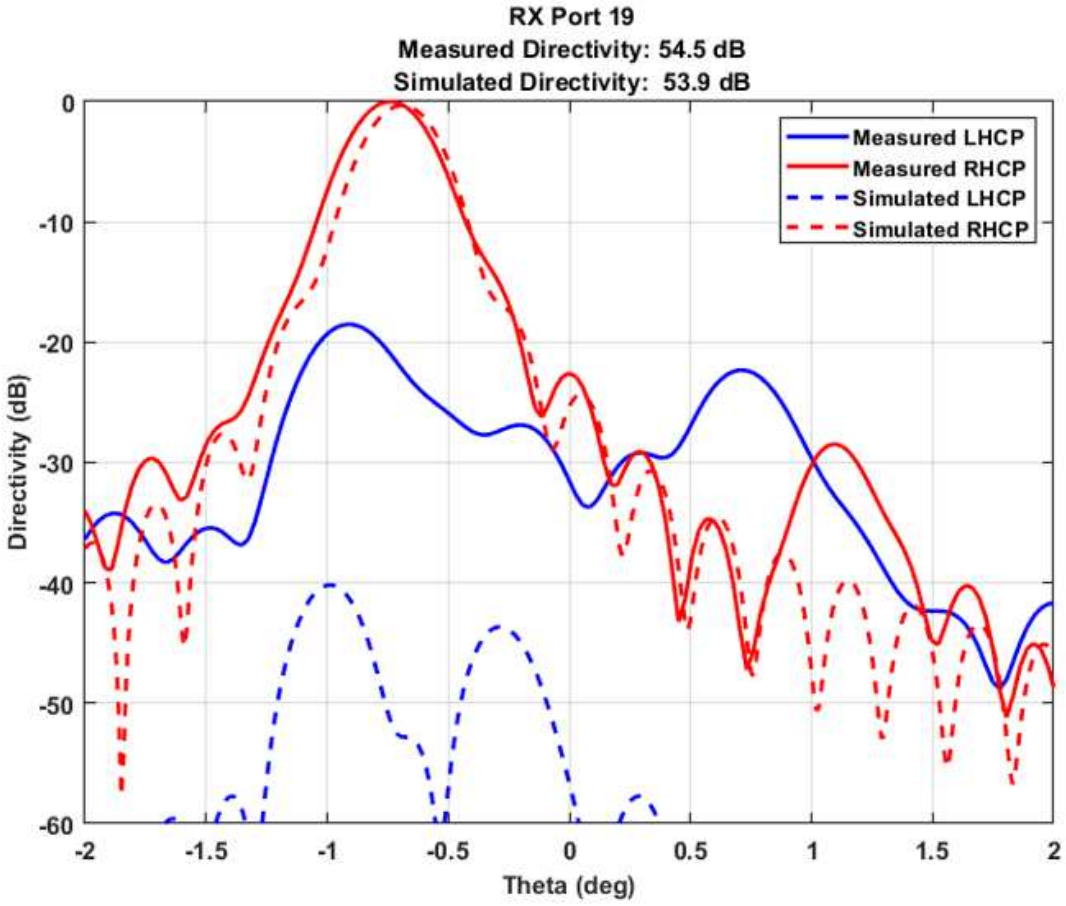

Figure 5.22: RX port 19 principal plane patterns. Measured and simulated patterns are shown.

Chapter 6

Conclusion and Future Work

6.1 Summary and Conclusion

The objective of this thesis was to develop and demonstrate a dual-band dual-circularly polarized multibeam V/W-band Satcom system. The primary challenge in this design was realizing the multibeam antenna feed horn to support 19 independent beams in the transmit and receive bands for the antenna system. To meet the objectives for the antenna development, custom waveguide features had to be designed to carry the signal, and beam shape between circularly polarized and linearly polarized waves. The waveguide components included a square waveguide mitered bend, a stepped septum polarizer beam former, and several waveguide transitions. The critical waveguide features were designed through simulation using CST MWS. Once designed, waveguide coupons were built and tested to increase the confidence that the components could be integrated and realized in the full waveguide feed subsystem. These steps were essential to the low-risk path of development for a complex multibeam feed system. Risk was reduced designing, building, and testing individual components before integrating them together in a complex system. Full-scale prototype V-band and W-band feed systems were successfully realized, and they were integrated with an offset fed parabolic reflector system to complete the wireless communication prototype system.

The comprehensive V/W system tests were carried out using frequency mixing devices for millimeter wave systems, and an open-ended WR-12 waveguide probe. The over-the-air tests verified that the waveguide feed assemblies were functioning as designed. The integrated antenna system was then measured at the near field range for a system demonstration. The measurements from the system demonstration were then compared to simulated system results. Beams were successfully formed and measured during the system evaluation for the transmit and receive configurations. Machining tolerances, particularly in the septum polarizer, were the primary source of deviation

from expected simulated values. The system successfully functioned as a capable next generation multibeam V/W-band antenna system for the transmit and receive configurations.

6.2 Future Work

The beam forming septum polarizer contained in the waveguide system did not perform consistently across waveguide channels. The axial ratio resultant from the feed assembly was not consistent across all waveguide channels, primarily due to phase and amplitude imbalance resultant from waveguide transitions and the stepped septum polarizer network. For future system development, the septum polarizer fabrication should be carefully analyzed to conclusively determine how consistently they can be fabricated with a tighter machining tolerance, given the variability between the measured waveguide horn parameters.

The frequency selective surface needs to be further developed and tested to realize full duplex operation for this system. This system component was not necessary to characterize the transmit and receive RF systems, but is a key area of future development to realize the full system capability.

The waveguide feed horns are solid copper in the absence of waveguide channels, since this was the most straight forward fabrication method for the prototype system. The next version of the feed assembly should be optimized for weight but reducing the amount of unused copper, or considering a mixture of other materials to provide the structural support necessary to realize the waveguide channels. This alteration would help to minimize the overall mass of the configured system.

Bibliography

[1] S. K. Rao. Advanced antenna technologies for satellite communications payloads. *IEEE Transactions on Antennas and Propagation*, 63(4):1205–1217, 2015.

[2] D. Serrano-Velarde, E. Lance, H. Fenech, and G. R-Guisantes. A novel dimensioning method for high throughput satellite design. In *2012 IEEE First AESS European Conference on Satellite Telecommunications (ESTEL)*, pages 1–6, Oct 2012.

[3] Angel Vazquez, Ana Perez-Neira, Dimitrios Christopoulos, Symeon Chatzinotas, Björn Ottersten, Pantelis-Daniel Arapoglou, Alberto Ginesi, and Giorgio Taricco. Precoding in multibeam satellite communications: Present and future challenges. *IEEE Wireless Commun Mag*, 23, 06 2015.

[4] Asoka Dissanayake, Jeremy Allnutt, and Fatim Haidara. Cloud attenuation modelling for shf and ehf applications. *International Journal of Satellite Communications*, 19:335 – 345, 05 2001.

[5] MATLAB. *Phased Array System Toolbox, version 9.0.0 (R2016a)*. The MathWorks Inc., Natick, Massachusetts, 2010.

[6] L. R. Shet, G. P. Reddy, I. Ahmad, P. Killedar, P. K. Gupta, and Anuradha T K. Challenges and configuration of isro's future q/v band satellite. In *2016 International Conference on Wireless Communications, Signal Processing and Networking (WiSPNET)*, pages 674–679, March 2016.

[7] Maruthi N. Yogeesh. Sige millimeter-wave (w-band) down-converter for phased focal plane array. Master's thesis, University of Massachusetts Amherst, 02 2014.

[8] Tim Fisher. How are 4g and 5g different? https://www.lifewire.com/5g-vs-4g-4156322, November 2019.

[9] Fenech H., Amos Tomatis, and Soumpholphkakdy. Ka-sat and future hts systems. *IEEE*, pages 1–2, 2013.

[10] A. Jerbil, M. Lucente, and T. Ruggieri Rossi. W-band satellite transmission in the wave mission. *IEEE*, pages 1–8, 2006.

[11] Lucente and Marco. Experimental missions in w-band: a small leo satellite approach. *IEEE*, pages 1–30, 2007.

[12] David M. Pozar. *Microwave Engineering*, volume 4. Wiley India, New Delhi, India, 2017, 2010.

[13] Sophocles J. Orfanidis. *Electromagnetic Waves and Antennas*, volume 1. Rutgers University, 1999.

[14] T. Hnilicka, V. Schejbal, O. Fisher, and T. Zalabsky. Design of square waveguide corner. In *2018 New Trends in Signal Processing (NTSP)*, pages 1–4, Oct 2018.

[15] S. Verploegh and Z. Popović. V- and w-band two-way waveguide splitters fabricated by metal additive manufacturing. In *2018 IEEE MTT-S Latin America Microwave Conference (LAMC 2018)*, pages 1–4, Dec 2018.

[16] A. A. Kifflenko, D. Y. Kulik, L. A. Rud, V. I. Tkachenko, and N. Herscovici. Cad of double-band septum polarizers. In *34th European Microwave Conference, 2004.*, volume 1, pages 277–280, 2004.

[17] M. J. Franco. A high-performance dual-mode feed horn for parabolic reflectors with a stepped-septum polarizer in a circular waveguide [antenna designer's notebook]. *IEEE Antennas and Propagation Magazine*, 53(3):142–146, June 2011.

[18] V. N. Skresanov, V. V. Glamazdin, A. A. Kirilenko, D. Y. Kulik, M. P. Natarov, O. M. Pylypenko, L. A. Rud, A. I. Shubnyj, and V. A. Zolotarev. Circular polarization splitters for

three-band feed of radiotelescope reflector antenna. In *2013 IX Internatioal Conference on Antenna Theory and Techniques*, pages 43–48, 2013.